Università degli Studi di Palermo

AREA RICERCA E TRASFERIMENTO TECNOLOGICO
SETTORE DOTTORATI E CONTRATTI PER LA RICERCA
U. O. DOTTORATI DI RICERCA

Ph.D. course in Technologies and Science for Human Health
Department of Biological, Chemical and Pharmaceutical Sciences and Technologies
CHEM-07/A

IDENTIFICATION OF NEW HETEROCYCLIC MOLECULES FOR THE TREATMENT OF LYMPHOMAS

Ph.D. Candidate
Ignazio Sardo

Coordinator of the Ph.D. course
Prof. Bruno Giuseppe Pignataro

Tutor
Prof. Maria Valeria Raimondi

Co-tutor
Prof. Marco Tutone

Cycle XXXVII
Graduation year 2025

SUMMARY

ABBREVIATIONS

ACN	Acetonitrile
ADP	Adenosine diphosphate
B cell	B lymphocyte
BCL-2	B-cell lymphoma 2
BL	Burkitt lymphoma
BPMD	Binding Pose Metadynamics
BTK	Bruton's tyrosine kinase
CAR-T	Chimeric antigen receptor T-cells
CI	Checkpoint inhibitor
CNS	Central nervous system
DLBCL	Diffuse Large B-Cell Lymphoma
DMAP	4-Dimethylaminopyridine
DMF	Dimethylformamide
DMSO	Dimethyl sulfoxide
EBV	Epstein–Barr virus
EMT	Epithelial–mesenchymal transition
EdU	5-ethynyl-2'-deoxyuridine
FL	Follicular lymphoma
FoxO	Forkhead box O
HDAC	Histone deacetylase
HL	Hodgkin lymphoma
HOBt	1-Hydroxybenzotriazole
Hp	*Helicobacter pylori*
IPA	Isopropyl alcohol
MALT	Mucosa-associated lymphoid tissues
MAOS	Microwave-assisted organic synthesis
MD	Molecular Dynamics
MPLC	Medium-pressure liquid chromatography

NAM	Nicotinamide
NHL	Non-Hodgkin lymphoma
c-Myc	Myelocytomatosis gene
NK	Natural Killer cell
NMI	N-methylimidazole
NSCLC	Non-small cell lung cancer
PBMC	Peripheral blood mononuclear cell
PDB	Protein Data Bank
PHA	Phytohemagglutinin
PI	Propidium iodide
PI3K	Phosphoinositide 3-kinase
QUE	Quercetin
RMSD	Root-mean-square deviation
ROS	Reactive oxygen species
RSC	Reed-Sternberg cell
SIRT6	Sirtuin 6
SIRT	Sirtuin
SPE	Solid-phase extraction
T cell	T lymphocyte
TCFH	N,N,N′,N′-tetramethylchloroformamidinium hexafluorophosphate
TMRE	Tetramethylrhodamine Ethyl Ester
TEV	Tobacco Etch Virus
TSN	Trichostatin A
VS	Virtual screening

1. INTRODUCTION

The lymphatic system consists of several components including lymph, lymphatic vessels, lymph nodes and various lymphoid organs, i.e. spleen, thymus, bone marrow and tonsils.[1] The lymphatic system plays a key role in maintaining tissue fluid homeostasis by returning excess interstitial fluid and metabolic waste to the venous circulation through a network of lymphatic vessels. Along this pathway, the lymph is filtered in lymph nodes before entering the systemic circulation.[2] The lymphatic system is also involved in immune surveillance, protecting the body against foreign particles and microorganisms. It achieves this by transporting antigens and leukocytes to lymph nodes, where antigen-primed and targeted lymphocytes, along with other immune cells, are directed into the lymphatic and blood vessels.[3] The structural organization and major anatomical components of the lymphatic system are illustrated in Figure 1. The two main types of lymphocytes are T lymphocytes (T cells) and B lymphocytes (B cells). The distribution and functions of T cells in immune responses vary across tissues and life stages. T cells are widely distributed throughout the body, in primary and secondary lymphoid organs, mucosal and barrier tissues, exocrine glands, adipose tissue, and even the brain and the central nervous system (CNS). The highest concentration of T cells is found in lymphoid tissues, but a substantial population can be also found in mucosal surfaces such as lungs and gastrointestinal tract, as well as the skin. In contrast, only about 2–3% of the total T cell pool circulates in peripheral blood.[3] T cells have a variety of different and specialized jobs in defending the body against disease and in immune homeostasis. Their actions also involve modulation of immune responses, elimination of infected and tumoral cells, and immune tolerance. Among their many roles, helper T cells ($CD4^+$) also act as coordinators of the immune response. They recognize antigens presented by antigen-presenting cells and, in response, secrete cytokines thus activating macrophages and B cells to produce antibodies. Cytotoxic T cells ($CD8^+$) play a direct role in eliminating virus-infected and cancerous cells. Once activated, they recognize cells with specific antigens on their surface and release cytolytic factor such as perforin and granzymes, thus inducing apoptosis. Their activity is crucial for immune surveillance, preventing the spread of infections and suppressing tumour development. [4]

B cells are present in primary and secondary lymphoid tissues, including the bone marrow, spleen, lymph nodes, Peyer's patches, and mucosa-associated lymphoid tissues (MALT). A significant population of B cells also live on mucosal surfaces, including the respiratory and gut tracts, where they are involved in frontline immune defence. Although cellular immunity

is mostly performed by T cells, B cells are crucial in humoral immunity, generating antibodies, displaying antigens, and regulating immune responses.[5] Their principal role is antigen recognition, followed by the production of antibodies that neutralize pathogens and facilitate their elimination. The lymphatic system is prone to several disorders like all the other systems. Lymphedema occurs when the lymphatic system's ability to drain fluid is impaired, thus leading to accumulation and subsequent swelling in the affected areas.[6] Lymphadenitis refers to the inflammation or enlargement of lymph nodes, typically resulting from a bacterial infection, even though viral or fungal infections may also be responsible. Affected lymph nodes often become swollen, tender, and sometimes warm to the touch, indicating an immune response to the infections.[7] Lymphatic filariasis, also known as elephantiasis, is a widespread mosquito-borne disease caused by parasitic roundworms. It is prevalent in tropical and subtropical regions, including Africa, Asia, the Pacific, the Caribbean, and South America. This condition occurs when microscopic nematodes infect the lymphatic system, multiply rapidly, and impair its function, leading to swelling and potential complications.[8]

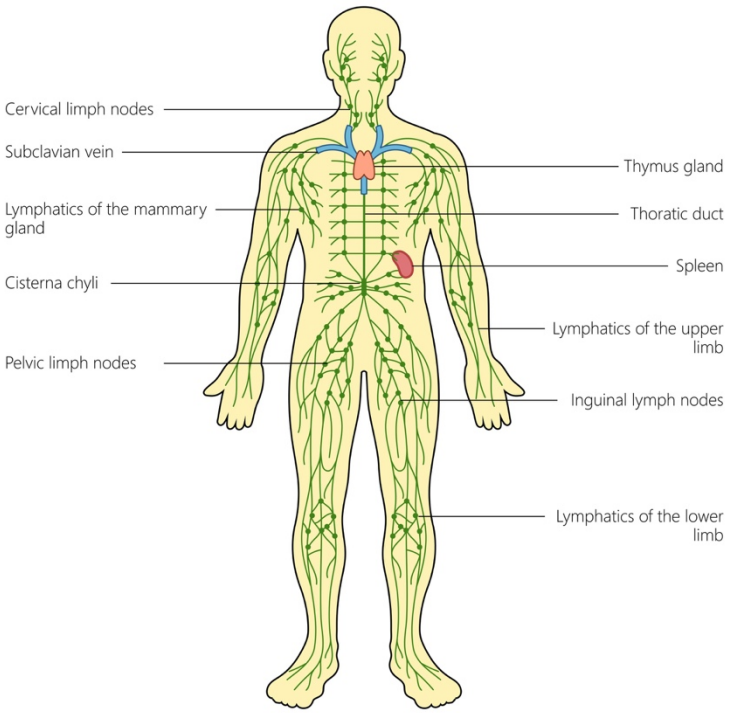

Figure 1. Anatomy and components of the human lymphatic system.

The neoplastic transformation of lymphocytes leads to the development of lymphomas. These malignancies are caused by uncontrolled proliferation of B cells and T cells, thus resulting in neoplastic proliferation of the lymphoid tissues.

2. LYMPHOMAS: CLASSIFICATION AND TREATMENT

Lymphomas are generally divided into two major categories: Hodgkin lymphoma (HL) and non-Hodgkin lymphoma (NHL).

According to American Cancer Society projections, approximately 8,570 new cases of HL were expected in the United States in 2024, with higher occurrence in men compared with women. Although HL may arise in individuals of any age, it more commonly affects young adults. A second peak of incidence occurs in adulthood, mainly in individuals of 55 years and above. Even though rare under 5 years of age, HL is the most frequent malignancy in adolescent between 15- and 19-year-olds.[9] HL has a typical clinical and pathological presentation and, unlike NHL, occurs with lower frequency. The hallmark of HL is the presence Reed-Sternberg cells (RSCs), atypical B cells, originated from B cells in the germinal centers. Although RSCs are typically large and may be multinucleated or contain a single, prominent nucleus with distinct nucleoli, they are often present in small numbers, with the majority of the tumour composed of a reactive inflammatory infiltrate, including T cells, eosinophils, neutrophils, and plasma cells. Tumour microenvironment has been considered very significant for the occurrence of HL, for tumour growth, and for immune evasion.[10] The classical HL, compared to NHL, occurs with highest frequency, accounting for approximately 95% of cases. HL, in its earlier stages, stays confined to a single lymph node region, whereas in more advanced stages, it can spread to extranodal sites.[11] Chemotherapy regimens, including the ABVD protocol (Adriamycin, Bleomycin, Vinblastine, and Dacarbazine), combined with radiotherapy, remain the cornerstone of treatment for earlier stages of the disease.[12] Stem cell transplantation and novel immunotherapies, including checkpoint inhibitors (CIs) such as nivolumab and pembrolizumab, are new frontiers for the treatment of relapsed or refractory disease.[12] HL has a generally favourable prognosis, with a 5-year overall relative survival rate of around 89% across all stages. Early-stage disease demonstrates particularly high survival rates, with 5-year survival reaching around 92%. Even when the disease has regional spread into adjacent tissues and adjacent lymph nodes, survival estimation remains excellent, with rates of around 94%.[13] However, age remains a significant predictor of survival. Young adults and children, and more commonly individuals between 15 and 39 years of age, achieve survival rates of more than 90%, largely reflecting the success of current therapeutic approaches.[14]

Non-Hodgkin lymphoma (NHL) is an extremely heterogenous group of lymphoid cancers essentially consisting of the malignant transformation of the B cells, T cells, and less frequently the Natural Killer (NK) cells. NHL includes a highly heterogeneous group of subtypes, each characterized by unique molecular, cellular, and immunological features that influence their pathogenesis, clinical manifestations, and response to therapy.[15] Unlike the presence of RSCs, the diagnostic landmark for HL, NHL arises from the malignant transformation of various immune cell lineages, typically occurring within a complex and dynamic tumour microenvironment.[16] The pathogenesis of NHL is also strongly associated with the presence of genetic alteration, including mutations, chromosomal translocations, and dysregulation of cell signalling pathways, thus resulting in disruptions in normal processes of lymphocyte differentiation, proliferation, and survival.[17] Chromosomal translocations such as t(14;18) involving the B-cell lymphoma 2 (BCL-2) gene in Follicular lymphoma (FL) and t(8;14) affecting the cellular Myelocytomatosis (*c-Myc*) gene in Burkitt lymphoma (BL) are representative defects responsible for oncogenesis.[18] These translocations induce oncogene overexpression, resulting in uncontrolled cell proliferation and evasion from cell death, both of which are critical aspects of NHL biology. NHL subtypes exhibit distinct clinical behaviors, ranging from indolent forms, i.e. FL, which typically follow a slow and progressive course, to the rapidly progressive forms like Diffuse Large B-Cell Lymphoma (DLBCL), which require immediate therapeutic intervention due to their rapid progression and spreading.[19] Moreover, the clinical presentation is very variable, depending on the subtype, disease stage, and tumour burden, with clinical manifestations ranging from asymptomatic disease to rapidly enlarging lymphadenopathy and systemic symptoms.[20] Standard treatments generally include chemotherapy, targeted therapies, immunotherapy, and hematopoietic stem cell transplantation; however, prognosis remains highly variable: while some subtypes respond favourably, others are resistant to treatment, underlining the need for continuous investigation into novel therapeutic strategies.[21] In recent years, innovative therapies emerged as promising strategies for NHL treatment. Chimeric antigen receptor T-cells (CAR-T) therapy, where the patient's T cells are genetically modified to recognize cancer cells specifically, showed remarkable efficacy for the treatment of relapsed and refractory DLBCL, and also for other aggressive subtypes.[22] Another promising therapeutic intervention was the use of bispecific antibodies like gofitamab and epcoritamab, in which T cells and tumour cells were simultaneously targeted by the antibody for enhancing cytotoxic potential through immunotherapy.[23] In addition, small-molecule inhibitors targeting the phosphoinositide 3-kinase (PI3K), Bruton’s tyrosine

kinase (BTK), and BCL-2 pathways are investigated, and compounds such as idelalisib (PI3K inhibitor), ibrutinib (BTK inhibitor), and venetoclax (BCL-2 inhibitor) provided alternative therapeutic options.[24] Although NHL essentially involves lymphoid tissue, extranodal spread is common and has prognostic and therapeutic implications.[25] Extranodal involvement may affect multiple organs, including skin, the gastrointestinal tract, the CNS, lungs, liver, and bones. Certain NHL subtypes exhibit a predilection for specific extranodal sites, such as primary mediastinal B-cell lymphoma, primary CNS lymphoma, and primary gastrointestinal lymphoma. The latter, generally associated with MALT lymphoma, is also linked to persistent infections, such as those caused by *Helicobacter pylori* (Hp).[26] Cutaneous T-cell lymphoma is one notable type of extranodal lymphomas observed in the skin, where their clinical presentations make their diagnosis and treatment complicated.[27] The etiology for NHL is multifactorial, consisting of genetics, infectious agents, and environmental factors.[28] Lifestyle risk factors such as tobacco smoking, obesity, and exposure to chemical and physical carcinogens, including pesticides and radiation, have been linked to an increased risk of developing NHL, although their contribution appears less significant than that of genetic and infectious etiologies.[29] Researchers' efforts in NHL treatment are primarily focused on optimizing immunotherapeutic approaches, refining the use of molecular profiling for precision medicine, and enhancing early detection strategies. Advances in single-cell sequencing and artificial intelligence-driven pathology are revolutionizing the understanding of NHL heterogeneity, thus facilitating the identification of novel therapeutic targets.[30] Ongoing trials are evaluating next-generation CAR-T, antibody-drug conjugates, and CIs for greater therapeutic efficiency and less toxicity.[31] Moreover, precision oncology is applied to the treatment of NHL. Personalized treatments are made possible by genomic profiling, which helps to minimize avoidable toxicities while maximizing treatment efficacy. Non-invasive monitoring of disease progression and therapeutic response is further supported using liquid biopsies, which allow for the analysis of circulating tumour DNA levels.[32]

NHLs can be classified into two major categories based on the aggressiveness of the disease: indolent lymphomas (slow-growing) and aggressive lymphomas (fast-growing).

Indolent lymphomas comprise the largest subcategory of NHLs and are characterized by their slow-growth nature and generally chronic clinical history. Unlike the aggressive lymphomas, that require an urgent treatment, the indolent forms can evolve very slowly or remain asymptomatic over several years, during which patients can maintain their normal lifestyle until serious manifestations.[33] Although traditionally considered incurable by

standard treatments, the available therapies have improved patients' quality of life and survival rate.[34,35] Today, many individuals diagnosed with indolent lymphomas can live for decades with the disease, owing to management strategies such as active surveillance (watch-and-wait) and the implementation of targeted immunotherapies.[36] A key feature of indolent lymphomas is their potential for transformation into their more aggressive counterparts, including the transformation into DLBCL.[37] For this reason, continuous follow-up is mandatory for the assessment of changes in the biology of the disease and the alteration of the treatment strategy.

Aggressive lymphomas are characterized by a high growth rate and acute clinical course. Unlike indolent forms, which can be asymptomatic for several years, aggressive lymphomas are usually symptomatic already at the early stages and must be treated rapidly. Amongst them, the most common is the DLBCL, representing around 30-40% of all NHLs.[38] One of the most highly proliferative subtypes is BL, which is characterized by exceptionally rapid cellular proliferation and is frequently associated with Epstein–Barr virus (EBV) infection.[39] The clinical presentation of aggressive lymphomas arises rapidly and is also associated with B symptoms, i.e., persistent fever, excessive night sweats, and involuntary weight loss. Other common presentations include lymphadenopathy, abdominal pain, and, in late presentations, extranodal involvement with organ dysfunction. Diagnosis is established by lymph node biopsy, with further histopathological and molecular analysis to identify the exact genetic alterations. Imaging modalities, such as positron emission tomography-computed tomography and magnetic resonance imaging, are important for staging the disease and for follow-up of treatment.[40] The treatment of most aggressive lymphomas starts with a combination of chemotherapy and immunotherapy; for DLBCL, the initial treatment is with rituximab, cyclophosphamide, doxorubicin, vincristine and prednisone (R-CHOP). For relapsed or refractory disease, autologous stem cell transplantation is a significant treatment approach, as it allows high-dose chemotherapy.[41] Radiotherapy may also be employed in some circumstances, particularly if the lymphoma is localized or involves the CNS.[42] Thanks to advances in therapeutic approaches, the prognosis of aggressive lymphomas has significantly improved, and a high percentage of patients achieve complete remission. Five-year survival rate of DLBCL ranges from 60% to 80% depending on disease characteristics and response to therapy.[43] Nevertheless, the risk of relapse requires regular monitoring with periodic clinical evaluations and molecular examinations to detect early signs of progression and adjust treatment strategies

appropriately. Early diagnosis and treatment are the key to maximise remission rates and improve survival rates.

Accounting for 30-40% of all cases worldwide, DLBCL is the most common subtype of NHL. It is an aggressive and rapidly growing B-cell malignancy with a highly variable clinical course. The disease mainly affects adults, with an average age of presentation of around 60 years, although younger patients can also be affected. The incidence is slightly higher in men than women.[44] A multitude of risk factors are involved in its onset, including genetic predisposition, immunodeficiency states like acquired immunodeficiency syndrome or post-transplant immunosuppression, chronic infections such as EBV and Hp, and autoimmune disorders. Environmental exposures, such as pesticide and radiation, and previous chemotherapy or radiotherapy for other cancers may also increase the risk of secondary DLBCL.[45,46]

DLBCL arises from the malignant transformation of B cells at the germinal centre or post-germinal centre stage. The germinal centre B-cell-like subtype has a more favourable prognosis and response to immunochemotherapy, with common translocations targeting BCL-2, and abnormalities in the PI3K/Akt signalling pathway. The activated B cell-like subtype originates from post-germinal centre B cells and is linked with poorer prognosis.[47] Clinically, DLBCL generally occurs with rapidly enlargement of lymph nodes, most frequently in the cervical, axillary, or inguinal areas. Extranodal involvement occurs in approximately 40% of cases, including the gastrointestinal tract, CNS, bone marrow, and skin.[38] Systemic symptoms such as fever, night sweats and unexplained weight loss, known collectively as B symptoms, occur in about 30% of patients. The first-line treatment of DLBCL is chemoimmunotherapy R-CHOP with complete remission rates of 60–70%.[48] More aggressive regimens such as dose-adjusted EPOCH-R (etoposide, prednisone, vincristine, cyclophosphamide, doxorubicin, and rituximab) can be employed in high-risk disease.[49] In relapsed or refractory disease, salvage regimens like R-ICE (rituximab, ifosfamide, carboplatin, and etoposide) or R-DHAP (rituximab, dexamethasone, high-dose cytarabine, and cisplatin) followed by autologous stem cell transplantation can be employed. However, treatment options are limited for patients who are ineligible for transplantation or who have primary refractory disease, and novel therapies are needed.[50]

In recent years, targeted therapies have been developed, particularly for relapsed or refractory DLBCL. BTK inhibitors, such as ibrutinib, showed to be effective in the activated B-cell subtype.[51] Venetoclax is a BCL-2 inhibitor, it was investigated for its ability to reverse

apoptotic resistance in BCL-2 overexpressing tumours.[52] Table 1 provides a comparative overview of their key clinical and biological differences.

Table 1. Main pathological differences between HL and NHL.

	HL	NHL
Cells of origin	Mature B cells	B cells, T cells, or NK cells (less frequently)
Diagnostic marker	Presence of RSCs	Absence of RSCs
Incidence	Less common (10% of all lymphomas)	More common (90% of all lymphomas)
Age of onset	Young adults (15–35) and older adults (>55)	Increases with age; median onset 60 years
Spread pattern	Contiguous lymph nodes involvement	Non-contiguous, multiple extranodal sites
Site of presentation	Cervical, mediastinal, and supraclavicular lymph nodes	Lymph nodes, Gastrointestinal tract, skin, CNS, bone marrow
Extranodal involvement	Rare in early stages	Common
Systemic "B" symptoms	Frequently present	Variable; more common in aggressive subtypes
Prognosis	Generally excellent (5-year survival 89%)	Highly variable; depends on subtype
Treatment approach	ABVD chemotherapy + radiotherapy	Chemoimmunotherapy (e.g., R-CHOP), CAR-T, small molecules, antibodies

3. THE ROLE OF SIRTUIN 6 IN DLBCL

Despite these advances, there is still a high percentage of patients with treatment failure and further studies into the molecular pathogenesis of DLBCL initiation and resistance are needed. To identify novel therapeutic targets for DLBCL, I conducted a target analysis from *The Human Protein ATLAS* database (www.proteinatlas.org) and identified Sirtuin 6 (SIRT6) as a protein broadly expressed in lymphoma cells (Figure 2).

SIRT6 is a protein that plays a pivotal role in the regulation of essential cellular processes including DNA repair, gene expression, and telomere maintenance. In 2020, Yang and colleagues conducted a comprehensive analysis of publicly available microarray datasets to explore the involvement of SIRT6 in lymphoid malignancies, with a specific focus on DLBCL.[53] Their findings revealed that SIRT6 is significantly upregulated in DLBCL tissues and cell lines compared to reactive lymphoid hyperplasia and peripheral blood mononuclear cells (PBMC) from healthy donors. This overexpression was positively associated with older age, higher International Prognostic Index scores, and more advanced clinical stages, suggesting that SIRT6 may serve as a prognostic biomarker to identify patients with a potentially more aggressive disease course. Functional studies demonstrated that SIRT6 knockdown suppressed DLBCL proliferation both *in vitro* and *in vivo*, exerting therapeutic effects by modulating DNA damage response pathways, inducing G_2/M cell cycle arrest, and promoting apoptosis. Furthermore, recent evidence suggests that SIRT6 promotes the Warburg effect in cancer cells by enhancing the production of reactive oxygen species (ROS). Notably, inhibition of ROS has been shown to reverse this metabolic shift.[54] RNA-seq-based Gene Set Enrichment analysis identified functional enrichment of SIRT6 in PI3K/Akt and Forkhead box O (FoxO) signaling pathways, implicating it in survival and proliferation pathways relevant to DLBCL pathogenesis.[55] Taken together, these findings support the hypothesis that SIRT6 may represent a novel and promising molecular target for the development of therapeutic strategies aimed at treating aggressive forms of DLBCL.

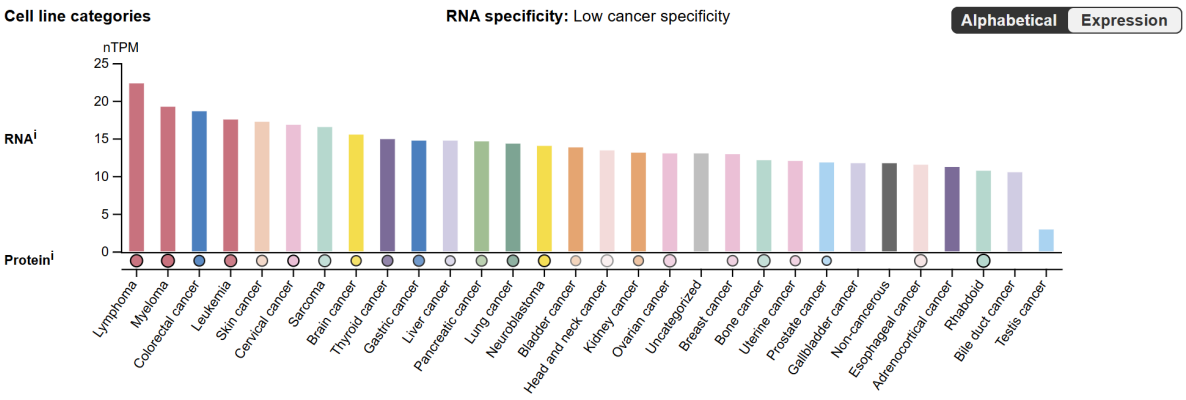

Figure 2. Expression of SIRT6 in cancer cell lines. The figure is comparatively showing RNA level (nTPM) and Protein level (nRPX) of various cell line groups of SIRT6 gene. In lymphoma, SIRT6 is detected in 39/40 cell lines. RNA expression data as normalized Transcript per Million (nTPM) values of cancer cell lines. The plot shows each individual nTPM of the SIRT6 gene in each cell line. *Source: The Human Protein ATLAS.*

3.1 SIRTUINS

Sirtuins (SIRTs) are a family of NAD^+-dependent histone deacetylases that play essential roles in the regulation of chromatin structure, gene expression, metabolism, and cellular homeostasis. In mammals, SIRTs family comprises seven isoforms (SIRT1–7), which share a conserved catalytic core of approximately 275 amino acids but differ in their N- and C-terminal domains, contributing to their distinct subcellular localization and functional specificity.[56] Unlike classical histone deacetylases (HDACs), SIRTs belong to a subgroup of the broader HDAC superfamily, which is traditionally classified into Zn^{2+}-dependent HDACs and NAD^+-dependent SIRTs based on catalytic mechanisms. The Zn^{2+}-dependent HDACs are further grouped into class I (HDAC1–3, 8), class II (HDAC4–7, 9, 10), and class IV (HDAC11) according to their sequence similarity with yeast deacetylases.[57,58] SIRTs have been extensively studied for their involvement in a wide range of physiological and pathological processes. Altered activity of SIRTs has been associated with cancer, neurodegenerative diseases, cardiovascular disorders, and metabolic dysfunctions.[59,60] Structurally, all SIRTs share a common catalytic region that includes a Rossmann fold and a small Zn^{2+} binding domain that surround a groove containing the binding sites for both substrate and NAD^+.[61]

The Rossmann fold domain contains a β-sheet of six parallel β-strands surrounded by a variable number of α-helices. This number varies depending on the SIRT isoform. The conserved GxG motif, which is crucial for phosphate interaction, a NAD^+-binding pocket, and charged amino acids that boost the affinity for the ribose moiety are all features of this organization, which is typical of NAD^+/NADH-binding proteins.[62] A single globular domain has two insertions that originate from the Rossmann fold. One of these insertions has simply a structural role and binds Zn^{2+} through four conserved cysteine residues.[63,64] Through β-sheet-like interactions with two neighbouring loops, substrate binding brings the Zn^{2+}-binding domains and Rossmann fold closer together. The so called *β-staple* results from the conformational shift of the enzyme from an open to a closed state, which is facilitated by these interactions. SIRTs share a similar deacylation mechanism.[63,64] After binding of the acylated substrate to the enzyme, the carbonyl oxygen of the acyl group attacks the ribose at position C1', resulting in the displacement of nicotinamide (NAM) and producing the intermediate O-alkylamidate. Then, a conserved histidine acts as base and leads to the deprotonation of the hydroxyl group in position 2′ which attacks, in turn, the imine carbon of O-alkylimidate intermediate, thus producing a cyclic intermediate C1′/C2′, which is

finally hydrolysed, restoring the deacylated protein and producing 2′-O-acyl-adenosine diphosphate(ADP)-ribose as reaction products.[65] The mechanism is depicted in Figure 3.

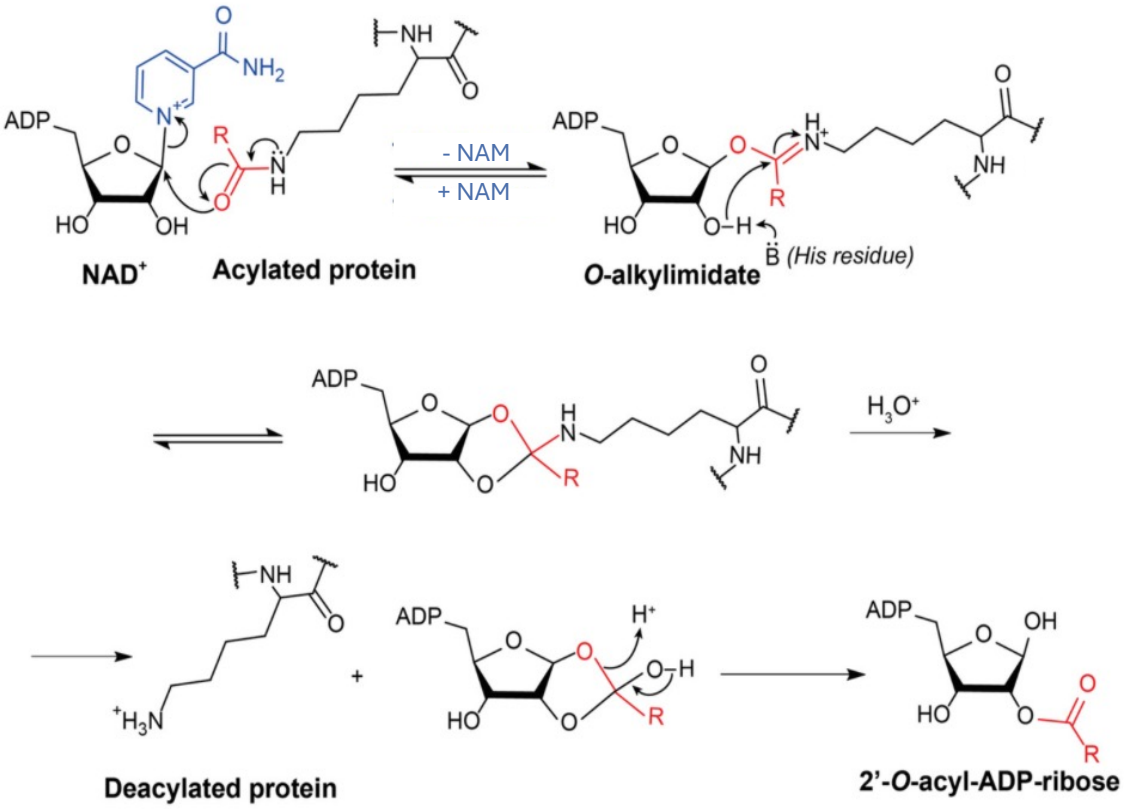

Figure 3. SIRT-catalyzed deacetylation reaction mechanism. The reaction involves the NAD^+-dependent deacetylation of ε-acetyl-lysine residues on target proteins.

Small changes in the binding site of each isoform, along with differences at the N- and C-terminal level, affect substrate specificity and cellular localisation, as well as interaction with modulators and other proteins. Indeed, the seven mammalian SIRTs regulate the acylation state of a wide range of protein. In particular, SIRT1-3 has a predominantly protein lysine deacetylase activity, although SIRT2 was also found to show a demyristoylase activity. SIRT4, on the other hand, exhibited deacetylase, decarbamylase, lipoamidase and mono-ADP-ribosyltransferase activities and catalyses the removal of 3-hydroxy-3-methyl-glutaryl moieties from the lysine residues of proteins.[66] SIRT5 has weak deacetylase activity and prefers negatively charged acyl chains, thus possessing significant deglutarylase, desuccinylase and demalonylase activities.[67,68] SIRT6 also has deacetylase activity and has preferential activity towards long-chain fatty acyl chains (e.g. myristoyl) and also exhibits mono-ADP-ribosyltransferase activity.[69] Finally, SIRT7 possesses deacetylase and desuccinylase activity,[70] and recently showed to possess self-ADP-ribosylation[71] and broad-

spectrum deacylase activity. The catalytic activity of SIRTs is modulated through several mechanisms, including protein-protein interactions, post-translational modifications and binding of endogenous molecules.

3.2 SIRT6

SIRT6 is predominantly located in the nucleus and involved in multiple biological processes, notably in genomic maintenance, transcriptional regulation, and metabolic control (Figure 4). It displays a range of enzymatic activities, including deacetylation, long-chain fatty acyl deacylation, and mono-ADP-ribosylation, which are associated with cellular protection and organismal longevity.[72,73] Functionally, SIRT6 contributes to chromatin remodeling by deacetylating histone marks such as H3K9ac and H3K56ac at specific genomic loci, thereby modulating gene expression and facilitating DNA repair.[74–76] For instance, repression of *c-Myc*, NF-κB target genes, and genes involved in ribosomal biogenesis and early development has been linked to SIRT6-dependent histone modification.[77,78]

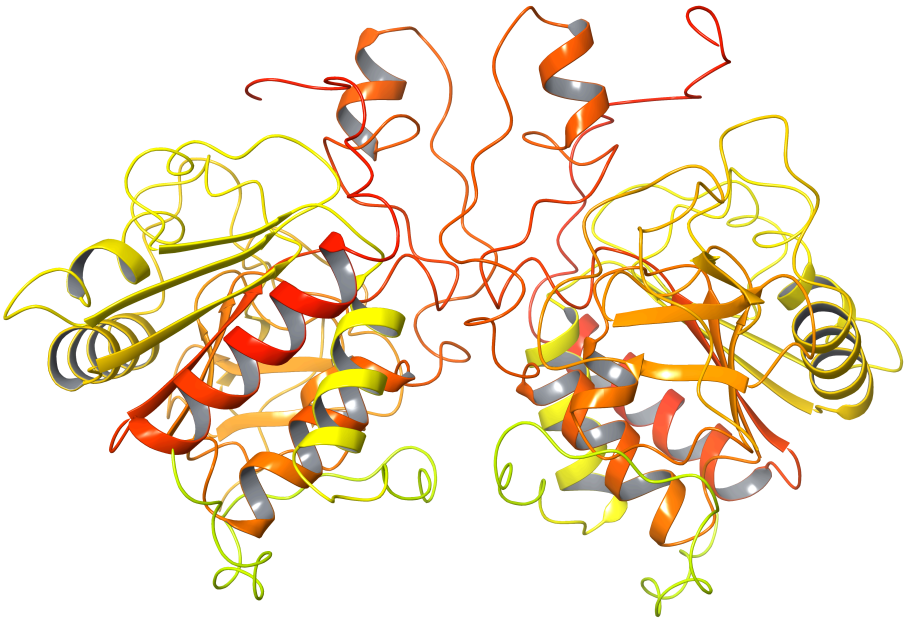

Figure 4. Three-dimensional structure of the apo form of human SIRT6.

SIRT6 is a key regulator of aging, acting through mechanisms such as the preservation of telomere integrity, enhancement of DNA damage response, maintenance of metabolic homeostasis, and modulation of the senescence-associated secretory phenotype. Mouse models deficient in SIRT6 show severe developmental defects and early postnatal lethality, while SIRT6 overexpression has been associated with extended lifespan and improved metabolic function.[79]

SIRT6 can act as tumour suppressor in several malignancies, where it regulates key pathways involved in proliferation and apoptosis. In nasopharyngeal carcinoma, SIRT6 induces apoptosis by downregulating BCL-2 and upregulating cleaved caspase-3 and Bax,

acting through NF-κB inhibition.[80] In glioma, it suppresses tumour growth by repressing Poly(rC)-binding protein 2 (PCBP2) via H3K9ac deacetylation.[81] Similarly, in pancreatic ductal adenocarcinoma (PDAC), SIRT6 deficiency leads to histone hyperacetylation and aberrant activation of Lin28b, contributing to tumour progression.[82] Similarly, in breast cancer, ectopic expression of SIRT6 reduces glycolysis and tumour growth.[83]

Conversely, SIRT6 may also act as tumour promoter. Indeed, in papillary thyroid carcinoma, it increases ROS production, promotes the Warburg effect,[84] and downregulates E-cadherin, thereby enhancing migration and invasion.[85] In non-small-cell lung cancer (NSCLC), SIRT6 activates the ERK1/2–MMP9 axis and promotes cell proliferation, while its silencing impairs tumour growth.[86,87] In hepatocellular carcinoma (HCC), SIRT6 is associated with poor prognosis, facilitates epithelial–mesenchymal transition (EMT) via E-cadherin degradation, and promotes survival through repression of Bax and activation of the Akt pathway.[88,89] Similar effects have been observed in prostate cancer, where SIRT6 enhances BCL-2-mediated chemoresistance,[90] and in colon cancer, where it drives EMT and represses tumour suppressors such as TET1.[91] As previously described, SIRT6 expression also decreases sensitivity to chemotherapy, apoptosis rates and cell cycle arrest between the G2/M phases in DLBCL.[53] Given the multifaceted roles of SIRT6, the development of selective inhibitors has emerged as a promising strategy to modulate its activity in a disease-specific context.[92]

In the last years, several molecules have been identified as SIRT6 inhibitors (Figure 5). Trichostatin A (TSN, **1**) is a well-known pan-HDAC inhibitor that has been recently identified as a SIRT6 inhibitor with partial selectivity over SIRT1–3 and SIRT5. Although TSN showed potent nanomolar inhibition against classical Zn^{2+}-dependent HDACs, its inhibition of SIRT6 occurs in the micromolar range. Kinetic studies reported Ki values of 2.02 μM using an H3K9Ac substrate and 4.62 μM with a p53K382Ac peptide.[93] Notably, TSN acts as a competitive inhibitor with respect to the acetylated substrate but does not compete with NAD^+. Crystallographic analysis of the SIRT6–TSN–ADP-ribose ternary complex revealed that TSN binds to both the nicotinamide binding pocket and the acyl channel of the active site.[94]

A series of quinazolinedione-based inhibitors (**2a-d**) have shown moderate SIRT6 inhibition, with IC_{50} values ranging from 37 to 106 μM.[95] Among them, **2d** displayed the highest selectivity profile, being 133-fold more selective for SIRT6 over SIRT1 and exhibiting no activity against Zn^{2+}-dependent HDACs. Compound **2c**, though slightly less selective, was the most potent of the series (IC_{50} = 37 μM) and demonstrated enhanced

glucose uptake in PDAC cells. Furthermore, both **2b** and **2c** sensitized BxPC3 cells to gemcitabine, and **2c** also potentiated the efficacy of olaparib in Capan-1 cells. Notably, **2a** has been reported to prevent muscle atrophy *in vivo*.[95]

A high-throughput screen of approximately 2,000 compounds identified 1-(4-nitrophenyl)piperazine (**3a**) as a fragment-like SIRT6 inhibitor, with an IC_{50} of 35 μM. Subsequent structural optimization led to 5-(4-methylpiperazin-1-yl)-2-nitroaniline (**3b**), which exhibited an improved IC_{50} of 4.9 μM and strong selectivity over SIRT1–3 and HDAC1–11.[96] In BxPC-3 cells, **3b** induced a dose-dependent increase in H3K9 and H3K18 acetylation. In a mouse model of type 2 diabetes, **3b** reduced blood glucose levels via upregulation of glucose transporter expression, highlighting its potential for metabolic intervention.[96]

Ageladine A, a marine-derived metalloproteinase inhibitor, served as the scaffold for the design of the SIRT6-selective inhibitor 2-(6-(4-(4,5-dibromo-1*H*-pyrrol-2-yl)-1*H*-imidazo[4,5-c]pyridin-1-yl)hexyl)-1,1,3,3-tetramethylisothiouronium bromide (**4**). Compound **4** demonstrated cellular activity, significantly increasing H3K9 acetylation in HeLa cells at low micromolar concentrations.[97] Selectivity profiling showed no inhibition of SIRT3, SIRT5, or HDAC1/2/4/5/7/9–11, while moderate inhibition was observed for SIRT1, SIRT2, and HDAC3/6/8 (IC_{50} 80-112 μM). In PDAC cells, **4** induced cell cycle arrest and apoptosis, blocked cell proliferation (IC_{50} 7-9 μM), and inhibited angiogenesis-related signaling pathways (e.g., N-cadherin, VEGFR2, HIF-1α). *In vivo*, **4** was well tolerated and sensitized pancreatic tumour xenografts to gemcitabine.[97,98]

Zhang *et al.* identified an allosteric pocket in SIRT6 that becomes accessible upon NAD^+ binding and designed the allosteric inhibitor (*E*)-1-(4-amino-1,2,5-oxadiazol-3-yl)-*N*′-(3-chloro-5-(trifluoromethyl)benzylidene)-1*H*-1,2,3-triazole-4-carbohydrazide (JYQ-42, **5**). This molecule inhibited SIRT6 with an IC_{50} of 2.33 μM, showed non-competitive inhibition toward both acetylated peptide and NAD^+, and exhibited high selectivity over other SIRTs and HDACs (except weak inhibition of SIRT2, IC_{50} = 87.2 μM).[99] In PDAC cells (BxPC-3 and MiaPaCa-2), **5** increased acetylation levels of H3K9, H3K18, and H3K56, reduced cytokine production (IL-6, IL-8, TNF-α), and impaired cell migration without affecting proliferation.[99]

A recent structure-based drug design campaign yielded two allosteric inhibitors, the carboxamide derivatives **6a** and **6b**, with IC_{50} values of 0.98 and 1.80 μM, respectively.[100] Compound **6a** increased H3K9, H3K18, and H3K56 acetylation in both human (BxPC-3, L3.6PL, SW1990) and murine (PANC-02) PDAC cell lines, inhibited cell migration, and

reduced liver metastases in xenograft mouse models. Importantly, **6a** displayed no cytotoxicity up to 100 μM and did not interfere with SIRT6 substrate or NAD^+ binding, confirming its allosteric mode of action.[100]

Recent studies have revealed that SIRT6 contributes to breast cancer progression by promoting drug resistance through enhancement of DNA damage repair mechanisms. In this context, a structure-based drug discovery approach combined high-throughput virtual screening and Fluor-de-lys assays to identify a novel hit compound featuring a β-carboline scaffold (**7a**). Guided by sequence and structural differences across the SIRTs family, a series of sixty derivatives modified at positions 3, 6, and 9 in the pyrido[3,4-*b*]indole moiety was synthesized. Among them, compound **7b** emerged as a potent and selective SIRT6 inhibitor, with an IC_{50} of 5.81 μM and more than 27-fold selectivity over other isoforms. Structural modeling identified Phe64, Met157, and Ser56 as critical residues mediating the interaction with **7b**. Functionally, **7b** inhibited the deacetylase activity of SIRT6, suppressed proliferation, migration, and invasion, and induced apoptosis in MCF-7 breast cancer cells by impairing DNA damage repair. Moreover, *in vivo* studies confirmed its efficacy and safety, supporting the therapeutic potential of targeting SIRT6 in breast cancer using β-carboline-based inhibitors.[101]

The 5-(3-(furan-2-carboxamido)benzamido)-2-hydroxybenzoic acid (OSS_128167, **8**) is a selective small-molecule inhibitor targeting SIRT6. With an IC_{50} of 89 μM for SIRT6, compound **8** exhibits significantly lower affinity for SIRT1 and SIRT2 (IC_{50} values of 1,578 and 751 μM, respectively). In the context of oncology, **8** has demonstrated potential therapeutic effects for the treatment of DLBCL. Indeed, **8** led to increased apoptosis, cell cycle arrest, and enhanced sensitivity to chemotherapeutic agents.[102]

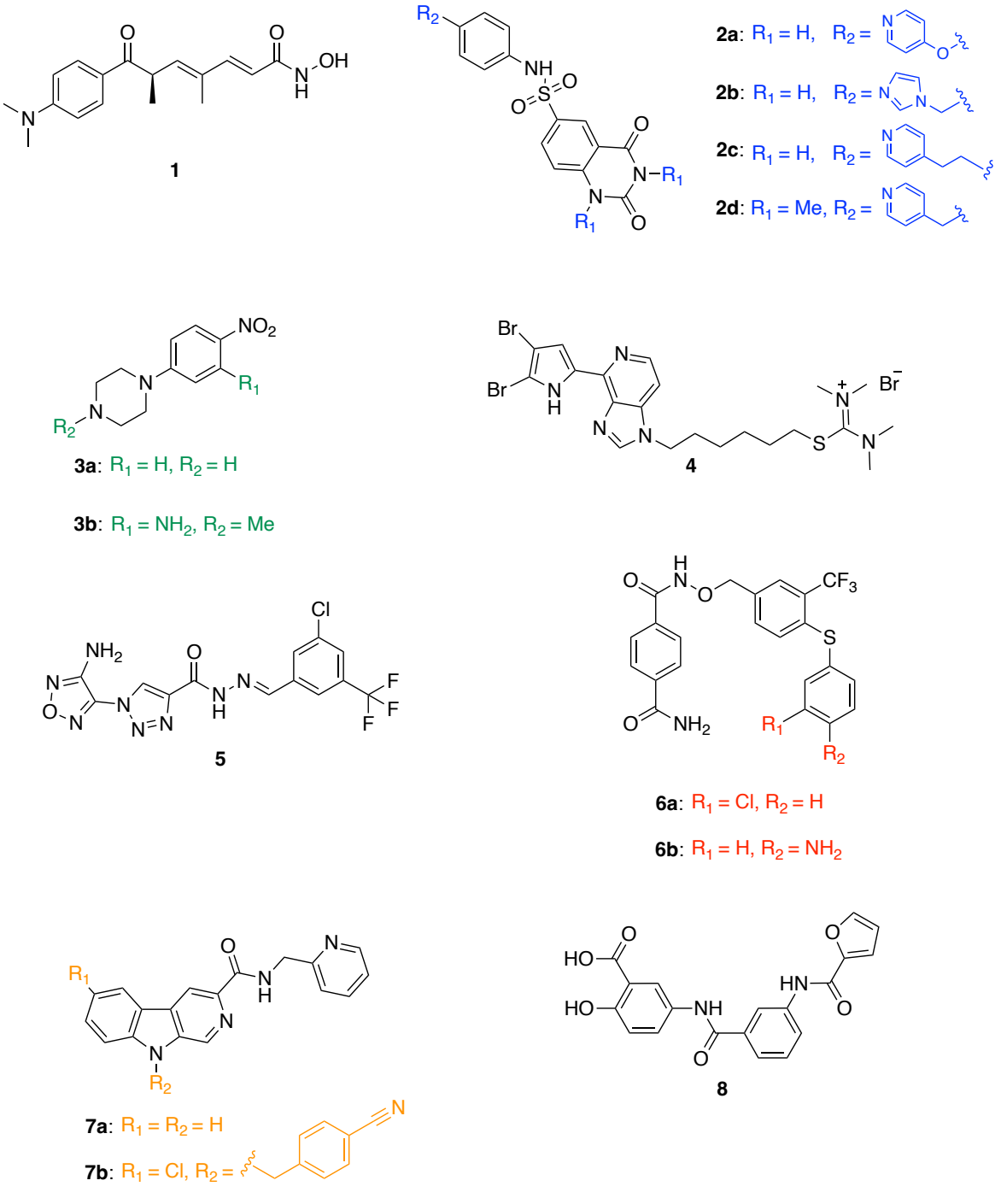

Figure 5. Structure of the most representative SIRT6 inhibitors.

4. AIM OF THE PhD THESIS

The aim of my PhD thesis was the design, synthesis, and biological evaluation of novel small molecules targeting SIRT6, within the framework of a drug discovery project in the field of haematological malignancies.

To achieve these goals, the research project included *in silico* approaches, employing molecular docking, molecular dynamics simulations and binding pose metadynamics, to gain mechanistic insights into SIRT6-ligand interactions thus identifying new inhibitory chemotypes through virtual screening campaigns performed on publicly available databases and in-house libraries. Computational studies moved to the synthetic approach, where selected hit compounds and their analogues were synthesized using different synthetic methodologies, with particular emphasis on microwave-assisted synthesis to achieve high efficiency, improved yields, and reduced reaction times. Comprehensive chemical characterization and purification protocols were applied to ensure the quality of the synthesized compound. Biological evaluation included enzymatic inhibition assays to determine SIRT6 activity modulation, as well as cellular assays on B-cell lymphoma models, such as SU-DHL-8 cells which express SIRT6. The cellular studies aimed to investigate the effects of SIRT6 inhibition on cell viability, proliferation, and cell cycle progression, as well as the selectivity towards non-tumorigenic cells, for instance peripheral blood mononuclear cells. By combining computational design, microwave synthetic methodologies, and thorough biological evaluation, this PhD thesis aimed to understand SIRT6's functional role in B-cell lymphomas and to establish a foundation for the development of new therapeutic approaches targeting this epigenetic enzyme.

5. RESULTS AND DISCUSSION

5.1 Binding site analysis

To pursue my research project, I adopted a combined computational and experimental approaches. I began my investigation by exploring the Protein Data Bank (PDB - www.rcsb.org) in search of crystallographic structures of human SIRT6 suitable for structure-based drug design. At the time of this study, twenty-one SIRT6 structures were deposited on the PDB and, among the available structures, only eleven SIRT6 entries were in complex with a modulator and the ADP-ribose. Specifically, PDB IDs 5MF6, 5MFP, 5MFZ, 5MGN, 6XVG, 6QCD, 6QCE, and 6QCH contained an activator, PDB IDs 6XV1 included an allosteric activator, and only two structures, 6HOY and 6QCJ, were co-crystallized with an inhibitor. The remaining entries were apo structures, with no ligand bound in the active site as reported in Table 2.

Table 2. List of the deposited human SIRT6 crystals.

PDB ID	Ligand	Activity	Resolution (Å)
3K35	None	None	2.00
3PKI	None	None	2.04
3PKJ	None	None	2.12
3ZG6	None	None	2.20
5MF6	UBCS039	Activator	1.87
5MFP	UBCS058	Activator	1.98
5MFZ	UBCS040	Activator	2.10
5MGN	UBCS038	Activator	2.07
5Y2F	MDL-801	Activator	2.53
6HOY	TSN	Inhibitor	1.70
6QCD	Quercetin	Activator	1.84
6QCE	Isoquercetin	Activator	1.90
6QCH	Cyanidin	Activator	2.10
6QCJ	Catechin gallate	Inhibitor	2.00
6XUY	None	None	2.13
6XV1	MDL-801	Allosteric activator	1.95
6XV6	None	None	1.75
6XVG	MDL-801	Allosteric activator	2.10
6ZU4	Fluvastatin	Activator	2.46
7CL0	None	None	2.53
7CL1	MDL-801	Allosteric activator	3.2

All the structures were imported on Maestro (Schrödinger, New York, 2021-1) and optimized using the Protein Preparation Wizard.[103] Hydrogen atoms were added, and missing loops and side chains were reconstructed. The protein preparation was carried out

at a pH of 7.4 ± 0.2. The resulting structure was then energy-minimized using OPLS4 as force field.[104] Sulfate ions were removed, whereas Zn^{2+} ions were retained, as they are known to be structurally essential, although not catalytically active for this isoform. The binding sites of the prepared protein structures were visually inspected in order to assess the correct orientation of the key residues, the presence of structural water molecules, and the accessibility of the active site. Particular attention was paid to the integrity of the catalytic pocket and to the spatial arrangement of residues known to be involved in ligand binding, such as Ala53, Ile61, Pro62, Val115, and Asp116. This inspection confirmed the absence of steric clashes or artifacts generated during the protein preparation process and validated the suitability of the resulting structures for subsequent docking studies and molecular dynamics simulations. Upon analysis of the binding pockets, I observed that both activators and inhibitors bound to the same pocket, whereas ADP-ribose was found to bind to a distinct site. Based on this evaluation, I selected four crystal structures, all with a resolution equal to or better than 2 Å, for further analysis: two co-crystallized with inhibitors (PDB IDs: 6HOY and 6QCJ) and two with activators (PDB IDs: 5MF6 and 6QCD). As initial step, I performed a re-docking of all ligands examined in order to assess whether the docking software was able to reproduce the original orientation and conformation of the co-crystallized ligands. This comparison is evaluated in terms of the Root Mean Square Deviation (RMSD), which quantifies the level of agreement between the predicted binding pose and the experimental structure, thus measuring of the reliability of the docking protocol. Following the superimposition of the predicted and experimental structures, RMSD was calculated, and a visual inspection of the aligned structures was also performed to evaluate the spatial correspondence of key interactions. Results are reported in Table 3.

Table 3. RMSD values after re-docking after superimposition.

PDB ID	Ligand	RMSD (Å)
5MF6	UBCS039	1.85
6HOY	TSN	2.65
6QCD	Quercetin	0.12
6QCJ	Catechin gallate	6.51

These RMSD values indicate discrepancies in docking accuracy between the docked and crystallographic poses, with particularly high accuracy observed for Quercetin (QUE), while significant deviation was observed for Catechin gallate.

Given these results, and in order to gain deeper insight into the distinct mechanisms of action of activators and inhibitors, I selected two representative crystal structures: one co-crystallized with the activator QUE, and the other with the inhibitor TSN. Both structures showed high resolution, specifically 1.84 Å for SIRT6-QUE and 1.70 Å for SIRT6–TSN. TSN is a potent and selective inhibitor of SIRT6, with a reported IC_{50} of 7.88 µM, the visual inspection of the binding site revealed that the hydroxamate moiety of TSN penetrated deeply into the active site. The carbonyl oxygen of the hydroxamic group established hydrogen bond interactions with residues Val115 and Asp116, while the hydroxyl group formed a direct interaction with Asp116. Furthermore, the nitrogen atom of the hydroxamic acid was involved in a water-bridge mediated hydrogen bond with Ala53 and Ile61. The phenyl-dimethylamine aromatic ring was involved in π–π stacking interactions with Trp71, whereas the aliphatic chain appeared not to be involved in any significant interactions. In addition, several van der Waals interactions were observed involving key residues such as Val115, Asp116, Met136, Met157, Ile61, Asp63, Phe64, Val70, Phe82, and Phe86 (Figure 6).

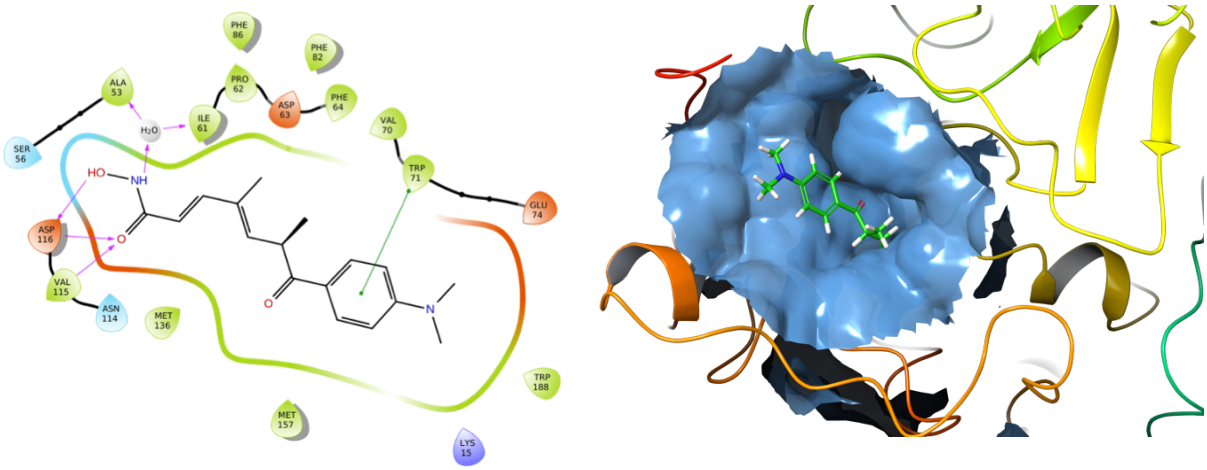

Figure 6. Ligand Interaction Diagram and 3D representation of the experimental pose of SIRT6-TSN (PDB ID: 6HOY).

QUE, a natural flavonoid compound widely studied for its antioxidant, anti-inflammatory, and potential anticancer properties, is reported as a SIRT6 activator with an EC_{50} of 990 µM. I performed the same structural analysis for the SIRT6–QUE complex. More specifically, one hydroxyl group of the catechol moiety established a H-bond with Pro62, and several van der Waals interactions were observed with the same residues involved in TSN binding, indicating a partially overlapping interaction pattern (Figure 7).

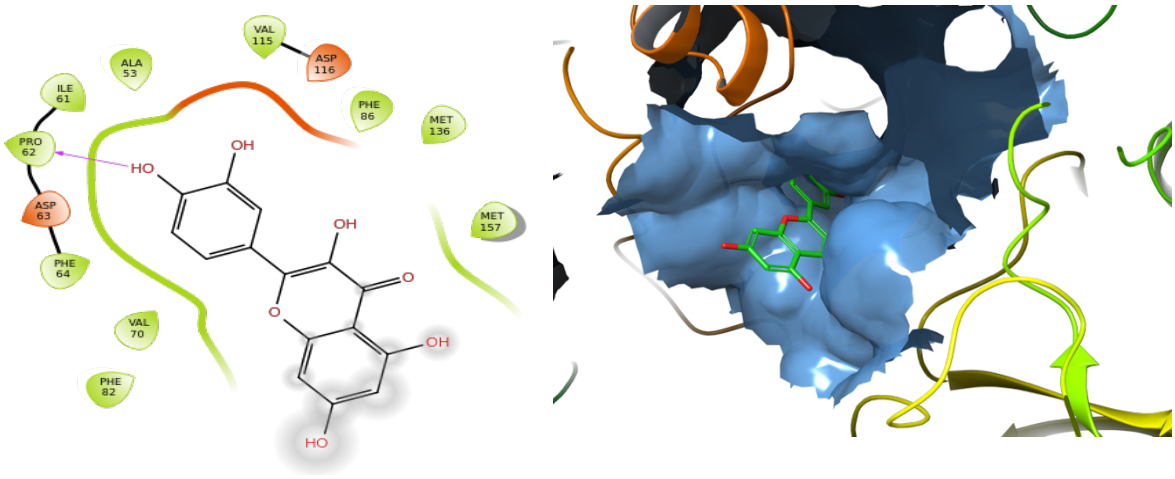

Figure 7. Ligand Interaction Diagram and 3D representation of the experimental pose of SIRT6-QUE (PDB ID: 6QCD).

5.2 Molecular Dynamics simulation of known activator and inhibitor

To elucidate the key interactions responsible for ligand stabilization within the SIRT6 binding site, I performed three independent molecular dynamics (MD) simulations of 500 ns for each protein–ligand complex (SIRT6–TSN and SIRT6–QUE). The choice of a time scale of 500 ns was motivated by the need to capture conformational changes of both protein and ligands, as well as the potential emergence of functionally relevant binding interactions that are often not visible in shorter simulations. This extended simulation time increases the probability of reaching equilibrium and provides statistically robust insights into the dynamic behavior of the complexes. The stability of the systems was assessed through trajectory analysis and root-mean-square deviation (RMSD) (Figure 8).

a)

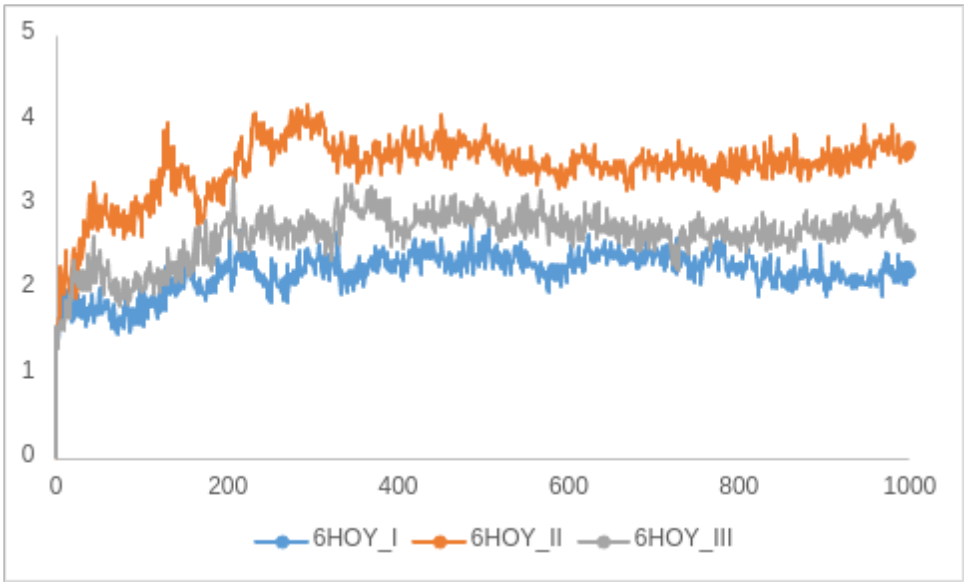

b)

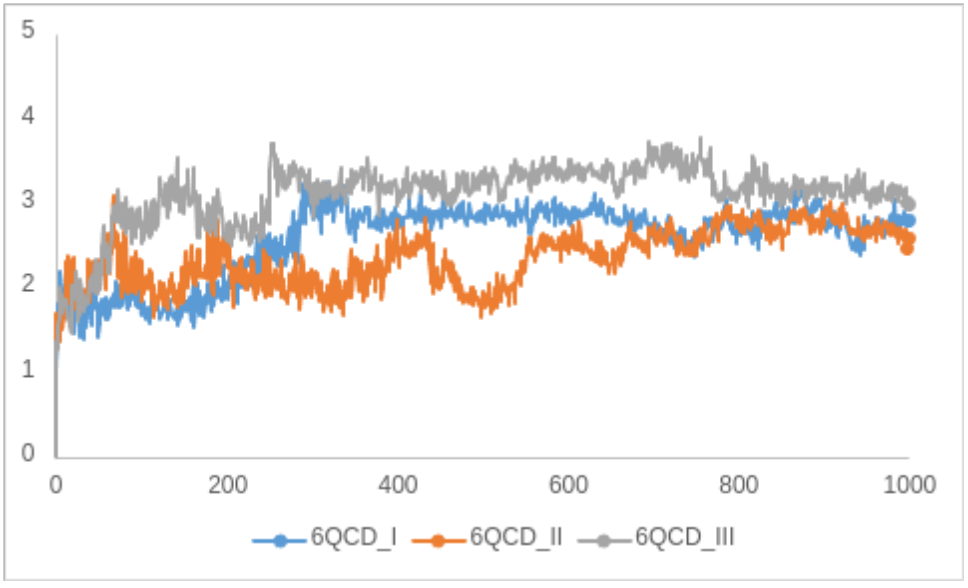

c)

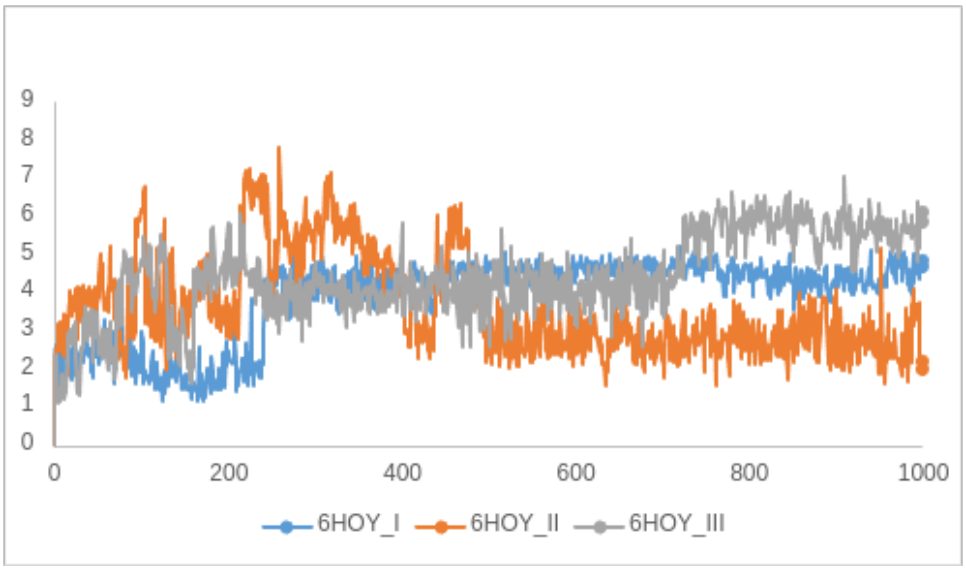

d)

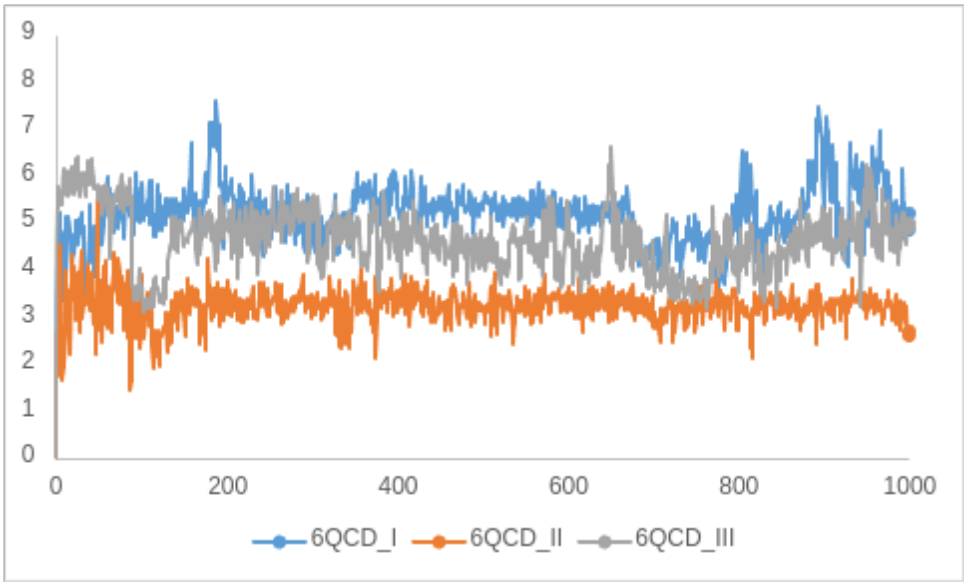

Figure 8 (a-b). Ligand Interaction Diagram and 3D representation of the experimental pose of SIRT6-QUE (PDB ID: 6QCD). Protein RMSD of SIRT6-TSN (PDB ID: 6HOY) SIRT6-QUE (PDB ID: 6QCD); **(c-d)** Ligand RMSD of SIRT6-TSN (PDB ID: 6HOY) and SIRT6-QUE (PDB ID: 6QCD) after 500 ns MD simulations.

Across all trajectories, both systems reached equilibrium, although with different conformational rearrangements. Protein RMSD values remained stable in all six simulations. In the SIRT6–TSN complex, only minor side chain fluctuations were observed, and these involved residues not directly engaged in ligand binding. In contrast, the QUE-bound system (PDB ID: 6QCD) exhibited more pronounced fluctuations in the 135–150 residues region, which is partially involved in ligand interactions. As a result, the TSN complex appeared overall more stable than the QUE complex. Ligand RMSD analysis was also performed to evaluate how firmly each ligand remained within the binding pocket. This measure was

obtained by aligning the complex trajectories on the protein backbone and calculating the RMSD of the ligand heavy atoms with respect to the reference frame. Both ligands remained bound within the active site throughout the simulations, although with different internal movement. In the TSN complex, increased RMSD values were attributed to the rotation of the terminal amino group. For the QUE complex, minimal fluctuations were observed, mainly due to rotational movements of the hydroxyl groups around their bond axes. A detailed evaluation of protein–ligand interactions provided insights into the dynamic stabilization of the complexes, revealing interactions not observable static crystallographic structures. These interactions were classified by type and represented as timelines (Table 4 and Figure 9).

Table 4. Target–ligands interactions were observed in the MD simulations. Int. is for interactions, HB is for H-bonds, Hphob is for hydrophobic interactions, and WB is for water bridges.

	MD					
	1st simulation		2nd simulation		3rd simulation	
Cpd	Residue	Int.	Residue	Int.	Residue	Int.
TSN	Ser56	HB	**Pro62**	HB	**Pro62**	HB
	Pro62	HB	**Val115**	HB, WB	**Val115**	HB, WB
	Val115	HB, WB				
	Trp188	HB				
QUE	Ser56	WB	**Pro62**	HB	**Phe64**	Hphob
	Pro62	HB, WB	**Phe64**	Hphob	**Phe82**	Hphob, HB, WB
	Phe64	Hphob	**Phe82**	Hphob	**Val115**	HB, WB
	Val115	WB, Hphob	Val154	HB, WB	Asp116	HB
	Leu186	HB, WB	Met157	WB, Hphob	**Trp188**	Hphob, WB
	Asp187	HB, WB				
	Trp188	Hphob				

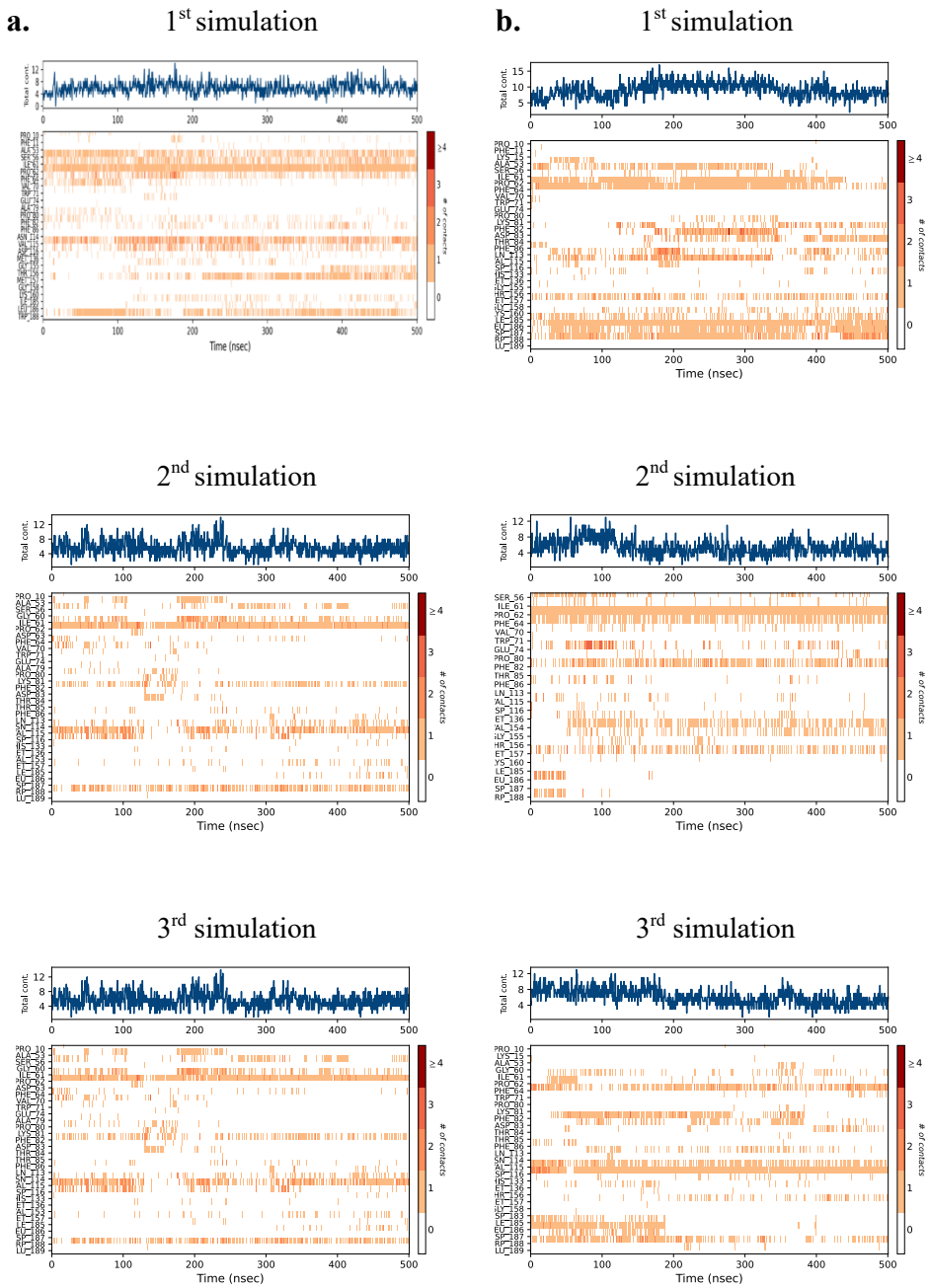

Figure. 9 Protein-ligand interactions (or "contacts") summarized in the timeline (**a.** PDB ID 6HOY; **b.** PDB ID 6QCD); the higher the number of contacts between the ligand and the protein, the darker the orange color is.

The MD analysis revealed that not all interactions observed in the crystal structures of TSN and QUE were maintained throughout the simulations; however, new contacts emerged that contributed to complex stabilization. For example, the interaction with Pro62 - present in the QUE crystal structure - was maintained in two out of three QUE simulations and, notably, also appeared in the TSN simulations, despite being absent in the original 6HOY structure. TSN binding was further stabilized by H-bonds with Ser56 and Val115, the latter occasionally mediated by water molecules interacting with the carbonyl oxygen of the

hydroxamic acid. Additional stabilization was provided by π–π stacking and hydrophobic interactions involving the aromatic ring and Trp188. For the QUE complex, the hydroxyl groups of the catecholic ring were involved in both direct and water-mediated hydrogen bonds with Ser56, Val115, Asp116, and Pro62. Furthermore, the catechol ring formed π–π stacking interactions with Phe64, and occasionally with Phe82. Additional stabilizing interactions were observed between the chromene hydroxyl group and residues Asp187, Leu186, and Val154, primarily mediated by water molecules.

5.3 Binding Pose Metadynamics

In addition, I performed a Binding Pose Metadynamics (BPMD) analysis to assess the relative binding stability of the two complexes, with the aim of identifying any differential behavior between the activator and the inhibitor. The results of this analysis are present in Figure 7. As shown in the plots, both compounds exhibited comparable PoseScore values: 2.632 for TSN and 3.106 for QUE (Figure 10). However, a more marked difference emerged when analyzing the persistence of H-bonds identified at the beginning of the metadynamics runs. In the case of TSN, these H-bonds were retained for only 14% of the average simulation time, whereas for QUE they persisted for 58% of the time. Furthermore, the CompScore values - an index combining geometric and energetic stability - were 1.922 for TSN and markedly lower at 0.196 for QUE. Based on these results, it is difficult to clearly distinguish a different binding behavior between the activator (i.e. QUE) and the inhibitor (i.e. TSN), suggesting that the dynamics of ligand stabilization within the SIRT6 binding pocket may involve more complex and context-dependent mechanisms than initially hypothesized.

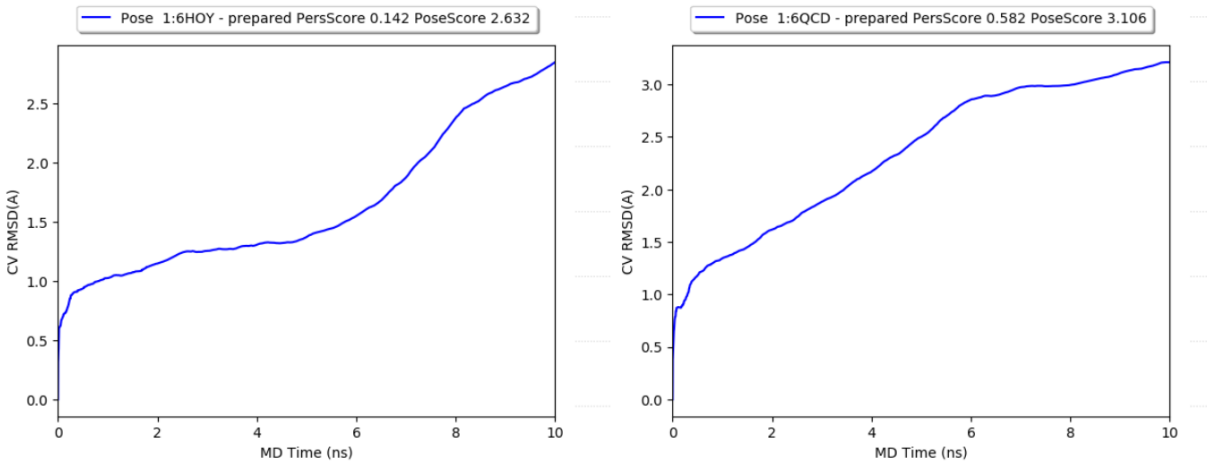

Figure 10. Plots of the RMSD estimate averaged over all 10 trials vs the simulation time for the Binding Pose Metadynamics runs: The blue lines represent the mean CV RMSD values along the 10 × 10 ns of the simulation trials (**Left.** PDB ID 6HOY; **Right.** PDB ID 6QCD).

The two compounds seemed to interact with the same residues after long molecular dynamics simulations in which it was not evident a peculiar behavior. The use of a biased MD approach such as BPMD showed an efficient ligand stability of both compounds, with QUE showing a CompScore >10 fold than TSN (0.196 vs 1.922, respectively).

5.4 Fragment-Based Virtual Screening

For the reasons outlined above, I selected the structure of the SIRT6–TSN complex (PDB ID: 6HOY) as the template for a molecular docking-based Virtual Screening (VS) campaign. I carried out a virtual screening campaign on a dataset of over 25,000 molecules, selected from both the ChEMBL database (www.ebi.ac.uk/chembl/) and in-house compound libraries. All molecules were docked into the SIRT6 active site using the Standard Precision (SP) mode. Docking poses were ranked according to their docking scores, and the top 5% of hits - those with the most favourable predicted affinities - were visual inspected to evaluate their interaction with key residues within the binding site. From this refined subset, nine compounds showing both optimal binding poses and docking scores superior to that of TSN were selected for biological validation (Figure 11, Table 5).

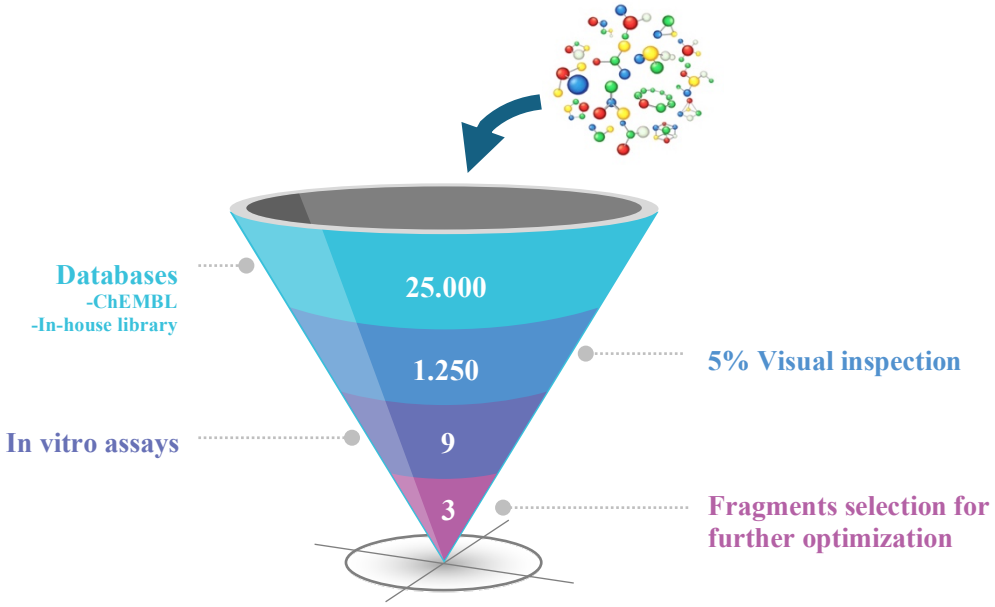

Figure. 11 Funnel infographics of the VS process using PDB ID 6HOY.

Table 5. Structure of the compounds selected through Virtual Screening.

Cpd.	Structure	Docking scores (Kcal/mol)	Smiles
9	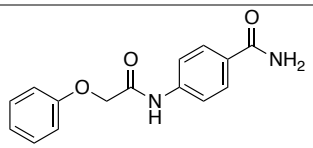	-7.212	O=C(C1=CC=C(C=C1)NC(COC2=CC=CC=C2)=O)N
10	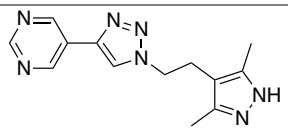	-7.365	CC1=NNC(C)=C1CCN(N=N2)C=C2C3=CN=CN=C3
11	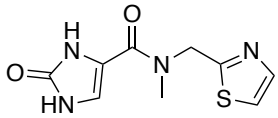	-6.224	O=C1NC=C(C(N(C)CC2=NC=CS2)=O)N1
12	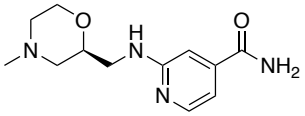	-7.087	NC(C1=CC(NC[C@@H]2OCCN(C)C2)=NC=C1)=O
13	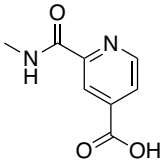	-6.962	O=C(NC)C1=CC(C(O)=O)=CC=N1
14	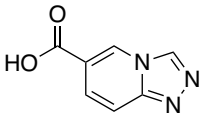	-6.260	OC(C(C=C1)=CN2C1=NN=C2)=O
15	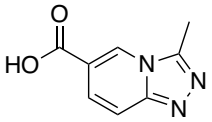	-6.352	OC(C(C=C1)=CN2C1=NN=C2C)=O
16	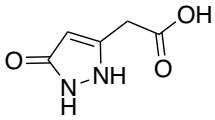	-6.964	O=C1NNC(CC(O)=O)=C1
17	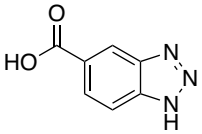	-5.807	OC(C1=CC2=NNN=C2C=C1)=O

Compound **9** was available as powder, while compounds **10-17** were provided as 10 mM solutions in dimethyl sulfoxide (DMSO). All compounds were analyzed by HPLC-Mass spectroscopy to rapidly assess sample integrity and purity. LC-MS analyses were performed using a Shimadzu LCMS-2020 instrument. Sixteen-minute runs were optimized individually for each sample, employing water and acetonitrile (ACN) as mobile phases and a C18 reversed-phase column. For **12** and **16**, a satisfactory chromatographic resolution required the use of a polar HILIC stationary phase with isopropyl alcohol (IPA) and water as the mobile phase. In all cases, mobile phases were buffered with 0.1% formic acid. All nine

compounds exhibited acceptable purity levels (>95%), and the molecular ion peak (M^+) was readily detected. These candidates were then sent at the University of Bayreuth for testing their inhibitory activity against SIRT6 using an enzymatic assay.

5.5 Sulfone derivatives

While awaiting the biological results necessary for the selection of fragments to be used in the design of new small molecules, during my research period at Ri.MED Foundation, I focused my efforts to the design and synthesis of new compounds aimed at reproducing the key interactions observed in the docking studies of TSN. Based on the docking results and molecular dynamics trajectory analysis, I identified specific interactions that appeared critical for the stabilization of the TSN–SIRT6 complex. In particular, the oxygen atom of the hydroxamic group was found to form hydrogen bonds with residues Val115 and Asp116, while the hydroxyl group engaged in a direct hydrogen bond with Asp116. Additionally, the nitrogen atom of the hydroxamic moiety was involved in a water-bridge mediated hydrogen bond with Ala53 and Ile61. These findings guided the rational design of novel compounds able to bind the same key residues within the SIRT6 active site. Accordingly, I designed a small library of thirty-two compounds in which two aromatic rings are connected via a sulfonic linker (Table 6). Each molecule also featured a carboxamide moiety, which, based on computational studies, was found to be crucial for establishing interactions with key amino acid residues within the binding site.

Table 6. Structures of the new designed derivatives.

Cpd.	Chemical structure	Docking score (Kcal/mol)	Cpd.	Chemical structure	Docking score (Kcal/mol)
18a	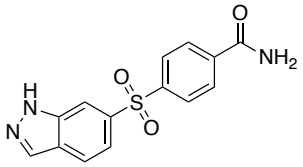	-8.030	**20a**	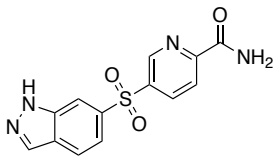	-7.247
18b	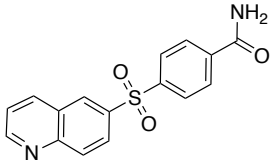	-8.559	**20b**	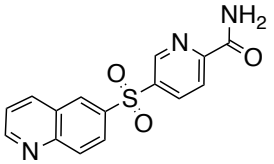	-8.589
18c	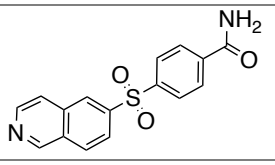	-8.244	**20c**	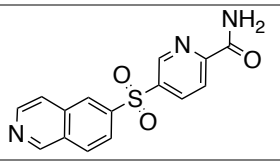	-8.082
18d	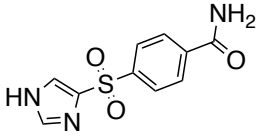	-7.669	**20d**	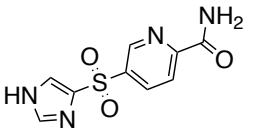	-7.247
18e	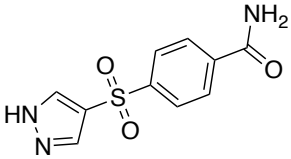	-7.669	**20e**	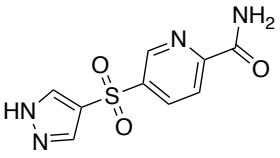	-7.247

18f	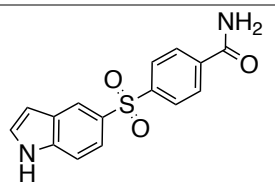	-8.160	**20f**	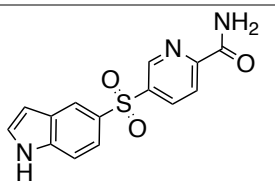	-8.132
18g	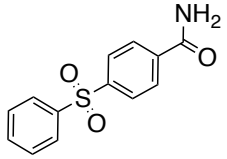	-8.230	**20g**	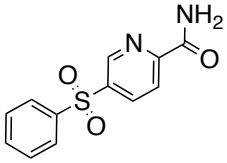	-8.044
18h	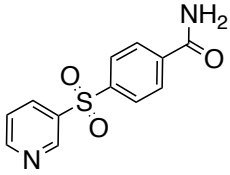	-8.082	**20h**	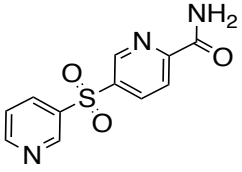	-7.916
19a	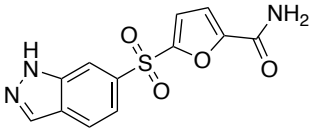	-5.712	**21a**	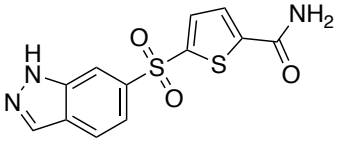	-7.876
19b	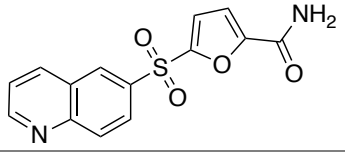	-8.038	**21b**	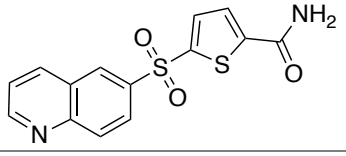	-8.266
19c	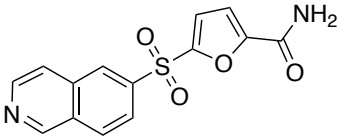	-7.936	**21c**	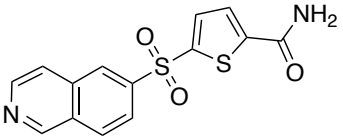	-8.227
19d	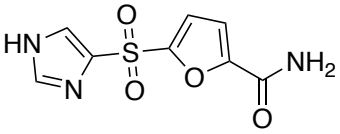	-7.266	**21d**	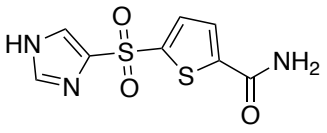	-7.469
19e	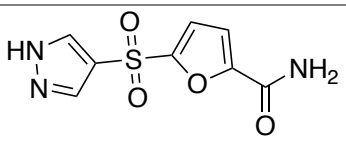	-7.266	**21e**	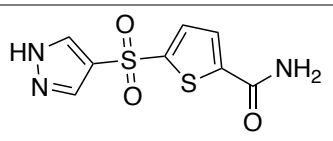	-7.469
19f	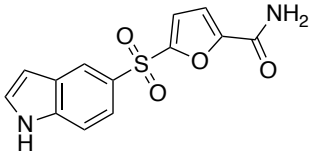	-7.877	**21f**	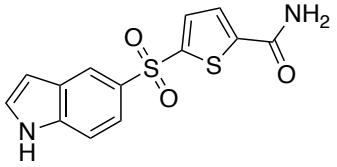	-8.063
19g	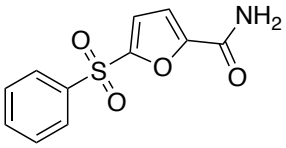	-8.317	**21g**	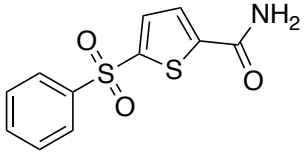	-7.924
19h	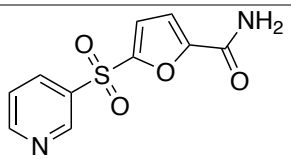	-7.470	**21h**	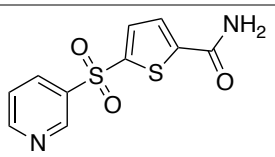	-7.346
TSN	-	-6.265	**TSN**	-	-6.265

Interestingly, in the docking poses, the aromatic ring of these compounds already displayed π–π stacking interactions with Phe64 that, in the case of TSN, was observed only through molecular dynamics simulations. This suggests that the designed structures may interact, potentially enhancing their interaction with SIRT6. The absence of commercially available heterocycles bearing a thiol group for sulfone production necessitated a more extensive exploration of alternative synthetic routes. Consequently, different synthetic strategies were attempted. Given the immediate availability of brominated heterocycles, these were considered as suitable starting materials for the synthesis of both thiols and sulfones. In particular, the synthesis of thiols was initially attempted using bromobenzene as the starting material and thiourea (CH_4N_2S, 1.5 eq) in dimethylformamide (DMF) at 140 °C for 2 hours (a). However, no product formation was observed. The reaction was subsequently repeated under reflux in absolute EtOH with the same amount of CH_4N_2S (b) and, in a third attempt, with 2.5 equivalents of CH_4N_2S were employed under the same conditions (c). A final attempt involved the use of sodium hydrogen sulphide (NaHS, 2.5 eq) in DMF at 140 °C for 2 hours (d). In all cases, the formation of thiophenol was not observed (Scheme 1).

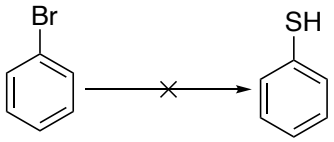

Scheme 1. **Reaction attempts to obtain the Thiophenol.** Reagents and conditions. **a.** CH_4N_2S (1.5 eq), DMF, 140 °C, 2 h; **b.** CH_4N_2S (1.5 eq), EtOH abs., reflux, 2 h; **c.** CH_4N_2S (2.5 eq), EtOH abs., reflux, 2 h; **c.** NaHS (2.5 eq), DMF, 140 °C, 2 h.

A potential synthetic route aimed at achieving a faster and more straightforward access to the desired sulfone was also investigated, involving the coupling between organolithium derivatives and sulfonyl chlorides. To this end, a solution of 6-bromoisoquinoline in tetrahydrofuran (THF) was cooled to –78 °C, and n-butyllithium (n-BuLi, 1.1 eq) was added dropwise over the course of one minute. After stirring for 30 minutes at this temperature, a solution of benzenesulfonyl chloride in THF, also precooled to –78 °C, was added to the reaction mixture containing the quinolinyl-lithium intermediate. The mixture was stirred for an additional 15 minutes, followed by gradual warming to 0 °C using an ice bath. At this point, 1 mL of a 10% aqueous solution of acetic acid was added, and stirring was continued for 5 minutes before removing the cooling bath. Despite the careful control of the reaction parameters and the inert atmosphere, the desired sulfone product was not obtained. This result suggests that either the lithiation step was inefficient under the applied conditions or the nucleophilic attack on the sulfonyl chloride did not proceed as expected (Scheme 2).

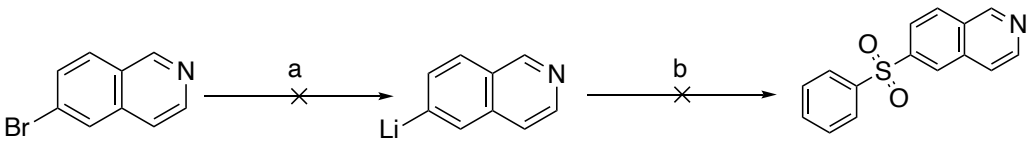

Scheme 2. **Reaction attempts to obtain the 6-(Phenylsulfonyl)isoquinoline**. Reagents and conditions. **a.** n-BuLi (1.1 eq), THF, -78 °C, 30 min. **b.** Benzenesulfonyl chloride (1 eq), THF, -78 °C to 0 °C, 15 min.

A Suzuki–Miyaura-type cross-coupling reaction was also explored, following the experimental procedure reported in the literature (Scheme 3). In the initial attempt, a mixture of pyridin-3-ylboronic acid, benzenesulfonyl chloride (1 eq), and potassium carbonate (K_2CO_3, 2 eq) in an acetone/water (3:1) solution at 0 °C was prepared, to which palladium(II) chloride ($PdCl_2$, 1.6 mol%) was added. The reaction mixture was stirred at room temperature under a nitrogen atmosphere.[105]

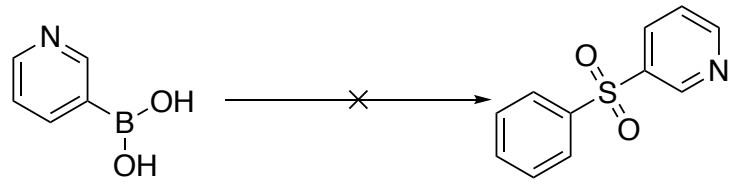

Scheme 3. **Reaction attempts to obtain the 3-(Phenylsulfonyl)pyridine** with Suzuki–Miyaura-type cross-coupling reaction. Reagents and conditions. Benzenesulfonyl chloride (1 eq), K_2CO_3 (2 eq) $PdCl_2$ (1.6 mol %), acetone:H_2O (3:1), 0 °C to r.t, 30 min.

However, the desired coupling product was not obtained. It was hypothesized that the presence of water may have led to the hydrolysis of benzenesulfonyl chloride, forming the corresponding sulfonic acid, thereby inhibiting the transmetalation step of the palladium-catalyzed reaction. To address this issue, several modified conditions were tested in an effort to suppress side reactions and improve coupling efficiency:

1. $PdCl_2$ was replaced with palladium(II) acetate, $Pd(OAc)_2$;
2. the reaction was carried out using $PdCl_2$ in 1,4-dioxane instead of the water:acetone mixture under microwave irradiations;
3. a combination of $PdCl_2$ in 1,4-dioxane and a 2 M aqueous solution of K_2CO_3 was tested, also under microwave irradiations;
4. the solvent system was modified by using acetone instead of the water:acetone mixture (3:1).

Despite the various attempts, none of the modified protocols led to the successful formation of the desired sulfone products. These observations suggest that the sulfonyl chloride moiety may not be compatible with Suzuki–Miyaura-type cross-coupling reactions under the tested

conditions, likely due to its susceptibility to hydrolysis and the limited reactivity of the functional group in the presence of the palladium catalytic system.

The only sulfone derivative that was synthesized is the 5-(phenylsulfonyl)furan-2-carboxamide (**19g**) from its commercial precursor 5-(phenylsulfonyl)furan-2-carboxylic acid (Scheme 4). Compound **19g** was selected based on its better docking score (-8.317 kcal/mol) compared to TSN (–6.164 kcal/mol), and for its ability to establish key interactions with crucial amino acid residues within the binding site (Figure 12).

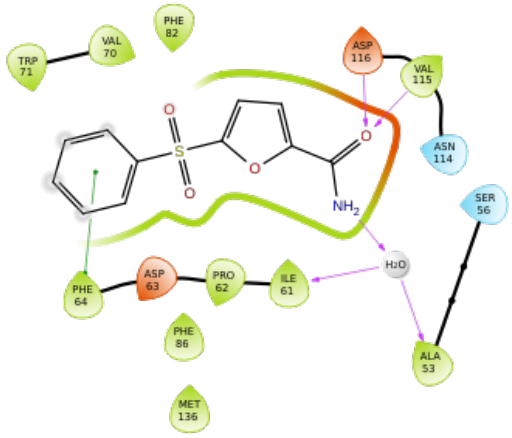

Figure 12. Ligand Interaction Diagram of the docking pose of 5-(phenylsulfonyl)furan-2-carboxamide (**19g**).

Compound **19g** was obtained through a direct amidation reaction between the 5-(phenylsulfonyl)furan-2-carboxylic acid (**22**) and ammonium chloride (NH_4Cl), employing 1-ethyl-3-(3-dimethylaminopropyl)carbodiimide hydrochloride (EDC·HCl) as a coupling agent, catalytic amounts of 1-hydroxybenzotriazole (HOBt) to reduce isomerization and suppress side reactions, and 4-dimethylaminopyridine (DMAP) as an acyl transfer reagent to facilitate the formation of a highly reactive acyliminium intermediate, as proposed by Steglich in his esterification protocol (Scheme 4).[106] After 24 hours of magnetic stirring, this protocol led to the isolation of **19g** as a single product, with a yield of 46.8%.

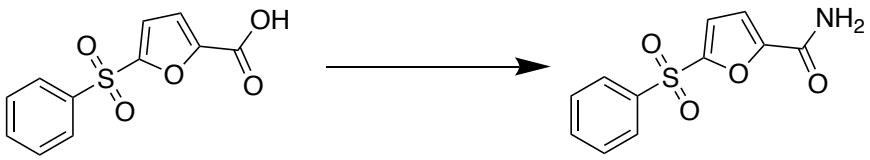

Scheme 4. Synthesis of 19g. Reagents: EDC·HCl, HOBt, DMAP, NH_4Cl, DMF. Experimental conditions mechanical stirring, r.t., 24 h. Yield: 46.8%.

The 5-(phenylsulfonyl)furan-2-carboxamide (**19g**) will be evaluated for its ability to inhibit SIRT6 deacetylase activity.

5.6 In-vitro SIRT6 inhibitory activity of the selected compounds

The selected compounds were evaluated for their ability to inhibit SIRT6 deacylation activity employing a fluorogenic assay based on the Fluor-de-Lys deacetylation substrate. Compound **12** was excluded from testing due to poor solubility. Most of the tested molecules exhibited a weak yet statistically significant inhibitory effect, supporting their classification as fragment-like structures suitable for further development in the design of novel SIRT6 inhibitors. Compounds **9** and **17** did not produce statistically relevant results, primarily due to signal variability observed at higher concentrations, which was again attributed to limited solubility. Compounds **10**, **11**, **14**, and **16** showed slightly better inhibitory profiles compared to compounds **13** and **15**, displaying significant activity already at intermediate concentrations. Notably, all compounds demonstrated a dose-dependent increase in inhibition, although none achieved full inhibition even at the highest tested concentration (50 µM) (Figure 13). Despite the relatively modest activity values in the high micromolar range, the fragment-like nature of these compounds makes them promising starting points for a structure-based drug design campaign. Accordingly, *in silico* approaches were employed to guide a fragment optimization with the goal of identifying more potent SIRT6 inhibitors.

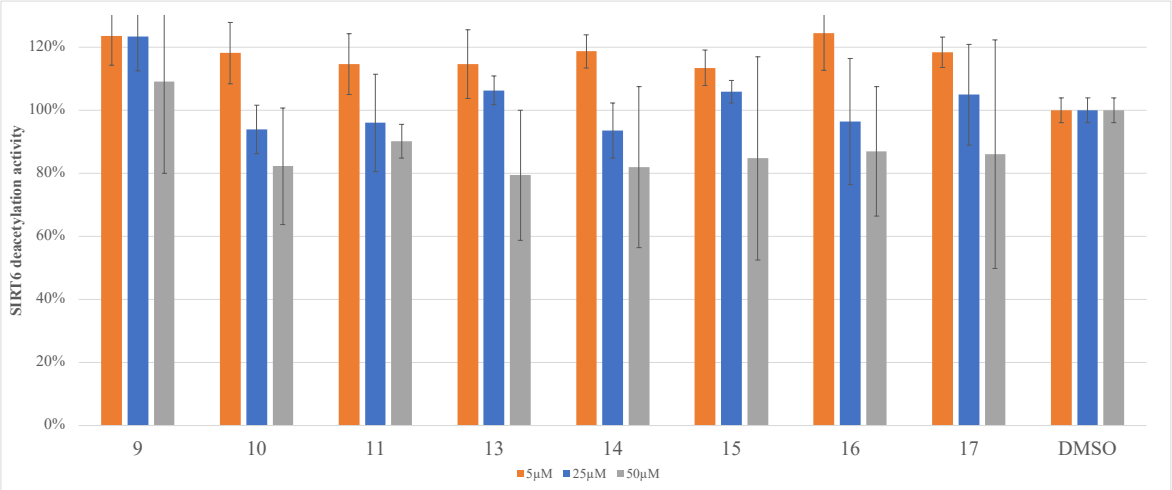

Figure 13. Inhibition rate for SIRT6 deacetylation activity.

The selection of fragments to be used for the design of new SIRT6 inhibitors was based on the integration of biological assay results with an extensive review of the scientific literature. This analysis highlighted that the few known synthetic SIRT6 inhibitors are small molecules, typically exhibiting molecular weights between 160 and 370 Da. Consequently, the compounds with molecular weights of 238, 269, and 270 Da were excluded from further

consideration, as their structures were not suitable for molecular elaboration. Among the five remaining compounds, with molecular weights ranging from 142 to 180 Da, **13**, **14**, and **17** were selected (Table 5). These fragments represent promising starting points for the rational design of novel SIRT6-targeting molecules.

5.7 Design of new potential SIRT6 inhibitors

The fragment growth process involved the expansion of three selected fragments (**13**, **14**, and **17**) through conjugation to an aromatic ring, with the aim of improving their drug-like properties. A key aspect of the design strategy was the identification of an optimal linker between the two aromatic moieties. Among the various linkers tested, computational analyses revealed that molecules bearing a ketone or ester linker consistently exhibited an inverted docking pose within the SIRT6 binding pocket. This inversion impaired the ability of the terminal carboxylic acid, carboxamide or sulphonamide group to establish interactions with key amino acid residues in the active site. This behavior could be attributed to the increased rigidity of the ketone linker and to the suboptimal geometry imposed by the ester group. In contrast, significant improvements were observed with the use of an amide linker. In this case, all the designed molecules were able to insert deeply into the binding pocket, adopting binding poses that overlapped with that of TSN, and, in most cases, exhibited improved docking scores. Moreover, structural modifications at the meta-position of the terminal aromatic ring were also evaluated, replacing the carboxamide group with either a carboxylic acid or a sulphonamide group, in order to investigate the impact of distinct electronic and steric properties on binding affinity. However, at the physiological pH range considered, the carboxylic acid was deprotonated, thus preventing the hydroxyl group from forming H-bonds, thereby resulting in reduced. Similarly, the substitution with a sulphonamide on the terminal ring introduced steric bulk and conformational flexibility due to the tetrahedral geometry around the sulfur atom. This probably hindered optimal binding site positioning and reduced the chances of forming H-bonds, as confirmed by docking analyses, which revealed lower scores and less favourable binding orientations than carboxamide analogues. These findings consistently highlighted the meta-positioned carboxamide as the most effective functional group in terms of binding orientation and interaction with key residues within the SIRT6 active site. In particular, among the compounds featuring a central amide linker, only those functionalized with a meta-substituted carboxamide on the terminal aromatic ring were able to establish favourable and stable interactions within the binding pocket. Based on these results, the meta-substituted carboxamides emerged as the most promising candidates, and the synthesis efforts were therefore focused on this subset of fifteen derivatives (Figure 14), which showed the highest binding affinity and optimal structural complementarity (Table 7).

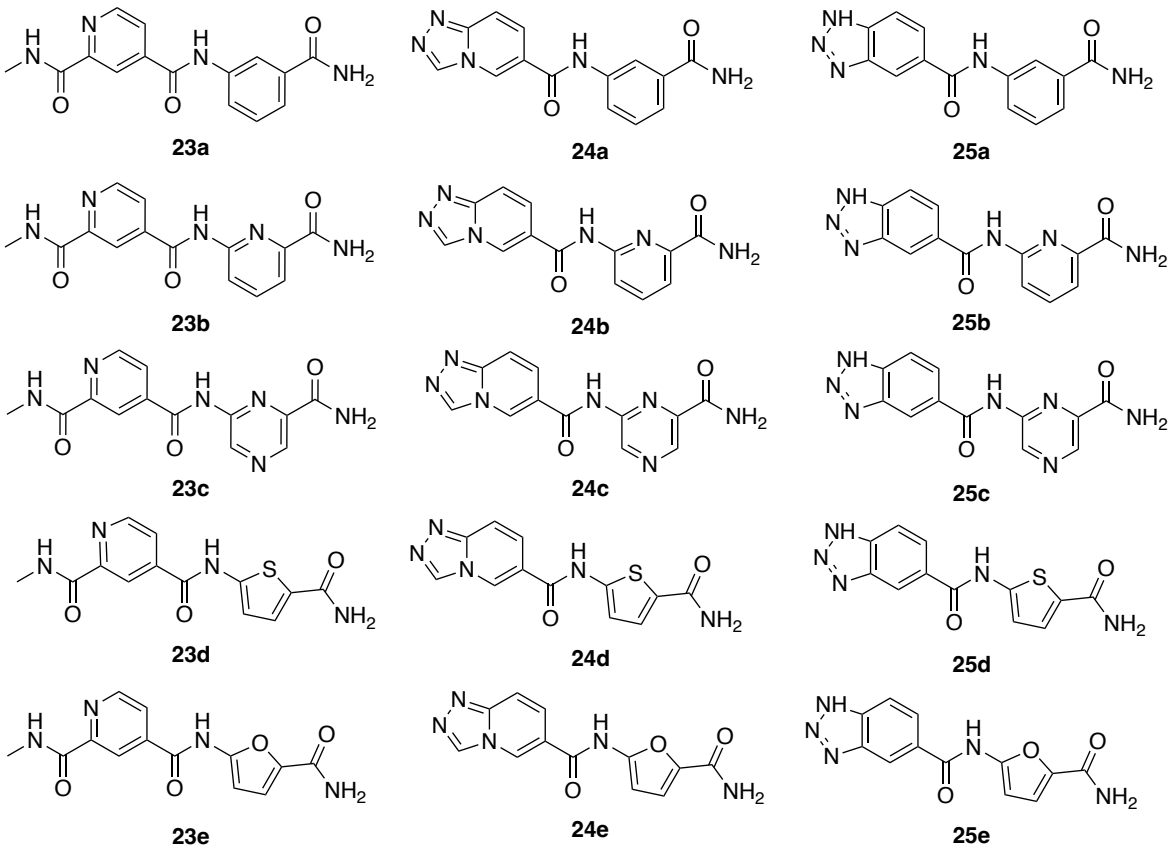

Figure 14. Structures of the most promising compounds

Table 7. Docking scores of the selected carboxamide.

Cpd.	Docking score (kcal/mol)	Cpd.	Docking score (kcal/mol)	Cpd.	Docking score (kcal/mol)
23a	-6.162	**24a**	-6.693	**25a**	-6.824
23b	-6.563	**24b**	-6.826	**25b**	-5.586
23c	-6.630	**24c**	-6.566	**25c**	-7.450
23d	-7.813	**24d**	-6.585	**25d**	-7.223
23e	-7.336	**24e**	-5.139	**25e**	-7.130
TSN	-6.265	**TSN**	-6.265	**TSN**	-6.265

5.8 Carboxamides synthesis

The retrosynthetic analyses of the newly designed carboxamides (**23a-e**, **24a-e**, **25a-e**) involved the cleavage of the amide linker, leading to the corresponding synthetic equivalents: compounds **13**, **14** and **17** as carboxylic acids, and the aromatic primary amines **26a–c** and **27a-b** (Scheme 5).

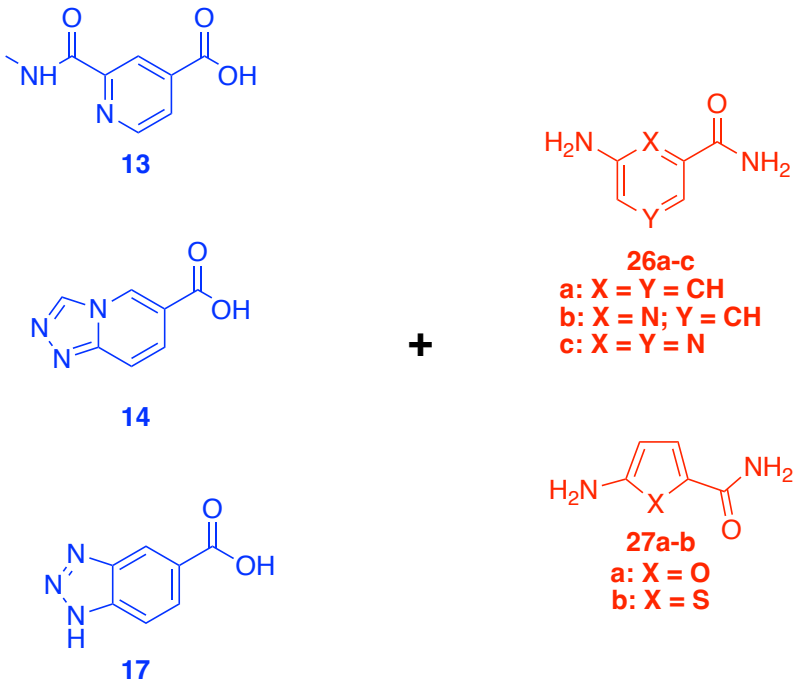

Scheme 5. Retrosynthetic analysis of the new carboxamides.

The synthesis of the carboxylic acids required different synthetic approaches. Compound **13** was synthesized via the initial direct condensation of 4-(methoxycarbonyl)pyridine-2-carboxylic acid (**28**) with methylamine hydrochloride ($CH_3NH_2 \cdot HCl$), employing the EDC/HOBt/DMAP reagent system. This intermediate undergoes nucleophilic attack by the primary amine to afford the coupling product methyl 2-(methylcarbamoyl)isonicotinate (**29**). The coupling reaction was carried out using either conventional method or microwave-assisted organic synthesis (MAOS). In the conventional approach, the reaction mixture was stirred at room temperature for 24 hours. After standard work-up and chromatographic purification on a traditional flash silica gel column, the intermediate **29** was isolated in 68.3% yield. By applying MAOS technique, **29** was obtained in only 40 minutes (2 cycles of 20 minutes each) using microwave irradiation at 150 W and 80 °C. Final purification was performed by medium-pressure liquid chromatography (MPLC) using an automated chromatographic system, affording the product in an improved yield of 83.0%. Subsequently, **29** underwent an alkaline hydrolysis of the ester group using a 1M

KOH/MeOH hydroalcoholic solution to obtain **13** (Scheme 6). The hydrolysis was also performed under both conventional and microwave-assisted conditions. In the conventional procedure, the potassium salt of **13** was obtained after 1 hour under reflux. Acidification with 3 M HCl to pH 4–5 allowed the isolation of **13**, which was subsequently purified by conventional column chromatography, affording the product in 37.4% yield. Using the MAOS approach, ester hydrolysis was completed in only 4 minutes under microwave irradiation at 200 W and 120 °C. Final acidification with 3 M HCl to pH 4–5 yielded **13** as a pure solid, with a significantly improved yield of 85.0%.

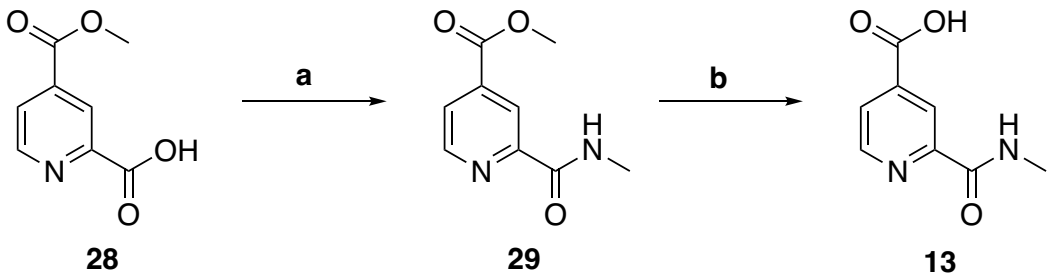

Scheme 6. Synthesis of 13. Reagents: **a.** EDC·HCl, HOBt, DMAP, CH_3NH_2·HCl. Solvent: anhydrous DMF. Experimental conditions: 1) mechanical stirring, r.t., 24 h. Yield: 68.3%. 2) MW, T = 80 °C, 150 W, 2 cycles of 20 minutes each. Yield: 83.0%. **b.** KOH/MeOH; work-up: 3M HCl to pH = 4–5. Experimental conditions: 1) reflux, 1 h. Yield: 37.4%. 2) MW, T = 120 °C, 200 W, 4 min. Yield: 85.0%.

Carboxylic acid **14** was synthesized via the reaction of 6-hydrazinylpyridine-3-carboxylic acid (**30**) with formic acid, initially forming a hydrazone intermediate. Under acidic conditions, protonation of the carbonyl oxygen of the aldehyde moiety increased its electrophilicity, thereby facilitating subsequent condensation with the pyridinic nitrogen and cyclization into a five-membered ring (Scheme 7). Compound **14** was obtained under conventional reflux conditions after 16 hours, affording a yield of 80.6%. Alternatively, the reaction was performed using microwave-assisted heating, reaching completion in just 20 minutes at 100 °C and 150 W, with an improved yield of 95.4%.

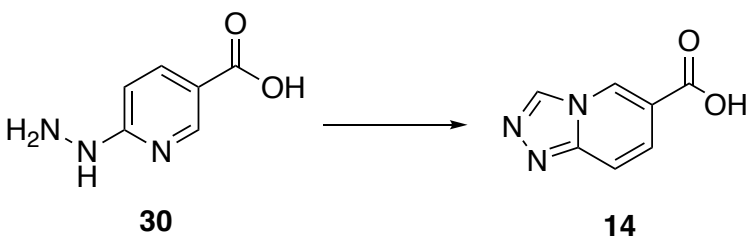

Scheme 7. Synthesis of 14. Reagents: HCOOH. Experimental conditions: 1) reflux, 16 h. Yield: 80.6%. 2) MW, T = 100 °C, 150 W, 20 min. Yield: 95.4%.

Carboxylic acid **17** was synthesized via diazotization of 3,4-diaminobenzoic acid (**31**) using 1.1 equivalents of $NaNO_2$ in glacial acetic acid at 0 °C. The resulting diazonium intermediate underwent an intramolecular nucleophilic attack by the adjacent amino group, leading to the formation of the triazole ring. Compound **17** was isolated as a pure solid in 93.2% yield (Scheme 8).

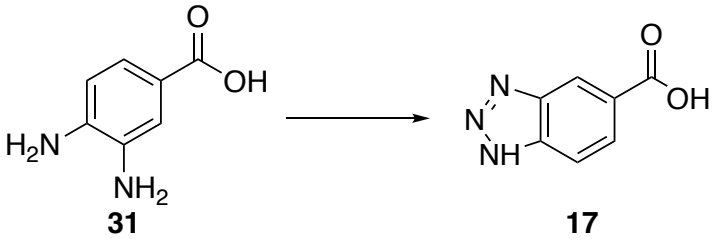

Scheme 8. Synthesis of 17. Reagents: $NaNO_2$ (1.1 eq.), glacial AcOH. Experimental conditions: T = 0 °C, 1 h; then r.t. overnight. Yield: 93.2%.

The aromatic primary amines **26a–c**, essential for the final condensation step with the proper fragment, were efficiently synthesized via direct condensation of the corresponding carboxylic acids (**32a–c**) with NH_4Cl, employing the EDC/HOBt/DMAP reagent system, as shown in Scheme 9. Specifically, 3-aminobenzamide (**26a**) was obtained from 3-aminobenzoic acid (**32a**), 6-aminopyridine-2-carboxamide (**26b**) from 6-aminopyridine-2-carboxylic acid (**32b**), and 6-aminopyrazine-2-carboxamide (**26c**) from 6-aminopyrazine-2-carboxylic acid (**32c**). The coupling reactions were conducted under both conventional and microwave-assisted conditions. In the conventional method, the reaction mixtures were stirred at room temperature for 24 hours. Under microwave irradiation, compounds **26a–c** were obtained in just 40 minutes (2 cycles of 20 minutes each) using a power of 150 W and a temperature of 80 °C. For purification, solid-phase extraction (SPE) cartridges packed with silica gel as sorbent were employed.

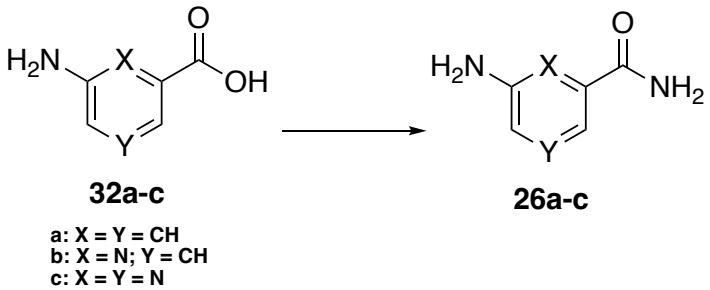

Scheme 9. Synthesis of 26a-c. Reagents: EDC·HCl, HOBt, DMAP, NH_4Cl. Solvent: anhydrous DMF. Experimental conditions: 1) mechanical stirring, r.t., 24 h. Yield: 86.7–90.4%. 2) MW, T = 80 °C, 150 W, 40 min. Yield: 44.0–97.8%

The synthesis of aromatic amines **27a–b** is still in progress, as the attempts made employing reducing agents such as iron (Fe), tin(II) chloride ($SnCl_2$), or ammonium formate ($HCOONH_4$) in the presence of palladium on activated carbon (Pd-C) have not led to the formation of the desired primary amines, probably due to their high instability intermediates. However, the corresponding amides **33a–b** were successfully synthesized via direct condensation of carboxylic acids **34a–b** with NH_4Cl, using the EDC/HOBt/DMAP reagent system. The coupling reactions were conducted under both conventional and microwave-assisted conditions. In the conventional method, the reaction mixtures were stirred at room temperature for 24 hours (yield = 75.2 and 77.9%, respectively). Under microwave irradiation, **33a–b** were obtained in only 40 minutes (2 cycles of 20 minutes each) using a power of 150 W and a temperature of 80 °C (both with 80.1% yield), as shown in Scheme 10. For the purification, SPE cartridges packed with silica gel as sorbent were also employed in this case. Table 8 shows a comparison of reaction conditions between the conventional method and MW.

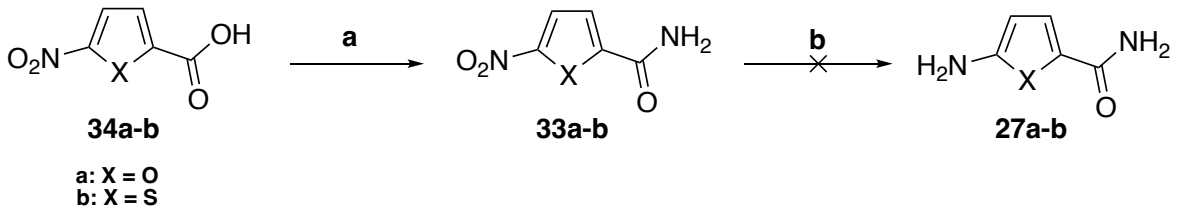

Scheme 10. Synthesis of 33a-b. a. Reagents: EDC·HCl, HOBt, DMAP, NH_4Cl. Solvent: anhydrous DMF. Experimental conditions: 1) mechanical stirring, r.t., 24 h. Yield: 75.2–77.9%. 2) MW, T = 80 °C, 150 W, 40 min. Yield: 80.1–88.5%. **b.** 1) Reagents: $HCOONH_4$ (4 eq), Pd-C (5% w/w) Solvent: EtOH Experimental conditions: r.t., o.n.; 2) Reagents: Fe (3 eq), Solvent: AcOH, Experimental conditions: 80 °C, 2.5 h; 3) Reagents: Fe (5 eq), Solvent: AcOH, Experimental conditions: 80 °C, 6 h; 4) Reagents: $SnCl_2$ (3.5 eq), Solvent: HCl conc. Experimental conditions: r.t., 24 h; 5) Reagents: $SnCl_2$ (4 eq), Solvent: HCl conc. Experimental conditions: r.t., 48 h.

Table 8. Comparison of experimental reaction conditions.

	Conventional method		**MW**	
Cpd	**Reaction Time**	**Yield (%)**	**Reaction Time**	**Yield (%)**
13	1 h	37.4	4 min	85.0
14	16 h	80.6	20 min	95.4
26a	24 h	90.0	40 min	97.8

26b	24 h	86.7	40 min	68.0
26c	24 h	90.4	40 min	44.0
29	24 h	68.3	40 min	83.0
33a	24 h	75.2	40 min	80.1
33b	24 h	77.9	40 min	80.1

The amide coupling reactions to obtain the final products required extensive optimization. This was due to the low nucleophilicity of the nitrogen lone pair in aromatic amines **26a–c**, which is significantly reduced by the presence of electron-withdrawing groups on the aromatic ring (e.g., –$CONH_2$), and by the additional nitrogen atoms in the case of heteroaromatic amines **26b** and **26c**. Considering the amide coupling reactions previously employed for the synthesis of compounds **13** and **26a–c**, the initial synthetic approach for obtaining the final amides involved applying the same experimental protocol (EDC/HOBt, DMAP). The test reaction was carried out using carboxylic acid **17** and amine **26a**. Under conventional conditions (24 hours, magnetic stirring, room temperature), the desired product N-(3-carbamoylphenyl)-1H-1,2,3-benzotriazole-5-carboxamide (**25a**) was obtained with a yield of 8.2%. When the same reaction was conducted under microwave-assisted conditions (T = 80 °C, P = 150 W, 2 cycles of 20 minutes), the yield increased modestly to 12.7% (Scheme 11).

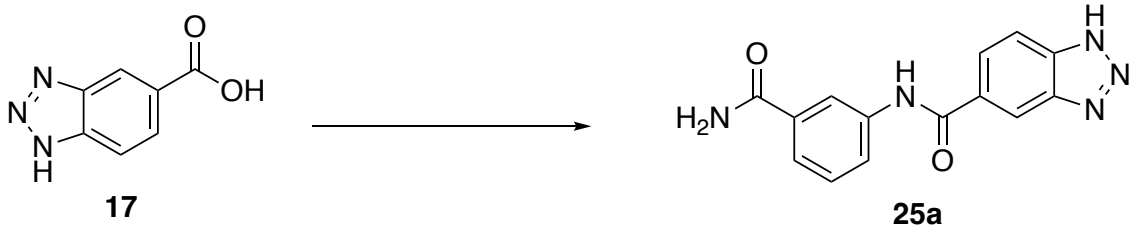

Scheme 11. Synthesis of 25a. Reagents: EDC·HCl, HOBt, DMAP, **26a**. Solvent: anhydrous DMF. Experimental conditions: 1) mechanical stirring, r.t., 24 h. Yield: 8.2%. 2) MW, T = 80 °C, 150 W, 40 min. Yield: 12.7%

In an effort to improve the reaction yield, during my research period abroad at the University of Hamburg, I had the opportunity to explore alternative synthetic methodologies. Among these, particular attention was given to a protocol involving the direct coupling of sterically hindered carboxylic acids with poorly nucleophilic amines using N,N,N′,N′-

tetramethylchloroformamidinium hexafluorophosphate (TCFH) as the coupling agent and N-methylimidazole (NMI) as the base.[107] This method promotes the *in situ* formation of highly reactive N-acylimidazolium intermediates, which facilitate amide bond formation under mild conditions (Figure 15).

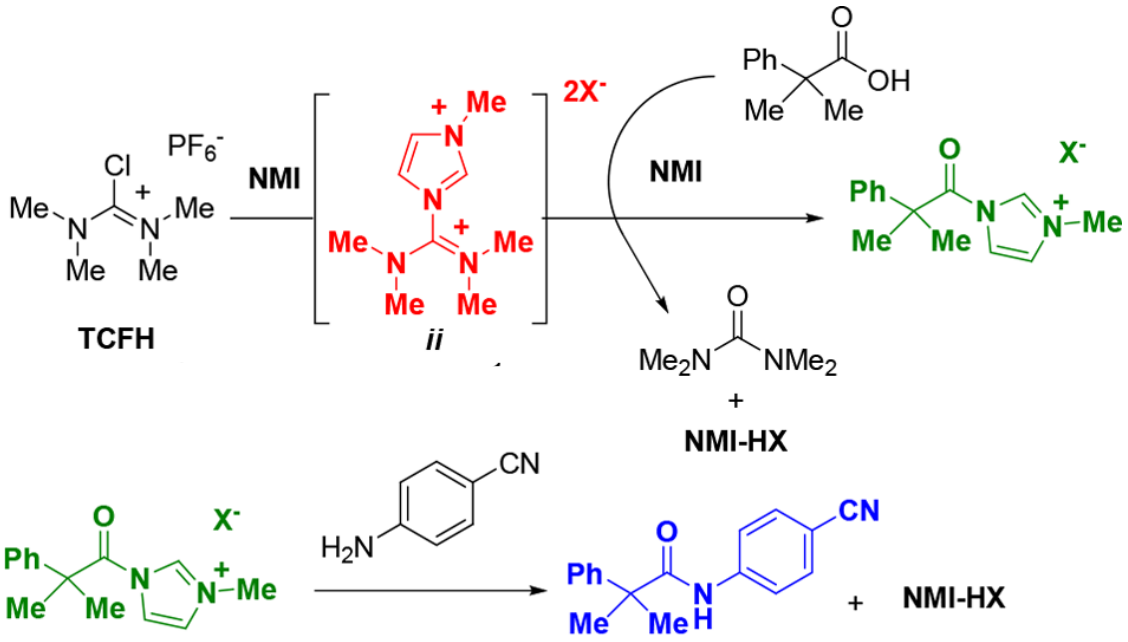

Figure 15. Proposed mechanism of amide bond formation promoted by TCFH/NMI coupling system.

I paid particular attention to the choice of solvent and reaction time, as both parameters were reported to significantly influence the formation of an anhydride as a side product. According to the literature, the use of acetonitrile as solvent and a reaction time of 3 hours resulted in the highest conversion to the desired amide. However, due to the poor solubility of my carboxylic acids in acetonitrile, I carried out the reaction in anhydrous DMF, maintaining the same stoichiometric ratios and reaction time as reported in the original study. Under these conditions, the coupling between **17** and amine **26a** at room temperature afforded the desired amide **25a** in a yield of 9.4%. I then performed the same reaction under microwave-assisted heating, applying the protocol previously optimized for the synthesis of amides **26a–c** (T = 80 °C, P = 150 W, 2 cycles of 20 minutes each). Under these conditions, I obtained amide **25a** with a yield of 33.0%. By increasing the number of cycles to 4 (20 minutes each), for a total reaction time of 80 minutes, the yield improved to 45.0% (Table 9).

Table 9. Comparison of experimental conditions for the synthesis of N-(3-carbamoylphenyl)-1H-1,2,3-benzotriazole-5-carboxamide **25a**.

		Conventional method		MW				
Coupling system	**Solvent**	**Reaction time**	**Yield (%)**	**T (°C)**	**P (W)**	**T (min.)**	**Cycles**	**Yield (%)**
EDC/HOBt, DMAP	DMF	24 h	8.2	80	150	20	2	12.7
TCFH/NMI	DMF	3 h	9.4	80	150	20	2	33
TCFH/NMI	DMF	-	-	80	150	20	4	45

This final experimental protocol was employed for the synthesis of the amides **23a,b**, **24a**, **25a,c** that will be tested for their inhibitory activity on SIRT6, as detailed in Table 10.

Table 10. Yield of final amides obtained using the MW protocol and TCFH/NMI reagent system.

FRAGMENT	AMINE	AMIDE	YIELD (%)
13	**26a**	**23a**	30.2
13	**26b**	**23b**	20.5
13	**26c**	**23c**	N.E.
14	**26a**	**24a**	25.0
14	**26b**	**24b**	N.E.
14	**26c**	**24c**	N.E.
17	**26a**	**25a**	45.0
17	**26b**	**25b**	N.E.
17	**26c**	**25c**	32.0

N.E.: Reaction not yet executed.

5.9 Exploring alternative scaffolds targeting SIRT6

With the aim to further investigate any possible alternative scaffolds targeting SIRT6, I decided to deeper evaluate compounds obtained from VS campaigns. Among them, I identified a quinoline moiety from the in-house library that, according to the scientific literature, it is known to exhibit antiproliferative activity against lymphoma cell lines and to induce apoptosis.[108,109] Then, the (*E*)-*N*-(4-nitro-3-(trifluoromethyl)phenyl)-2-styryl quinoline-4-carboxamide (**35a**) emerged from VS campaign (Figure 16) was synthesized to be tested on DLBCL cell lines.

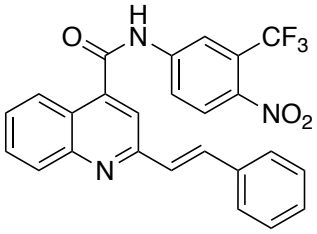

35a

Figure 16. Chemical structure of (E)-N-(4-nitro-3-(trifluoromethyl)phenyl)-2-styrylquinoline-4-carboxamide (**35a**).

For this purpose, a retrosynthetic analysis was performed thus leading to the selection of isatin (**36**) as the key starting material for the proposed synthetic route (Scheme 12).

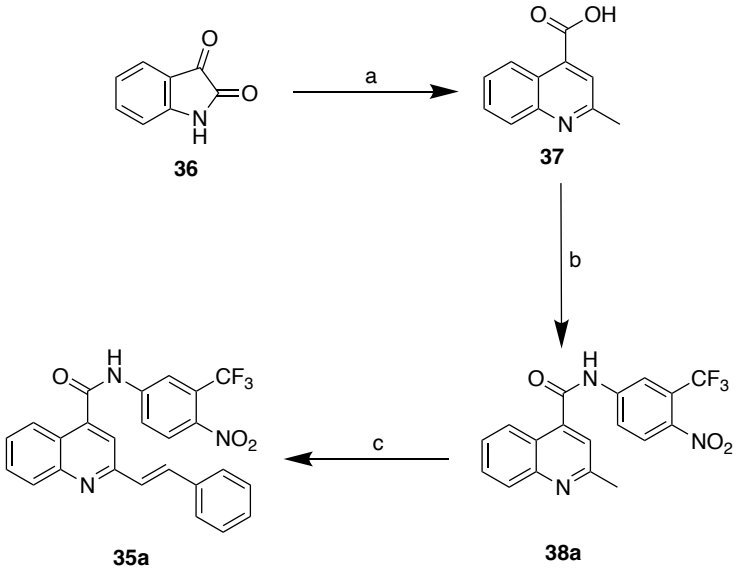

36 **37** **35a** **38a**

Scheme 12. Reagents and conditions. **a:** 1. KOH (10% aq.), $(CH_3)_2CO$; MW: 150°C, 15', 100 W (2 cycles); 2. HCl 37%, pH < 6.5; **b:** 1. EDC·HCl (2 eq), HOBt (0.2 eq), DMAP (2 eq), ACN ax; 2. 4-nitro-3-(trifluoromethyl)aniline (1 eq); MW: 50°C, 20', 60 W (2 cycles); **c:** Benzaldehyde (1 eq), glacial AcOH; MW: 150°C, 20', 200 W (2 cycles).

Compound **36** served as the starting material for the synthesis of 2-methylquinoline-4-carboxylic acid (**37**), following a procedure reported in the literature. The compound was obtained via a Pfitzinger reaction between compound **36** and acetone under alkaline conditions. After 7 hours of reflux, the target product was isolated in a yield of 48.3%.[110] The reaction was carried out using MAOS technique and under closed-vessel conditions, allowing the solvent to reach boiling points higher than those possible at atmospheric pressure. The first synthetic step was performed by setting the microwave reactor power at 100 W and maintaining a constant temperature of 150 °C for 15 minutes. A second microwave cycle under the same conditions was performed to complete the reaction. This microwave protocol led to the isolation of compound **37** as a single product, with an excellent yield of 92.7%. For comparative purposes, the same reaction was carried out under conventional heating, leading to the synthesis of **37** with a yield of only 48.3%.

The second step was a coupling reaction between **37** and 4-nitro-3-(trifluoromethyl)aniline to obtain the 2-methyl-N-(4-nitro-3-(trifluoromethyl)phenyl)quinoline-4-carboxamide (**38a**). In the literature, this type of reaction typically involves the formation of an activated intermediate of the carboxylic acid via chlorination with thionyl chloride, under prolonged reflux conditions (3-8 hours), followed by an amidation reaction with the proper substituted aniline pyridine or triethylamine in dichloromethane at room temperature for 24-48 hours, yielding the desired carboxamide with reported yields of 20-30%.[111] Therefore, a direct amidation strategy was employed using the well-established EDC/HOBt/DMAP reagent system. The reaction was initially performed at room temperature under magnetic stirring for 24 hours. However, under these conditions, the target compound **38a**, was isolated with a yield of less than 5%. The reaction was carried out under microwave irradiation by setting the reactor to a power of 60 W and maintaining a constant temperature of 50 °C for 20 minutes. A second cycle under the same conditions was performed to complete the reaction. This protocol led to the isolation of **38a** with a yield of 45.2%.

The final step of the synthesis involved the reaction between the substituted carboxamides and an aldehyde under acidic conditions to form an α,β-unsaturated bond. Indeed, the imine–enamine tautomerism of compound **37** enables a nucleophilic attack on the formyl group, leading to the formation of the 2-styrylbenzene moiety. The reaction was initially carried out under conventional heating by refluxing the mixture in glacial acetic acid. After 62 hours of reflux, the reaction was quenched by addition of water, and the resulting precipitate was collected by vacuum filtration to afford compound **35a** with a yield of 33.7 %. In order to

obtain **35a** in a short time, microwave-assisted heating was also applied to the final reaction step. The optimisation of the protocol involved several attempts to evaluate the parameters of power, time, and temperature. The best yield was achieved by setting the reactor to a power of 200 W and maintaining a constant temperature of 150 °C for 20 minutes. A second cycle under the same conditions was performed to complete the reaction. The optimised reaction conditions were set as follows: 2-methyl-N-(4-nitro-3-(trifluoromethyl)phenyl) quinoline-4-carboxamide (1 eq) in 0.5 mL of glacial AcOH, PhCHO (1 eq); MW: 150 °C, 20 min, 200 W (2 cycles). **35a** was obtained with a yield of 56.8%.

Compound **35a** was tested on a panel of five cancer cell lines to evaluate its antiproliferative activity. The compound was found to be inactive against RPMI-8402 (T-lymphoblastic leukemia), A549 (NSCLC), and MDA-MB-231 (Triple-negative breast cancer). In contrast, it showed moderate to significant antiproliferative activity on HD-MB03, a medulloblastoma cell line, and SU-DHL-8, a DLBCL cell line expressing SIRT6, with IC_{50} values of 8.23 ± 0.47 µM and 3.86 ± 0.44 µM, respectively. Given these promising results, I further investigated **35a** through computational studies by analysing its binding mode using a MD simulation. Trajectory analysis revealed that the key stabilizing interactions were predominantly hydrophobic, particularly π–π stacking interactions, involving the quinoline ring and aromatic residues Phe64, Trp71, and Phe82, thereby contributing to the stabilization of the binding pose within the active site pocket. Additional persistent interactions were observed between the benzene ring and residues Phe84 and Phe86 (Figure 17).

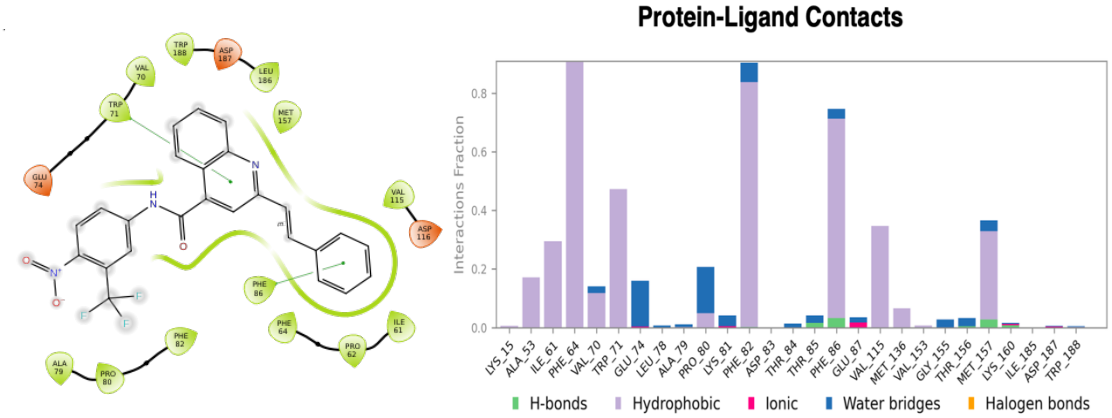

Figure 17. Ligand Interaction Diagram of the docking pose of **35a** (on the left) and Protein-Ligand contacts diagram of the MD simulation (on the right).

Given the stability of the binding pose throughout the simulation, I proceeded to design a library of thirty-three quinoline analogues (Scheme 13, Table 11), which were synthesized using the experimental protocol optimized for **35a**, resulting in final compounds with yields ranging from 56.2% to 91.1%. For reactions involving 3,4,5-trimethoxybenzaldehyde, an excess of aldehyde was necessary to drive the reaction toward completion and to enhance overall yields.

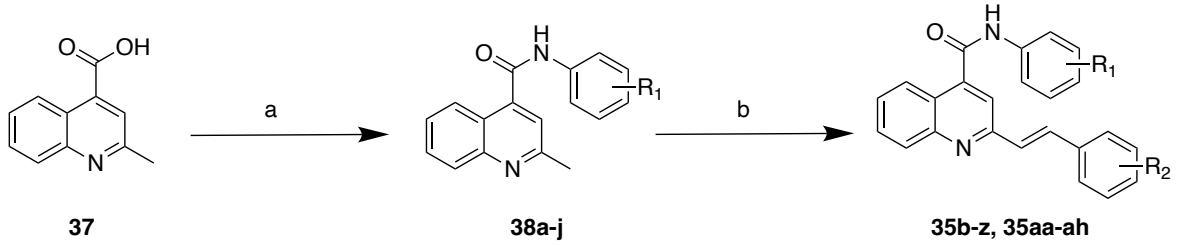

Scheme 13. Reagents and conditions. **a:** 1. EDC·HCl (2 eq), HOBt (0.2 eq), DMAP (2 eq), ACN ax; proper aniline (1 eq); MW: 50°C, 20', 60 W (2 cycles); **b:** Proper benzaldehyde (1 eq) or 3,4,5-trimethoxybenzaldehyde (2 eq), glacial AcOH; MW: 150°C, 20', 200 W (2 cycles).

Table 11. Structures of the new designed derivatives.

Cpd.	R_1	R_2	Cpd.	R_1	R_2
35b	H	H	**35s**	2,6-$(CH_3)_2$	3,4,5-$(OCH_3)_3$
35c	4-CH_3	H	**35t**	3-Cl	3,4,5-$(OCH_3)_3$
35d	4-Cl	H	**35u**	3-CF_3,4-NO_2	4-Cl
35e	3,4,5-$(OCH_3)_3$	H	**35v**	3-CF_3,4-NO_2	3,4-Cl_2
35f	4-CF_3	H	**35w**	3-CF_3,4-NO_2	4-OCH_3
35g	4-NO_2	H	**35x**	3-CF_3,4-NO_2	3-CH_3
35h	3-CH_3	H	**35y**	4-CF_3	4-Cl
35i	2,6-$(CH_3)_2$	H	**35z**	4-CF_3	4-Br
35j	3-Cl	H	**35aa**	4-CF_3	3,4-Cl_2
35k	3-CF_3,4-NO_2	3,4,5-$(OCH_3)_3$	**35ab**	4-CF_3	2-NO_2
35l	H	3,4,5-$(OCH_3)_3$	**35ac**	4-CF_3	3-NO_2
35m	4-CH_3	3,4,5-$(OCH_3)_3$	**35ad**	4-CF_3	3-CH_3
35n	4-Cl	3,4,5-$(OCH_3)_3$	**35ae**	4-Cl	4-Cl
35o	3,4,5-$(OCH_3)_3$	3,4,5-$(OCH_3)_3$	**35af**	4-Cl	3,4-Cl_2
35p	4-CF_3	3,4,5-$(OCH_3)_3$	**35ag**	4-Cl	2-NO_2
35q	4-NO_2	3,4,5-$(OCH_3)_3$	**35ah**	4-Cl	4-OCH_3
35r	3-CH_3	3,4,5-$(OCH_3)_3$	-	-	-

5.10 Antiproliferative activity of quinoline derivatives 35a-z, 35aa-ah

All synthesized quinolines (**35a-z**, **35aa-ah**) were evaluated *in vitro* on a panel of five cancer cell lines (HD-MB03, Medulloblastoma; RPMI-8402, T-lymphoblastic leukemia; SU-DHL-8, Diffuse Large B Cell Lymphoma; A549, Non-Small-Cell Lung Cancer; MDA-MB-231, Triple-negative breast cancer) to assess their antiproliferative activity. The assays were carried out at the University of Padua.

The quinolines reported interesting selectivity towards the lymphoma cell line expressing SIRT6 (SU-DHL-8), suggesting that SIRT6 could be the molecular target, as supported by computational studies (Table 12).

Table 12. *In Vitro* cell growth inhibitory effects of compounds **35a-z**, **35aa-ah**.

Cpd.	HD-MB03	RPMI-8402	SU-DHL-8	A549	MDA-MB-231
35a	8.23±0.47	>10	**3.86±0.44**	>10	>10
35b	>10	>10	>10	>10	>10
35c	>10	>10	>10	>10	>10
35d	>10	6.3±0.36	7.8±1.30	>10	>10
35e	7.1±1.15	>10	6.61±0.76	>10	>10
35f	>10	8.97±0.75	7.09±0.25	>10	>10
35g	>10	1.14±0.12	**1.64±0.25**	>10	>10
35h	>10	>10	5.05±0.58	>10	>10
35i	>10	>10	6.53±1.49	>10	5.6±0.79
35j	>10	>10	8.27±0.70	>10	>10
35k	>10	>10	>10	>10	>10
35l	>10	>10	5.33±0.52	>10	>10
35m	>10	>10	>10	>10	>10
35n	>10	>10	4.6±0.84	>10	>10
35o	>10	4.55±0.42	**2.09±0.14**	>10	5.95±0.89
35p	>10	>10	**2.13±0.08**	>10	>10
35q	>10	>10	**1.37±0.14**	>10	>10
35r	>10	3.75±0.18	**2.94±0.08**	9.34±0.18	5.95±0.66
35s	>10	0.79±0.07	**0.46±0.05**	>10	>10
35t	8.31±0.64	9.06±0.59	4.46±0.37	>10	5.7±0.10

35u	>10	3.56±0.44	8.25±0.67	>10	>10
35v	>10	>10	>10	>10	>10
35w	>10	>10	>10	>10	>10
35x	>10	>10	>10	>10	>10
35y	6.73±1.10	>10	4.77±0.30	>10	>10
35z	>10	>10	>10	>10	>10
35aa	7.83±0.98	>10	6.54±0.44	>10	>10
35ab	>10	>10	>10	>10	>10
35ac	>10	>10	>10	>10	>10
35ad	3.84±0.22	3.2±0.19	**3.25±0.23**	8.73±0.74	7.84±0.65
35ae	>10	4.61±0.24	4.45±0.53	>10	>10
35af	6.93±0.06	6.42±0.43	**3.49±0.11**	7.71±0.56	5.52±0.22
35ag	>10	1.33±0.02	**2.15±0.45**	6.92±0.68	4.99±0.35
35ah	>10	6.41±1.16	4.67±0.14	>10	>10

Data are expressed as the mean ± SE from the dose–response curves of three independent experiments.

Subsequently, the antiproliferative activity of the most promising quinolines (**35g**, **35q**, **35s**, and **35ag**) was assessed on a panel of five lymphoma-derived cell lines (VL51, Splenic B-cell lymphoma; TOLEDO, Diffuse Large B Cell Lymphoma; SU-DHL-18, Lymph node lymphoma; SU-DHL-1, Histiocytic large cell lymphoma; KM-H2, Hodgkin lymphoma) (Table 13).

Table 13. Cytotoxic activity of the most promising quinoline derivatives on lymphoma cell lines.

Cpd.	VL51	TOLEDO	SU-DHL-18	SU-DHL-1	KM-H2
35g	1.033±0.02	1.046±0.09	7.6±2.8	2.32±1.46	2.8±0.21
35q	>10	>10	>10	>10	>10
35s	>10	>10	>10	>10	>10
35ag	>10	4.93±0.62	3.79±0.51	4.9±0.31	6.74±2.12

Data are expressed as the mean ± SE from the dose–response curves of three independent experiments.

The results showed that the most active compounds were **35g**, which exhibited potent activity across all tested lymphoma lines with IC_{50} values ranging from 1.033 to 7.6 µM, and

35ag, which displayed slightly lower activity ($3.79 \leq IC_{50} \leq 6.74$ μM) on TOLEDO, SU-DHL-18, SU-DHL-1, and KM-H2, but was inactive against VL51 ($IC_{50} > 10$ μM). Both compounds feature small electron-withdrawing substituents on their phenyl groups. Although a substituent-based analysis highlights the importance of electron-withdrawing groups on one or both phenyl rings, visual inspection of the binding poses within the receptor pocket revealed that quinolines adopt different conformations depending on the substituents. Generally, quinoline derivatives bearing a para-nitro group on the benzamide moiety were found to be more selective towards lymphoma cell lines, while those featuring a trimethoxy group on the styryl portion tended to be less active, underlining the importance of steric hindrance in receptor interaction, which may hinder optimal pocket accommodation. Interestingly, although **35s** was the only quinoline to exhibit nanomolar activity against SU-DHL-8, it showed no activity on the other lymphoma lines, further supporting the hypothesis that the presence of electron-withdrawing groups on the benzamide moiety is crucial to broaden the activity spectrum of quinoline derivatives. Finally, it is important to note that the differential activity of quinolines across lymphoma cell lines suggests that SIRT6 may not be the only molecular target involved in their biological effect. Indeed, the literature reports the involvement of SIRT6 in the PI3K/Akt/FoxO signaling pathway,[112] and further investigations into alternative targets are warranted to more precisely elucidate the mechanism of action of these derivatives.

To assess the toxicity of quinolines **35g**, **35q**, **35s**, and **35ag**, an antiproliferative assay was performed on peripheral blood mononuclear cells (PBMCs) derived from a healthy donor. All tested compounds showed no cytotoxic effects ($IC_{50} > 10$ μM) on both resting PBMCs and PBMCs stimulated with phytohemagglutinin (PHA) to induce proliferation.

5.11 Induced apoptotic process by quinoline derivative 35g

To evaluate the pro-apoptotic activity of compound **35g**, flow cytometry assays were performed on two cancer cell lines, TOLEDO and VL51, treated at concentrations of 1 µM and 2 µM. Analysis of apoptosis using Annexin V/propidium iodide (PI) double staining (Figure 18-A) revealed a clear dose-dependent increase in both late apoptotic (AnV+/PI+) cell populations, accompanied by a reduction in the viable cell fraction (AnV−/PI−). This effect was particularly pronounced at 2 µM and reached high statistical significance, indicating that **35g** effectively induces apoptosis in both cell lines. To further investigate the mechanism of cell death, mitochondrial membrane potential was assessed using Tetramethylrhodamine Ethyl ester (TMRE) staining (Figure 18-B). A significant increase in the percentage of TMRE-negative cells, especially in the VL51 line, confirmed the involvement of the intrinsic mitochondrial apoptotic pathway. Representative histograms (Figure 18-C) clearly show a leftward shift in TMRE fluorescence following treatment, consistent with marked mitochondrial depolarization. In parallel, the production of mitochondrial ROS was measured using the MitoSOX assay (Figure 18-D). A dose-dependent increase in the MitoSOX-positive cell population was observed upon treatment with **35g**, particularly at 2 µM, suggesting enhanced oxidative stress. This finding is further supported by the fluorescence histograms (Figure 18-E), which exhibit a shift toward higher fluorescence intensities in treated cells. Taken together, these results demonstrate that compound **35g** induces apoptosis in TOLEDO and VL51 cells through a mitochondria-mediated mechanism, involving both loss of mitochondrial membrane potential and increased ROS production.

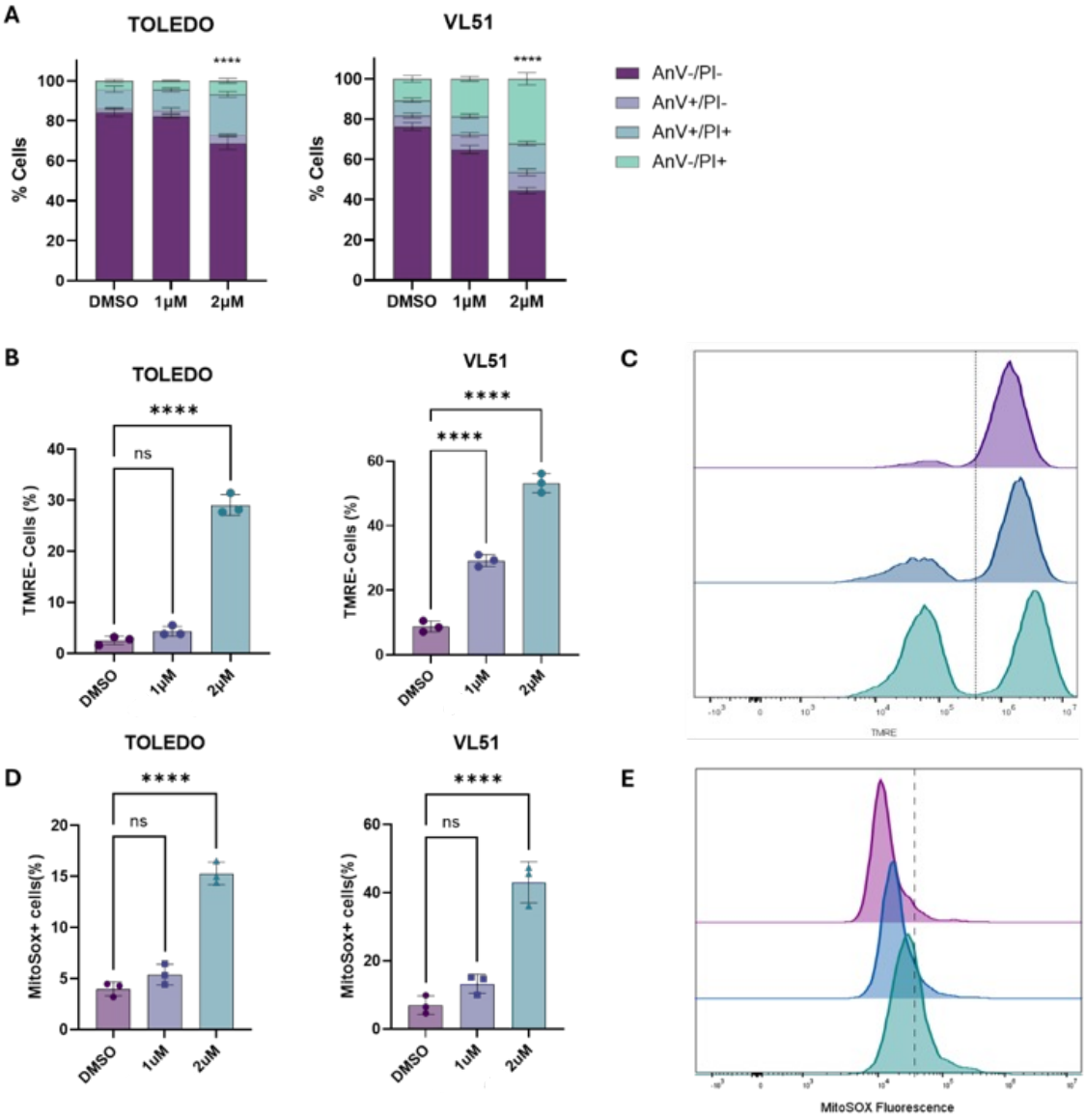

Figure 18. Apoptotic effects caused by **35g**. TOLEDO and VL51 cells were treated with the indicated concentrations of **35g** for either 24 and 48 hours and then were analyzed by flow cytometry after double staining with Annexin-V-FITC and PI. Data are expressed as the mean ± SE from the dose−response curves of three independent experiments.

5.12 Cell cycle assay

To further investigate the effects of compound **35g** on cell growth, its influence on DNA replication and cell cycle dynamics was assessed in TOLEDO and VL51 lymphoma cell lines. Cell proliferation was first evaluated by measuring 5-ethynyl-2'-deoxyuridine (EdU) incorporation, a marker of active DNA synthesis. As shown in Figure 19-A, treatment with **35g** led to a clear, dose-dependent reduction in the percentage of EdU-positive cells in

both cell lines. Notably, at 2 µM, the proportion of replicating cells dropped significantly compared to the DMSO control, indicating a marked inhibition of DNA synthesis. These findings are visually confirmed by the flow cytometry histograms (Figure 19-B), where EdU fluorescence intensity is notably decreased in treated cells. To understand whether this reduction in proliferation was associated with specific changes in the cell cycle, DNA content analysis was performed. As reported in Figure 19-C, **35g** treatment caused a substantial accumulation of cells in the G_2/M phase, accompanied by a consistent decrease in the G_1 population. This effect was again dose-dependent and highly significant in both cell models. Taken together, these results suggest that **35g** impairs cell proliferation by inducing a block in G_2/M phase, effectively halting DNA replication and progression through the cell cycle. The observed arrest is in agreement with the decrease in EdU incorporation, pointing to a mechanism of action that interferes with checkpoint regulation.

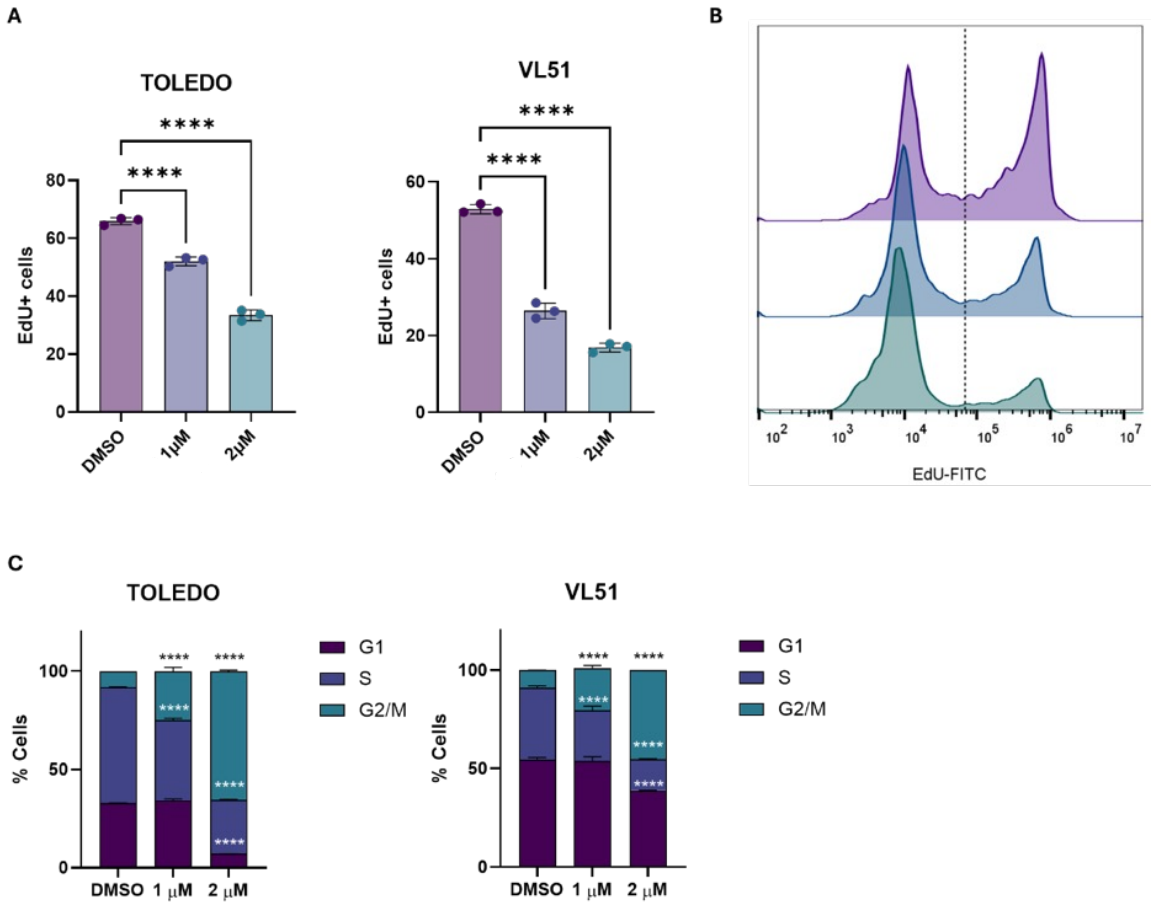

Figure 19. Quantitative analysis of cell cycle phase distribution in TOLEDO and VL51 cells after 24 h treatment with **35g** at the concentration of 1 and 2 µM. Cells were stained with PI to analyzed the DNA content by flow cytometry. Data are expressed as the mean ± SE from the dose−response curves of three independent experiments.

6. CONCLUSIONS

In the PhD thesis I employed a multidisciplinary strategy to identify and optimize novel SIRT6 inhibitors. This integrated approach included computational modeling, synthetic chemistry, and biological evaluation to investigate structure–activity relationships and pharmacological potential of a series of novel small molecules. Initially, I performed a comprehensive analysis of the SIRT6 binding site using molecular docking, molecular MD simulations, and BPMDs. These techniques provided key insights into the conformational flexibility of the binding pocket and highlighted the crucial interactions stabilizing known activators and inhibitors. A Fragment-based VS was then performed to identify new chemotypes targeting SIRT6 with optimal binding pose and good interaction profiles. Then, I focused on the synthesis of three distinct classes of compounds. First, I synthesized a sulfone-based derivative, rationally designed based on insights gained from the structural features of TSN and its known interactions with SIRT6. Secondly, I developed a focused set of five meta-substituted carboxamides, selected following detailed docking analyses that highlighted their optimal positioning and consistent H-bond patterns with critical SIRT6 residues. These compounds featured a central amide linker and were prioritized for synthesis due to their promising binding modes. Lastly, I designed and synthesized a library of thirty-four quinoline-based derivatives, aiming to investigate a novel chemotype for its potential to modulate SIRT6 activity and its antiproliferative effects in lymphoma cell lines. These findings were further supported by biological assays, in which selected derivatives exhibited significant antiproliferative activity in DLBCL cell lines. A noteworthy result was the dual behavior observed for some quinoline derivatives, which induced apoptosis and cell cycle arrest in lymphoma cell lines expressing SIRT6, thus reinforcing their potential therapeutic value. This work has provided not only novel molecular entities with potential anticancer applications but has also improved the current knowledge of the structural elements responsible for SIRT6 modulation. In conclusion, this PhD journey has allowed me to apply and consolidate my expertise in medicinal chemistry, computational drug design, and chemical biology. The molecules developed herein represent a solid foundation for further optimization and preclinical investigation, while the methodological pipeline established throughout this research may serve as a valuable framework for the rational design of future SIRT6 modulators. These results, although highly encouraging, require further validation through enzymatic assays on SIRT6 to confirm it as the actual molecular target. For this purpose, sixteen compounds (**19g, 23a, 23b, 24a, 25a, 25c, 35a, 35g, 35o, 35p, 35q, 35r,**

35s, 35ad, 35af, 35ag) have been selected for future investigation, and binding assays are currently in progress at the University of Palermo.

7. ACKNOWLEDGMENTS

I would like to express my deepest gratitude to my Tutor, Professor Maria Valeria Raimondi, whose guidance, expertise, and constant support have been invaluable throughout the course of my PhD. Her insightful advice and scientific vision have greatly contributed to the development and completion of this work.

My sincere thanks also go to my Co-tutor, Professor Marco Tutone, for his valuable supervision of the computational studies, and to Dr. Giulia Culletta for her support throughout this work.

I am deeply grateful to Drs. Ugo Perricone, Maria De Rosa, Simona Di Martino, and Giovanna Li Petri of the Ri.MED Foundation, for allowing me to deepen my knowledge in computational chemistry, for kindly providing the compounds used in the biological assays on SIRT6, for their assistance in the chemical characterization of the molecules, and for hosting me during my training in synthetic chemistry.

I would also like to thank Professor Clemens Steegborn and Dr. Michael Weyand from the University of Bayreuth for performing the binding studies on SIRT6.

Special thanks to Professor Paola Barraja for providing additional funding that supported my research activities.

I am also grateful to Professor Giampietro Viola and Dr. Roberta Bortolozzi from the University of Padua, for carrying out the biological evaluations on lymphoma cell lines.

Finally, I would like to thank Professor Ralph Holl for sharing his expertise in organic synthesis and for kindly hosting me at the University of Hamburg during my research period abroad.

8. EXPERIMENTALS

8.1 COMPUTATIONAL STUDIES

8.1.1 Systems preparation

Crystal structures of human SIRT6 were retrieved from the Protein Data Bank (PDB) and processed using the Protein Preparation Wizard tool available in the Schrödinger Suite (Release 2021-1, Schrödinger, New York, NY). The OPLS4 force field[113] was employed for energy minimization, and Epik (Schrödinger, Release 2021-1)[114] was used to assign ionization states at physiological pH (7.4 ± 0.2). Hydrogen atoms were added to the systems, and missing loops or side chains were reconstructed using the Prime module.

Non-structural sulfate ions were removed from the binding site, whereas structural Zn^{2+} ions were retained, as they contribute to the stability of the enzyme but are not catalytically active, in accordance with literature reports. Selected crystallographic water molecules were also preserved, particularly those located in proximity to residues Ala53, Ile61, and Pro62, due to their potential role in forming stabilizing H-bonds with ligands.

8.1.2 Ligands preparation

All chemical structures used in this study were prepared using the LigPrep tool (Release 2021-1, Schrödinger, New York, NY). The OPLS4 force field was applied for geometry optimization. Possible ionization states were generated at pH 7.0 ± 2.0 using Epik.[114] All possible combinations of stereoisomers and tautomers were generated. A maximum of 32 conformers per ligand was selected, and chiral centers were preserved when specified. The output structures were used for subsequent molecular docking studies.

8.1.3 Molecular Docking

Molecular docking studies were performed using the GLIDE software package (Schrödinger Release 2021-1, New York, NY) according to standard protocols.[115] Grid generation was carried out centering on the co-crystallized ligand within the active site. The van der Waals radii scaling factor was set to 0.8 Å, and a partial atomic charge cut-off of 0.15 was applied to soften nonpolar interactions. Ligands were flexible during docking using standard precision (SP) mode. The accuracy of the docking protocol was validated through cognate docking of co-crystallized ligands, and the resulting binding poses were assessed by

calculating the root-mean-square deviation (RMSD) between the predicted and experimental coordinates.

8.1.4 Molecular Dynamics

Three independent molecular dynamics (MD) simulations of 500 ns for each were carried out using the Desmond (Schrödinger New York, 2021-1),[116] and OPLS4 was chosen as the force field. The complexes were included in an orthorhombic box using the TIP3P water model. Ions were added to neutralize the charges. The systems were minimized and equilibrated at the temperature of 310 K and the pressure of 1.01325 bar. The systems were simulated as an NPT ensemble; a Nose–Hoover (NHC) thermostat was selected with a relaxation time of 1 picosecond, and Martyna–Tobia–Klein (MTK) barostat was set to regulate the pressure, with relaxation time of 2 ps. The integration time step was chosen at 2 fs. The SHAKE algorithm was used to keep the hydrogen–heavy atom bonds rigid. A 9 Å cut-off radius was set for the short-range Coulomb interactions, and smooth particle mesh Ewald was used for the long-range interactions. Systems' stability was assessed by analyzing the root mean square deviation (RMSD) of the protein and ligand coordinates, after alignment, compared to their initial positions. The visualization and the analysis of the MD trajectories were performed using the Desmond simulation analysis tools in Maestro.

8.1.5 Binding Pose Metadynamics

Binding Pose Metadynamics (BPMD) simulations were carried out to assess the stability of ligand–protein interactions, using an enhanced sampling protocol based on metadynamics.[117] This method applies a bias potential to explore the free energy landscape and evaluate the persistence of binding poses beyond standard molecular dynamics or docking predictions. Each complex was subjected to 10 independent metadynamics simulations. BPMD outputs three scoring metrics to characterize pose stability: PoseScore: the average root-mean-square deviation (RMSD) of the ligand heavy atoms relative to the starting pose over the course of the simulation. Higher values indicate greater structural deviation and reduced stability; PersistenceScore (PersScore): a metric ranging from 0 to 1, reflecting the average hydrogen bond persistence in the final 2 ns of simulation across all runs. A value of 1 indicates full retention of initial interactions; a score of 0 suggests a complete loss of key contacts; CompositeScore (CompScore): a linear combination of the PoseScore and PersScore, offering a comprehensive index of binding pose stability; lower

scores indicate more robust binding configurations. Simulations were executed using a single computing node equipped with an NVIDIA GeForce RTX2070 GPU card.

8.1.6 Virtual Screening

A dataset of over 25,000 small molecules, collected from both the ChEMBL database (https://www.ebi.ac.uk/chembl/) and an in-house compound library, was prepared using LigPrep (Schrödinger, New York, 2022-1), following the procedure previously described. The prepared library was subjected virtual screening campaign using GLIDE (Schrödinger, New York, 2022-1) in standard precision (SP) mode, without constraints. After docking, the top 5% of poses, based on their docking scores, were selected and visually inspected to assess the quality of the binding mode, focusing on key interactions within the SIRT6 active site.

8.2 ORGANIC SYNTHESIS

8.2.1 General methods

All reagents and solvents were purchased from Sigma-Aldrich, TCI, Fluka, Merck and Across and used without further purification. Microwave reactions were performed with an Anton Paar GmbH - Monowave™ 300. All reactions were monitored by thin-layer chromatography (TLC) on precoated TLC plates (0.2 mm Kieselgel 60 G F254, Merck). Developed plates were air-dried and visualized by exposure to UV light ($\lambda = 254$ and 365 nm). Products were purified by crystallization from EtOH or by medium pressure liquid chromatography (MPLC). MPLC was performed using a CombiFlash RF200 (TeleDyne Isco) and prepacked silica gel RediSep cartridge (35-75 μm). All compounds were named following IUPAC rules as applied by ChemDraw Professional 16.0. All compounds were fully characterized by spectroscopic data. The nuclear magnetic resonance (NMR) spectra were recorded on a Bruker AC 300 (^{1}H: 300 MHz, ^{13}C: 75 MHz) at room temperature using DMSO-d_6 or $CDCl_3$ as solvents and tetramethylsilane (TMS) as internal standard. Chemical shifts (δ) for ^{1}H and ^{13}C spectra were recorded in parts per million (ppm). Data are reported as follows: chemical shift (ppm), multiplicity (indicated as: s, singlet; br s, broad singlet; m, multiplet; dd, doublet of doublets; br d, broad doublet), integrated intensity, assignments.

8.2.2 Synthesis of 5-(phenylsulfonyl)furan-2-carboxamide 19g

In a round-bottom flask equipped with a magnetic stir bar and cooled in an ice bath, 5-(phenylsulfonyl)furan-2-carboxylic acid (100 mg, 0.396 mmol, **22**) was dissolved in DMF. EDC·HCl (2.0 eq), HOBt (0.2 eq), DMAP (2.0 eq), and NH_4Cl (1.0 eq) were added sequentially under stirring. The reaction mixture was stirred at room temperature for 24 hours. Upon completion, the solvent was removed under reduced pressure using a rotary evaporator. The crude product was purified by flash cromatography and eluted with EtOAc to afford compound **19g**. Yield: 46.8%; ^{1}H NMR (300 MHz, DMSO-d_6) δ: 7.27-7.28, 7.51-7.52 (dd, 2H, C_4H_2O); 7.75, 8.11 (br d, 2H, CO-NH_2); 7.76-8.03 (m, 5H, C_6H_5). ^{13}C NMR (75 MHz, DMSO-d_6) δ: 114.94 (CH); 119.62 (CH); 128.07 (2xCH); 130.45 (2xCH); 135.15 (CH); 139.33 (C); 150.22 (C); 152.18 (C); 158.36 (CO).

8.2.3 Synthesis of Methylammonium chloride

In a round-bottom flask equipped with a magnetic stir bar and cooled in an ice bath, hydrochloric acid (37%, 1.5 mL, 0.018 mmol) was placed under stirring. A solution of methylamine in absolute ethanol (8.03 M, 2.24 mL, 0.018 mmol) was then added dropwise

under continuous stirring at 0 °C. After 15 minutes at 0 °C, the solvent was removed under reduced pressure using a rotary evaporator to afford a white solid. The obtained residue was dried overnight in an oven at 150 °C and stored in a desiccator over silica gel. The crude methylammonium chloride was used without further purification.

8.2.4 Synthesis of Methyl 2-(methylcarbamoyl)isonicotinate 29

Method 1. In a round-bottom flask equipped with a magnetic stir bar and cooled in an ice bath, 4-(methoxycarbonyl)picolinic acid (100 mg, 0.552 mmol, **28**) was dissolved in anhydrous DMF (3 mL). EDC·HCl (2.0 eq), HOBt (0.2 eq), DMAP (2.0 eq), and CH_3NH_3Cl (1.0 eq) were added sequentially under stirring. The reaction mixture was stirred at room temperature for 24 hours. Upon completion, the solvent was removed under reduced pressure using a rotary evaporator. The crude product was purified by MPLC and eluted with EtOAc to afford compound **29**. Yield: 68.3%.

Method 2. In a 30 mL microwave reaction tube equipped with a magnetic stir bar and cooled in an ice bath, 4-(methoxycarbonyl)pyridine-2-carboxylic acid (100 mg, 0.552 mmol, **28**) was dissolved in anhydrous DMF (3 mL). EDC·HCl (2.0 eq), HOBt (0.2 eq), DMAP (2.0 eq), and CH_3NH_3Cl (1.0 eq) were added sequentially. The microwave reactor was set with the following parameters: T = 80 °C, Power = 150 W, Time = 40 minutes (2 cycles of 20 minutes each) and vigorous magnetic stirring (600 rpm). Upon completion, the solvent was removed under reduced pressure using a rotary evaporator. The crude product was purified by MPLC and eluted with EtOAc to afford compound **29**. Yield: 83.0%.

(**29**): ^{1}H NMR (300 MHz, $CDCl_3$): δ 3.06, 3.07 (d, 3H, N-CH_3); 3.98 (s, 3H, O-CH_3); 7.98-8.01, 8.68-8.72 (m, 4H, C_5H_3N, NH-Me). ^{13}C NMR (75 MHz, $CDCl_3$): δ 26.4 (N-CH_3); 52.86 (O-CH_3); 121.48 (CH); 125.32 (CH); 139.03 (C); 148.87 (CH); 150.99 (C); 164.13 (CO); 165.08 (CO).

8.2.5 Synthesis of 2-(methylcarbamoyl)isonicotinic acid 13

Method 1. In a round-bottom flask, methyl 2-(methylcarbamoyl)isonicotinate (60 mg, 0.378 mmol, **29**) was dissolved in MeOH (5 mL), and KOH 1 M (1.7 mL, 4.5 eq) was added. The reaction mixture was refluxed for 1 hour. Upon completion, the organic solvent was removed under reduced pressure using a rotary evaporator, and the resulting aqueous solution was acidified with 3 M HCl to pH 4–5. The crude product was purified by MPLC and eluted with EtOAc/MeOH (98:2) containing 0.1% formic acid affording compound **13**. Yield: 37.4%.

Method 2. In a 30 mL microwave reaction vessel, methyl 2-(methylcarbamoyl)isonicotinate (260 mg, 1.338 mmol, **29**) was dissolved in EtOH (5 mL), and KOH 1 M (4.42 mL, 4.5 eq) was added. The microwave reactor was set with the following parameters: T = 120 °C, Power = 200 W, Time = 4 minutes and vigorous magnetic stirring (600 rpm). Upon completion, the organic solvent was removed under reduced pressure using a rotary evaporator and the aqueous phase was acidified with 3 M HCl to pH 4-5 to afford compound **13** as a pure solid. Yield: 85.0%.

(**13**): ^{1}H NMR (300 MHz, DMSO-d_6): δ 2.83, 2.84 (d, 3H, N-CH_3); 7.98, 7.99 (dd, 1H, NH-Me); 8.38–8.39, 8.81–8.98 (m, 3H, C_5H_3N); 13.78 (br s, 1H, OH). ^{13}C NMR (75 MHz, DMSO-d_6): δ 26.69 (N-CH_3); 121.05 (CH); 125.67 (CH); 140.20 (C); 150.12 (CH); 151.60 (C); 164.16 (CO); 166.31 (CO).

8.2.6 Synthesis of [1,2,4]triazolo[4,3-a]pyridine-6-carboxylic acid 14

Method 1. A solution of 6-hydrazinylpyridine-3-carboxylic acid (250 mg, 1.632 mmol, **30**) in formic acid (4 mL) was heated to reflux for 16 hours. Upon completion, the solvent was removed under reduced pressure using a rotary evaporator. The resulting residue was washed with cold water and collected by vacuum filtration to afford compound **14** as a pure product and dried in a desiccator over silica gel. Yield: 80.6%.

Method 2. In a 30 mL microwave reaction vessel, 6-hydrazinylpyridine-3-carboxylic acid (100 mg, 0.649 mmol, **30**) was dissolved in formic acid (4 mL). The microwave reactor was set with the following parameters: T = 100 °C, Power = 150 W, Time = 20 minutes and vigorous magnetic stirring (600 rpm). Upon completion, the solvent was removed under reduced pressure using a rotary evaporator. The resulting precipitate was collected by vacuum filtration, washed with cold water affording compound **14** as a pure solid and dried in a desiccator over silica gel. Yield: 95.4%.

(**14**):^{1}H NMR (DMSO-d_6): δ 7.69-7.81, 9.25-9.34 (m, 3H, C_5H_3N); 13.47 (br s, 1H, OH). ^{13}C NMR (DMSO-d_6): δ 115.06 (CH); 128.26 (C); 127.62 (CH); 130.27 (CH); 138.08 (CH); 149.18 (C); 165.66 (CO).

8.2.7 Synthesis of 1H-benzo[d][1,2,3]triazole-5-carboxylic acid 17

To an ice-cooled solution (T = 0-5 °C) of 3,4-diaminobenzoic acid (100 mg, 0.657 mmol, **31**) in glacial AcOH (1.5 mL), $NaNO_2$ (1.1 eq), previously dissolved in the minimum amount of deionized water, was added dropwise under stirring. After 1 hour at 0-5 °C, the reaction mixture was allowed to stir overnight at room temperature. The resulting precipitate was

collected by vacuum filtration, washed with cold water affording compound **17** as a pure solid and dried in a desiccator over silica gel. Yield: 93.2%; ^{1}H NMR (DMSO-d_6): δ 7.93-8.52 (m, 3H, C_6H_3); 14.47 (br s, 2H, OH, NH). ^{13}C NMR (DMSO-d_6): δ 114.35; 118.84; 126.88; 128.05; 167.55 (CO).

8.2.8 Synthesis of 3-aminobenzamide 26a

Method 1. In a round-bottom flask equipped with a magnetic stir bar and cooled in an ice bath, 3-aminobenzoic acid (100 mg, 0.729 mmol, **32a**) was dissolved in anhydrous DMF (4 mL). EDC·HCl (2.0 eq), HOBt (0.2 eq), DMAP (2.0 eq), and NH_4Cl (1.0 eq) were added sequentially under stirring. The reaction mixture was stirred at room temperature for 24 hours. Upon completion, the solvent was removed under reduced pressure using a rotary evaporator, and the crude product was purified by solid-phase extraction (SPE) using a silica gel cartridge, conditioned and eluted with EtOAc, affording compound **26a**. Yield: 90.0%.

Method 2. In a 30 mL microwave reaction vessel, 3-aminobenzoic acid (100 mg, 0.729 mmol, **32a**) was dissolved in anhydrous DMF (4 mL). EDC·HCl (2.0 eq), HOBt (0.2 eq), DMAP (2.0 eq), and NH_4Cl (1.0 eq) were added sequentially. The microwave reactor was set with the following parameters: T = 80 °C, Power = 150 W, Time = 40 minutes (2 cycles of 20 minutes each) and vigorous magnetic stirring (600 rpm). Upon completion, the solvent was removed under reduced pressure using a rotary evaporator, and the crude product was purified by solid-phase extraction (SPE) using a silica gel cartridge, conditioned and eluted with EtOAc, affording compound **26a**. Yield: 97.8%.

(**26a**): ^{1}H NMR (DMSO-d_6): δ 5.17 (s, 2H, NH_2); 6.66-6.69, 6.96-7.08 (m, 4H, C_6H_4); 7.12, 7.71 (br d, 2H, CO-NH_2). ^{13}C NMR (DMSO-d_6): δ 113.42 (CH); 115.13 (CH); 116.90 (CH); 128.92 (CH); 135.57 (C); 149.04 (C); 169.14 (CO).

8.2.9 Synthesis of 6-aminopicolinamide 26b

Method 1. In a round-bottom flask equipped with a magnetic stir bar and cooled in an ice bath, 6-aminopicolinic acid (100 mg, 0.724 mmol, **32b**) was dissolved in anhydrous DMF (3 mL). EDC·HCl (2.0 eq), HOBt (0.2 eq), DMAP (2.0 eq), and NH_4Cl (1.0 eq) were added sequentially under stirring. The reaction mixture was stirred at room temperature for 24 hours. Upon completion, the solvent was removed under reduced pressure using a rotary evaporator, and the crude product was purified by solid-phase extraction (SPE) using a silica gel cartridge, conditioned and eluted with EtOAc/Acetone (1:1), affording compound **26b**. Yield: 86.7%.

Method 2. In a 30 mL microwave reaction vessel, 6-aminopicolinic acid (100 mg, 0.724 mmol, **32b**) was dissolved in anhydrous DMF (5 mL). EDC·HCl (2.0 eq), HOBt (0.2 eq), DMAP (2.0 eq), and NH_4Cl (1.0 eq) were added sequentially. The microwave reactor was set with the following parameters: T = 80 °C, Power = 150 W, Time = 40 minutes (2 cycles of 20 minutes each) and vigorous magnetic stirring (600 rpm). Upon completion, the solvent was removed under reduced pressure using a rotary evaporator, and the crude product was purified by solid-phase extraction (SPE) using a silica gel cartridge, conditioned and eluted with EtOAc/acetone (1:1), affording compound **26b**. Yield: 68.0%.

(**26b**): ^{1}H NMR (DMSO-d_6): δ 6.09 (s, 2H, NH_2); 6.60-6.63, 7.15-7.17, 7.49-7.54 (m, 3H, C_6H_3N); 7.44, 7.64 (br d, 2H, CO-NH_2). ^{13}C NMR (DMSO-d_6): δ 110.41 (CH); 111.65 (CH); 138.48 (CH); 148.79 (C); 159.06 (C); 166.93 (CO).

8.2.10 Synthesis of 6-aminopyrazine-2-carboxylic acid 26c

Method 1. In a round-bottom flask equipped with a magnetic stir bar and cooled in an ice bath, 6-aminopyrazine-2-carboxylic acid (500 mg, 3.594 mmol, **32c**) was dissolved in anhydrous DMF (9 mL). EDC·HCl (2.0 eq), HOBt (0.2 eq), DMAP (2.0 eq), and NH_4Cl (1.0 eq) were added sequentially under stirring. The reaction mixture was stirred at room temperature for 24 hours. Upon completion, the solvent was removed under reduced pressure using a rotary evaporator. The crude product was purified by MPLC and eluted with EtOAc affording compound **26c**. Yield: 90.4%.

Method 2. In a 30 mL microwave reaction vessel, 6-aminopyrazine-2-carboxylic acid (100 mg, 0.7188 mmol, **32c**) was dissolved in anhydrous DMF (4 mL). EDC·HCl (2.0 eq), HOBt (0.2 eq), DMAP (2.0 eq), and NH_4Cl (2.0 eq) were added sequentially. The microwave reactor was set with the following parameters: T = 80 °C, Power = 150 W, Time = 40 minutes (2 cycles of 20 minutes each) and vigorous magnetic stirring (600 rpm). Upon completion, the solvent was removed under reduced pressure using a rotary evaporator. Upon completion, the solvent was removed under reduced pressure using a rotary evaporator, and the crude product was purified by solid-phase extraction (SPE) using a silica gel cartridge, conditioned and eluted with EtOAc/MeOH (8:2), affording compound **26c**. Yield: 44.0%.

(**26c**): ^{1}H NMR (DMSO-d_6): δ 6.63 (s, 2H, NH_2); 7.63 (br s, 2H, CO-NH_2); 8.04 (s, 1H, $C_6H_2N_2$); 8.23 (s, 1H, $C_6H_2N_2$). ^{13}C NMR (DMSO-d_6): δ 130.40 (CH); 135.79 (CH); 142.46 (C); 155.09 (C); 166.29 (CO).

8.2.11 Synthesis of 5-nitrofuran-2-carboxamide 33a

Method 1. In a round-bottom flask equipped with a magnetic stir bar and cooled in an ice bath, 5-nitrofuran-2-carboxylic acid (100 mg, 0.637 mmol, **34a**) was dissolved in anhydrous DMF (3 mL). EDC·HCl (2.0 eq), HOBt (0.2 eq), DMAP (2.0 eq), and NH_4Cl (1.0 eq) were added sequentially under stirring. The reaction mixture was stirred at room temperature for 24 hours. Upon completion, the solvent was removed under reduced pressure using a rotary evaporator. The crude product was purified by flash column cromatography and eluted with EtOAc affording compound **33a**. Yield: 75.2%.

Method 2. In a 30 mL microwave reaction vessel, 5-nitrofuran-2-carboxylic acid (100 mg, 0.637 mmol, **34a**) was dissolved in anhydrous DMF (3 mL). EDC·HCl (2.0 eq), HOBt (0.2 eq), DMAP (2.0 eq), and NH_4Cl (1.0 eq) were added sequentially. The microwave reactor was set with the following parameters: T = 80 °C, Power = 150 W, Time = 40 minutes (2 cycles of 20 minutes each) and vigorous magnetic stirring (600 rpm). Upon completion, the solvent was removed under reduced pressure using a rotary evaporator. The crude product was purified by flash column cromatography and eluted with EtOAc affording compound **33a**. Yield: 80.1%.

(**33a**): ^{1}H NMR (DMSO-d_6): δ 7.38-7.39, 7.71-7.72 (dd, 2H, C_4H_2O); 7.88, 8.24 (br d, 2H, CO-NH_2). ^{13}C NMR (DMSO-d_6): δ 113.82 (CH); 116.17 (CH); 148.87 (C); 151.91 (C); 158.03 (CO).

8.2.12 Synthesis of 5-nitrothiophene-2-carboxamide 33b

Method 1. In a round-bottom flask equipped with a magnetic stir bar and cooled in an ice bath, 5-nitrothiophene-2-carboxylic acid (100 mg, 0.577 mmol, **34b**) was dissolved in anhydrous DMF (3 mL). EDC·HCl (2.0 eq), HOBt (0.2 eq), DMAP (2.0 eq), and NH_4Cl (1.0 eq) were added sequentially under stirring. The reaction mixture was stirred at room temperature for 24 hours. Upon completion, the solvent was removed under reduced pressure using a rotary evaporator. The crude product was purified by flash column cromatography and eluted with EtOAc affording compound **33b** Yield: 77.9%.

Method 2. In a 30 mL microwave reaction vessel, 5-nitrothiophene-2-carboxylic acid (100 mg, 0.577 mmol, **34b**) was dissolved in anhydrous DMF (3 mL). EDC·HCl (2.0 eq), HOBt (0.2 eq), DMAP (2.0 eq), and NH_4Cl (1.0 eq) were added sequentially. The microwave reactor was set with the following parameters: T = 80 °C, Power = 150 W, Time = 40 minutes (2 cycles of 20 minutes each) and vigorous magnetic stirring (600 rpm). Upon completion, the solvent was removed under reduced pressure using a rotary evaporator. The crude

product was purified by flash column cromatography and eluted with EtOAc affording compound **33b**. Yield: 80.1%.

(**33b**): ^{1}H NMR (DMSO-d_6): δ 7.75-7.76, 8.10-8.11 (dd, 2H, C_4H_2S); 7.94, 8.41 (br d, 2H, CO-NH_2). ^{13}C NMR (DMSO-d_6): δ 128.24 (CH); 130.62 (CH); 147.30 (C); 153.46 (C); 161.66 (CO).

8.2.13 Synthesis of N-(3-carbamoylphenyl)-1H-1,2,3-benzotriazole-5-carboxamide 25a

Method 1. In a round-bottom flask equipped with a magnetic stir bar and cooled in an ice bath, 1H-benzo[d][1,2,3]triazole-5-carboxylic acid (103.75 mg, 0.636 mmol, **17**) and 3-aminobenzamide (1.0 eq, **26a**) were dissolved in anhydrous DMF (2 mL). EDC·HCl (2.0 eq), HOBt (0.2 eq), and DMAP (2.0 eq) were added sequentially under stirring. The reaction mixture was stirred at room temperature for 24 hours. Upon completion, water was added and the mixture was extracted with EtOAc (3 × 2 mL) to remove excess reagents. The aqueous layer was evaporated under reduced pressure using a rotary evaporator. The resulting oily residue was treated with a few drops of EtOH, leading to the formation of a solid, which was filtered and purified by flash column chromatography and eluted with EtOAc/MeOH (8:2), affording compound **25a**. Yield: 8.2%.

Method 2. In a 30 mL microwave reaction vessel, compound **17** (100 mg, 0.613 mmol) was dissolved in anhydrous DMF (3 mL). EDC·HCl (2.0 eq), HOBt (0.2 eq), DMAP (2.0 eq), and compound **26a** (1.0 eq) were added sequentially. The microwave reactor was set with the following parameters: T = 80 °C, Power = 150 W, Time = 40 minutes (2 cycles of 20 minutes each) with vigorous magnetic stirring (600 rpm). Upon completion, the solvent was removed under reduced pressure using a rotary evaporator. The crude product was purified by flash column chromatography and eluted with EtOAc/MeOH (8:2), affording compound **25a**. Yield: 12.7%.

Method 3. In a round-bottom flask equipped with a magnetic stir bar and cooled in an ice bath, compounds **17** (150 mg, 0.919 mmol) and **26a** (1.1 eq) were dissolved in anhydrous DMF (2.4 mL). NMI (3.5 eq) and TCFH (1.8 eq) were added sequentially under stirring. The reaction mixture was stirred at room temperature for 24 hours. Upon completion, the solvent was removed under reduced pressure using a rotary evaporator, and the crude product was purified by flash column chromatography and eluted with EtOAc/MeOH (97:3), affording compound **25a**. Yield: 9.4%.

Method 4. In a 30 mL microwave reaction vessel, compound **17** (100 mg, 0.613 mmol) was dissolved in anhydrous DMF (4 mL). Compound **26a** (1.3 eq), NMI (3.5 eq), and TCFH (1.2

eq,) were added sequentially. The microwave reactor was set with the following parameters: T = 80 °C, Power = 150 W, Time = 80 minutes (4 cycles of 20 minutes each). Upon completion, the solvent was removed under reduced pressure using a rotary evaporator. The crude product was purified by MPLC using EtOAc/MeOH (8:2) as eluent. Yield: 45.0%. (**25a**): ^{1}H NMR (300 MHz, DMSO-d_6) δ:7.34-8.59 (m, 10H, C_6H_3, C_6H_4, CO-NH_2); 10.47 (s, 1H, NH).

Method 4, due to the higher yield achieved, was selected for the synthesis of the other carboxamides.

8.2.14 Synthesis of N^4-(3-carbamoylphenyl)-N^2-methylpyridine-2,4-dicarboxamide 23a

Purified by flash column chromatography and eluted with EtOAc/MeOH (95:5). Yield: 30.2%; ^{1}H NMR (300 MHz, DMSO-d_6) δ: 2.86, 2.87 (d, 3H, N-CH_3); 7.59-8.93 (m, 10H, NH-Me, C_6H_4, C_5H_3N, CO-NH_2); 10.99 (s, 1H, NH). ^{13}C NMR (DMSO-d_6): δ 26.73 (N-CH_3); 112.01 (C); 119.03 (C); 119.87 (CH); 123.84 (CH); 124.73 (CH); 125.64 (CH); 128.28 (CH); 130.72 (CH); 139.82 (C); 143.25 (CO); 149.84 (CH); 151.48 (CO); 164.27 (CO).

8.2.15 Synthesis of N^4-(6-carbamoylpyridin-2-yl)-N^2-methylpyridine-2,4-dicarboxamide 23b

Purified by flash column chromatography and eluted with EtOAc. Yield: 20.5%; ^{1}H NMR (300 MHz, DMSO-d_6) δ: 2.85, 2.87 (d, 3H, N-CH_3); 7.84-8.89 (m, 9H, NH-Me, 2 x C_5H_3N, CO-NH_2); 11.76 (s, 1H, NH).

8.2.16 Synthesis of N^4-(6-carbamoylpyridin-2-yl)-N^2-methylpyridine-2,4-dicarboxamide 24a

Purified by solid-phase extraction (SPE) using a silica gel cartridge, conditioned and eluted with EtOAc/MeOH (9:1). Additional purification by flash column chromatography was required using EtOAc/MeOH (9:1). Yield: 25.0%. ^{1}H NMR (300 MHz, DMSO-d_6) δ: 7.42-8.27 (m, 9H, C_6H_3N, C_6H_4, CO-NH_2); 10.77 (s, 1H, NH).

8.2.17 Synthesis of N-(6-carbamoylpyrazin-2-yl)-1H-benzo[d][1,2,3]triazole-5-carboxamide 25c

Purified by flash column chromatography and eluted with DCM/MeOH (85:15). Yield: 32.0%; ^{1}H NMR (300 MHz, DMSO-d_6) δ:7.00-8.72 (m, 8H, C_6H_3N, C_6H_3, CO-NH_2); 10.82 (s, 1H, NH).

8.2.18 Synthesis of 2-methylquinoline-4-carboxylic acid 37

In a 10 mL microwave reaction tube equipped with a magnetic stir bar, isatin (200 mg, 1.36 mmol, **36**) was dissolved in 4 mL of aqueous KOH (10%), followed by the addition of 0.3 mL acetone RPE. The microwave reactor was set with the following parameters: T = 150 °C, Power = 100 W, Time = 30 minutes (2 cycles of 15 minutes each) and vigorous magnetic stirring (600 rpm). The reaction mixture was then allowed to cool to room temperature and acidified to pH < 6.5 using aqueous HCl (37%) affording compound **37** as a pure solid. The resulting solid was washed with cold water, collected by vacuum filtration to afford compound **37** as pure product and dried in a desiccator over silica gel. Yield: 92.7%; ^{1}H NMR (300 MHz, DMSO-d_6) δ: 3.00 (s, 3H, CH_3), 7.87–8.68 (m, 5H, C_9H_5N), 14.20 (br s, 1H, OH); ^{13}C NMR (75 MHz, DMSO-d_6) δ: 21.46 (CH_3), 122.48 (CH), 123.84 (C), 124.57 (CH), 126.65 (CH), 129.80 (CH), 133.65 (CH), 140.59 (C), 143.09 (C), 159.02 (C), 166.40 (CO).

8.2.19 General procedure for the synthesis of the substituted 2-methyl-N-phenylquinoline-4-carboxamides (38a–j)

In a 10 mL microwave reaction tube equipped with a magnetic stir bar, 2-methylquinoline-4-carboxylic acid (100 mg, 0.534 mmol, **37**) was dissolved in anhydrous MeCN (3 mL). EDC·HCl (2.0 eq), HOBt (0.2 eq), DMAP (2.0 eq), and the proper substituted aniline (1.1 eq) were added sequentially. The microwave reactor was set with the following parameters: T = 50 °C, Power = 600 W, Time = 40 minutes (2 cycles of 20 minutes each) and vigorous magnetic stirring (600 rpm). Upon completion, the reaction mixture was allowed to cool at room temperature, and deionized water was added. The resulting precipitate was collected by vacuum filtration, washed with cold water and dried in a desiccator over silica gel. The crude substituted 2-methyl-*N*-phenylquinoline-4-carboxamides (38a–j) were purified by crystallization from EtOH.

8.2.19.1 2-methyl-N-phenylquinoline-4-carboxamide 38a

Purified by crystallization from EtOH. Yield: 78.3%; ^{1}H NMR (300 MHz, DMSO-d_6) δ: 2.74 (s, 3H, CH_3), 7.14–8.11 (m, 10H, C_9H_5N and C_6H_5), 10.78 (s, 1H, NH); ^{13}C NMR (75 MHz, DMSO-d_6) δ: 25.29 (CH_3), 120.37 (3 × CH), 122.86 (C), 124.59 (CH), 125.45 (CH), 127.06 (CH), 129.19 (CH), 129.32 (2 × CH), 130.29 (CH), 139.25 (C), 142.60 (C), 148.10 (C), 159.07 (C), 165.84 (CO).

8.2.19.2 2-methyl-N-(m-tolyl)quinoline-4-carboxamide 38b

Purified by crystallization from EtOH. Yield: 81.3%; ^{1}H NMR (300 MHz, DMSO-d_6) δ: 2.34 (s, 3H, CH_3), 2.75 (s, 3H, CH_3), 6.97–8.10 (m, 9H, C_9H_5N and C_6H_4), 10.69 (s, 1H, NH); ^{13}C NMR (75 MHz, DMSO-d_6) δ: 21.67 (CH_3), 25.01 (CH_3), 117.64 (CH), 120.41 (CH), 120.95 (CH), 122.94 (C), 125.31 (CH), 125.52 (CH), 127.22 (CH), 128.67 (CH), 129.13 (CH), 130.54 (CH), 138.52 (C), 139.12 (C), 143.11 (C), 147.50 (C), 159.04 (C), 165.61 (CO).

8.2.19.3 2-methyl-N-(p-tolyl)quinoline-4-carboxamide 38c

Purified by crystallization from EtOH. Yield: 99.3%; ^{1}H NMR (300 MHz, DMSO-d_6) δ: 2.29 (s, 3H, CH_3), 2.72 (s, 3H, CH_3), 7.21–8.08 (m, 9H, C_9H_5N and C_6H_4), 10.70 (s, 1H, NH); ^{13}C NMR (75 MHz, DMSO-d_6) δ: 20.96 (CH_3), 25.18 (CH_3), 120.33 (CH); 120.49 (2 × CH); 122.88 (C); 125.41 (CH); 127.09 (CH); 129.02 (CH); 129.69 (2 × CH); 130.37 (CH); 136.58 (C); 138.81 (C); 142.65 (C); 147.97 (C); 159.18 (C); 165.69 (CO).

8.2.19.4 N-(2,6-dimethylphenyl)-2-methylquinoline-4-carboxamide 38d

Purified by crystallization from EtOH. Yield: 64.5%; ^{1}H NMR (300 MHz, DMSO-d_6) δ: 2.34 (s, 6H, 2 × CH_3), 2.79 (s, 3H, CH_3), 7.17–8.21 (m, 8H, C_9H_5N and C_6H_3), 10.20 (s, 1H, NH). ^{13}C NMR (75 MHz, DMSO-d_6) δ: 18.73 (2 × CH_3), 24.88 (CH_3), 120.50 (2 × CH), 123.21 (C), 125.56 (CH), 127.39 (CH), 127.49 (CH), 128.38 (CH), 130.77 (CH), 134.81 (C), 135.85 (2 × C), 143.55 (C), 147.15 (C), 159.05 (C), 165.66 (CO).

8.2.19.5 2-methyl-N-(3,4,5-trimethoxyphenyl)quinoline-4-carboxamide 38e

Purified by crystallization from EtOH. Yield: 58.5%; ^{1}H NMR (300 MHz, DMSO-d_6) δ: 2.74 (s, 3H, CH_3), 3.67 (s, 3H, OCH_3), 3.79 (s, 6H, 2 × OCH_3), 7.22–8.12 (m, 7H, C_9H_5N and C_6H_2), 10.70 (s, 1H, NH); ^{13}C NMR (75 MHz, DMSO-d_6) δ: 25.28 (CH_3), 56.22 (2 × OCH_3), 60.62 (OCH_3), 98.11 (2 × CH), 120.32 (CH), 122.83 (C), 125.48 (CH), 127.05 (CH),

129.17 (CH), 130.29 (CH), 135.40 (C), 142.47 (C), 148.10 (C), 153.24 (3 × C), 159.04 (C), 165.64 (CO).

8.2.19.6 N-(3-chlorophenyl)-2-methylquinoline-4-carboxamide 38f

Purified by crystallization from EtOH. Yield: 69.4%; ^{1}H NMR (300 MHz, DMSO-d_6) δ: 2.78 (s, 3H, CH_3), 7.23–8.14 (m, 9H, C_9H_5N and C_6H_4), 11.00 (s, 1H, NH); ^{13}C NMR (75 MHz, DMSO-d_6) δ: 24.71 (CH_3), 118.87 (CH), 119.95 (CH), 120.71 (CH), 122.86 (C), 124.43 (CH), 125.58 (CH), 127.59 (CH), 128.11 (CH), 131.01 (CH), 131.05 (CH), 133.62 (C), 140.54 (C), 143.11 (C), 146.80 (C), 159.05 (C), 165.76 (CO).

8.2.19.7 N-(4-chlorophenyl)-2-methylquinoline-4-carboxamide 38g

Purified by crystallization from EtOH. Yield: 69.4%; ^{1}H NMR (300 MHz, DMSO-d_6) δ: 2.74 (s, 3H, CH_3), 7.46–8.10 (m, 9H, C_9H_5N and C_6H_4), 10.92 (s, 1H, NH); ^{13}C NMR (75 MHz, DMSO-d_6) δ: 25.28 (CH_3), 120.41 (CH), 121.92 (2×CH), 122.76 (C), 125.40 (CH), 127.12 (CH), 128.21 (C), 129.24 (3×CH), 130.34 (CH), 138.20 (C), 142.27 (C), 148.10 (C), 159.07 (C), 165.91 (CO).

8.2.19.8 2-methyl-N-(4-(trifluoromethyl)phenyl)quinoline-4-carboxamide 38h

Purified by crystallization from EtOH. Yield: 40.1%; ^{1}H NMR (300 MHz, DMSO-d_6) δ: 2.74 (s, 3H, CH_3), 7.62–8.10 (m, 9H, C_9H_5N and C_6H_4), 11.11 (s, 1H, NH); ^{13}C NMR (75 MHz, DMSO-d_6) δ: 25.27 (CH_3), 120.36 (2×CH), 120.46 (CH), 122.69 (C), 124.40 (C), 124.82 (C), 125.33 (CH), 126.60 (CH), 126.65 (CH), 127.18 (CH), 129.24 (CH), 130.36 (CH), 142.03 (C), 142.78 (C), 148.12 (C), 159.06 (C), 166.34 (CO).

8.2.19.9 2-methyl-N-(4-nitrophenyl)quinoline-4-carboxamide 38i

Purified by crystallization from EtOH. Yield: 54.8%; ^{1}H NMR (300 MHz, DMSO-d_6) δ: 2.74 (s, 3H, CH_3), 7.63–8.33 (m, 9H, C_9H_5N and C_6H_4), 11.34 (s, 1H, NH); ^{13}C NMR (75 MHz, DMSO-d_6) δ: 25.28 (CH_3), 120.23 (2×CH), 120.57 (CH), 122.59 (C), 125.27 (CH), 125.44 (2×CH), 127.27 (CH), 129.26 (CH), 130.43 (CH), 141.71 (C), 143.39 (C), 145.29 (C), 148.11 (C), 159.07 (C), 166.56 (CO).

8.2.19.10 2-methyl-N-(4-nitro-3-(trifluoromethyl)phenyl)quinoline-4-carboxamide 38j

Purified by crystallization from EtOH. Yield: 45.2%; ^{1}H NMR (300 MHz, DMSO-d_6) δ: 2.75 (s, 3H, CH_3), 7.60–8.48 (, 8H, C_9H_5N and C_6H_3), 11.53 (s, 1H, NH); ^{13}C NMR (75 MHz,

DMSO-d_6) δ: 25.29 (CH_3), 118.79 (CH), 120.69 (CH), 122.50 (C), 123.15 (C), 123.58 (C), 123.75 (CH), 125.34 (CH), 127.31 (CH), 128.11 (CH), 129.28 (CH), 130.47 (CH), 141.19 (C), 142.53 (C), 143.79 (C), 148.17 (C), 159.02 (C), 166.75 (CO).

8.2.20 General procedure for the synthesis of N-phenyl-2-(E)-2-phenylethenyl]quinoline-4- carboxamides 35a-z, 35aa-ah

In a 10 mL microwave reaction tube equipped with a magnetic stir bar, the appropriate substituted 2-methyl-N-phenylquinoline-4-carboxamide (**38a–j**) (1.0 eq) was dissolved in glacial AcOH. An appropriately substituted benzaldehyde (1.0 eq) or 3,4,5-trimethoxybenzaldehyde (2.0 eq) was then added to the solution. The tube was sealed, and the microwave reactor was set with the following parameters: T = 150 °C, Power = 200 W, Time = 40 minutes (2 cycles of 20 minutes each) and vigorous magnetic stirring (600 rpm). Upon completion, the reaction mixture was allowed to cool at room temperature, and water was added. The resulting precipitate was collected by vacuum filtration, washed with cold water and dried in a desiccator over silica gel. The crude substituted N-phenyl-2-(E)-2-phenylethenyl]quinoline-4-carboxamides ***35a-z, 35aa-ah*** were purified by crystallization from EtOH or by MPLC.

8.2.20.1 (E)-N-(4-nitro-3-(trifluoromethyl)phenyl)-2-styrylquinoline-4-carboxamide 35a

Purified by flash column chromatography EtOAc/Cyclohexane (1:1). Yield: 56.8%; ^{1}H NMR (300 MHz, DMSO-d_6) δ: 7.39–8.52 (m, 15H, C_9H_5N, 2×CH, C_6H_5, C_6H_3), 11.63 (s, 1H, NH); ^{13}C NMR (75 MHz, DMSO-d_6) δ: 118.39 (CH), 118.68 (CH), 118.76 (CH), 123.23 (C), 123.64 (C), 123.83 (CH), 124.34 (C), 125.45 (CH), 127.85 (3×CH), 128.21 (CH), 128.62 (CH), 129.44 (2×CH), 129.75 (CH), 130.94 (CH), 135.77 (CH), 136.50 (C), 141.68 (C), 142.60 (C), 143.81 (C), 148.52 (C), 155.95 (C), 166.77 (CO).

8.2.20.2 (E)-N-phenyl-2-styrylquinoline-4-carboxamide 35b

Purified by flash column chromatography EtOAc/Cyclohexane (1:1). Yield: 64.4%; ^{1}H NMR (300 MHz, DMSO-d_6) δ: 7.17–8.14 (m, 17H, C_9H_5N, 2×CH, 2×C_6H_5), 10.86 (s, 1H, NH); ^{13}C NMR (75 MHz, DMSO-d_6) δ: 118.04 (CH), 120.44 (2×CH), 123.66 (C), 124.63 (CH), 125.55 (CH), 127.57 (CH), 127.82 (2×CH), 128.75 (CH), 129.33 (2×CH), 129.40 (3×CH), 129.67 (CH), 130.69 (CH), 135.50 (CH), 136.61 (C), 139.31 (C), 143.09 (C), 148.50 (C), 155.97 (C), 165.86 (CO).

8.2.20.3 (E)-2-styryl-N-(p-tolyl)quinoline-4-carboxamide 35c

Purified by crystallization from EtOH. Yield: 91.1%; ^{1}H NMR (300 MHz, DMSO-d_6) δ: 2.33 (s, 3H, CH_3), 7.23–8.13 (m, 16H, C_9H_5N, 2×CH, C_6H_5, C_6H_4), 10.79 (s, 1H, NH); ^{13}C NMR (75 MHz, DMSO-d_6) δ: 21.02 (CH_3), 118.00 (CH), 120.38 (2×CH), 123.67 (C), 125.57 (CH), 127.54 (CH), 127.82 (2×CH), 128.74 (CH), 129.40 (3×CH), 129.69 (3×CH), 130.68 (CH), 133.61 (C), 135.46 (CH), 136.59 (C), 136.82 (C), 143.16 (C), 148.47 (C), 155.96 (C), 165.61 (CO).

8.2.20.4 (E)-N-(4-chlorophenyl)-2-styrylquinoline-4-carboxamide 35d

Purified by flash column chromatography EtOAc/Cyclohexane (1:1). Yield: 68.8%; ^{1}H NMR (300 MHz, DMSO-d_6) δ: 7.35–8.14 (m, 16H, C_9H_5N, 2×CH, C_6H_5, C_6H_4), 10.97 (s, 1H, NH); ^{13}C NMR (75 MHz, DMSO-d_6) δ: 118.07 (CH), 121.98 (2×CH), 123.53 (C), 125.48 (CH), 127.62 (CH), 127.81 (2×CH), 128.27 (C), 128.70 (CH), 129.26 (2×CH), 129.40 (3×CH), 129.67 (CH), 130.74 (CH), 135.56 (CH), 136.57 (C), 138.22 (C), 142.74 (C), 148.47 (C), 155.96 (C), 165.91 (CO).

8.2.20.5 (E)-2-styryl-N-(3,4,5-trimethoxyphenyl)quinoline-4-carboxamide 35e

Purified by flash column chromatography EtOAc/Cyclohexane (1:1). Yield: 56.2%; ^{1}H NMR (300 MHz, DMSO-d_6) δ: 3.69 (s, 3H, OCH_3), 3.80 (s, 6H, 2×OCH_3), 7.25–8.14 (m, 14H, C_9H_5N, 2×CH, C_6H_5, C_6H_2), 10.75 (s, 1H, NH); ^{13}C NMR (75 MHz, DMSO-d_6) δ: 56.31 (2×OCH_3), 60.65 (OCH_3), 98.32 (2×CH), 118.04 (CH), 123.61 (C), 125.57 (CH), 127.56 (CH), 127.82 (2×CH), 128.72 (CH), 129.40 (3×CH), 129.66 (CH), 130.69 (CH), 134.70 (C), 135.42 (C), 135.49 (CH), 136.58 (C), 142.98 (C), 148.48 (C), 153.29 (2×C), 155.92 (C), 165.65 (CO).

8.2.20.6 (E)-2-styryl-N-(4-(trifluoromethyl)phenyl)quinoline-4-carboxamide 35f

Purified by crystallization from EtOH. Yield: 67.6%; ^{1}H NMR (300 MHz, DMSO-d_6) δ: 7.38–8.18 (m, 16H, C_9H_5N, 2×CH, C_6H_5, C_6H_4), 11.25 (s, 1H, NH); ^{13}C NMR (75 MHz, DMSO-d_6) δ: 118.17 (CH), 120.41 (2×CH), 123.45 (C), 124.42 (C), 124.84 (C), 125.42 (CH), 126.63 (CH), 126.67 (CH), 127.70 (CH), 127.81 (2×CH), 128.67 (CH), 129.40 (3×CH), 129.69 (CH), 130.78 (CH), 135.61 (CH), 136.56 (C), 142.50 (C), 142.85 (C), 148.47 (C), 155.97 (C), 166.35 (CO).

8.2.20.7 (E)-N-(4-nitrophenyl)-2-styrylquinoline-4-carboxamide 35g

Purified by crystallization from EtOH. Yield: 63.2%; ^{1}H NMR (300 MHz, DMSO-d_6) δ: 7.39–8.37 (m, 16H, C_9H_5N, 2×CH, C_6H_5, C_6H_4), 11.44 (s, 1H, NH); ^{13}C NMR (75 MHz, DMSO-d_6) δ: 118.24 (CH), 120.27 (2×CH), 123.33 (C), 125.37 (CH), 125.47 (2×CH), 127.82 (3×CH), 128.64 (CH), 129.41 (3×CH), 129.73 (CH), 130.85 (CH), 135.70 (CH), 136.53 (C), 142.16 (C), 143.42 (C), 145.53 (C), 148.48 (C), 155.97 (C), 166.56 (CO).

8.2.20.8 (E)-2-styryl-N-(m-tolyl)quinoline-4-carboxamide 35h

Purified by crystallization from EtOH. Yield: 68.2%; ^{1}H NMR (300 MHz, DMSO-d_6) δ: 2.35 (s, 3H, CH_3), 6.99–8.11 (m, 16H, C_9H_5N, 2×CH, C_6H_5, C_6H_4), 10.75 (s, 1H, NH); ^{13}C NMR (75 MHz, DMSO-d_6) δ: 21.69 (CH_3), 117.64 (CH), 117.99 (CH), 120.93 (CH), 123.65 (C), 125.31 (CH), 125.52 (CH), 127.54 (CH), 127.81 (2×CH), 128.73 (CH), 129.14 (CH), 129.39 (3×CH), 129.64 (CH), 130.86 (CH), 135.47 (CH), 136.58 (C), 138.54 (C), 139.20 (C), 143.13 (C), 148.45 (C), 155.94 (C), 165.77 (CO).

8.2.20.9 (E)-N-(2,6-dimethylphenyl)-2-styrylquinoline-4-carboxamide 35i

Purified by flash column chromatography EtOAc/Cyclohexane (1:1). Yield: 83.2%; ^{1}H NMR (300 MHz, DMSO-d_6) δ: 2.39 (s, 6H, 2×CH_3), 7.19–8.24 (m, 15H, C_9H_5N, 2×CH, C_6H_5, C_6H_3), 10.27 (s, 1H, NH); ^{13}C NMR (75 MHz, DMSO-d_6) δ: 18.84 (2×CH_3), 118.55 (CH), 123.96 (C), 125.61 (CH), 127.48 (CH), 127.70 (CH), 127.94 (2×CH), 128.19 (CH), 128.40 (2×CH), 129.31 (CH), 129.41 (2×CH), 129.50 (CH), 130.94 (CH), 134.88 (C), 135.73 (CH), 135.87 (2×C), 136.51 (C), 143.60 (C), 148.02 (C), 155.59 (C), 165.75 (CO).

8.2.20.10 (E)-N-(3-chlorophenyl)-2-styrylquinoline-4-carboxamide 35j

Purified by flash column chromatography EtOAc/Cyclohexane (1:1). Yield: 84.8%; ^{1}H NMR (300 MHz, DMSO-d_6) δ: 7.24–8.15 (m, 16H, C_9H_5N, 2×CH, C_6H_5, C_6H_4), 11.02 (s, 1H, NH); ^{13}C NMR (75 MHz, DMSO-d_6) δ: 118.10 (CH), 118.84 (CH), 119.93 (CH), 123.48 (C), 124.37 (CH), 125.48 (CH), 127.67 (CH), 127.81 (2×CH), 128.68 (CH), 129.40 (3×CH), 129.68 (CH), 130.77 (CH), 131.06 (CH), 133.65 (C), 135.59 (CH), 136.55 (C), 140.67 (C), 142.58 (C), 148.47 (C), 155.95 (C), 166.10 (CO).

8.2.20.11 (E)-N-(4-nitro-3-(trifluoromethyl)phenyl)-2-(3,4,5-trimethoxystyryl)quinoline-4-carboxamide 35k

Purified by flash column chromatography EtOAc/Cyclohexane (1:1). Yield: 75.3%; ^{1}H NMR (300 MHz, DMSO-d_6) δ: 3.72 (s, 3H, OCH_3), 3.88 (s, 6H, 2×OCH_3), 7.11–8.50 (m, 12H, C_9H_5N, 2×CH, C_6H_2, C_6H_3), 11.60 (s, 1H, NH); ^{13}C NMR (75 MHz, DMSO-d_6) δ: 56.44 (2×OCH_3), 60.57 (OCH_3), 105.33 (2×CH), 118.28 (CH), 118.64 (CH), 118.71 (CH), 123.13 (C), 124.32 (C), 124.58 (C), 125.44 (CH), 127.75 (CH), 127.97 (CH), 128.19 (CH), 129.61 (CH), 130.92 (CH), 132.13 (C), 135.96 (CH), 138.93 (C), 141.53 (C), 142.58 (C), 143.79 (C), 148.56 (C), 153.64 (2×C), 156.09 (C), 166.77 (CO).

8.2.20.12 (E)-N-phenyl-2-(3,4,5-trimethoxystyryl)quinoline-4-carboxamide 35l

Purified by crystallization from EtOH. Yield: 44.7%; ^{1}H NMR (300 MHz, DMSO-d_6) δ: 3.71 (s, 3H, OCH_3), 3.87 (s, 6H, 2×OCH_3), 7.12–8.12 (m, 14H, C_9H_5N, 2×CH, C_6H_5, C_6H_2), 10.84 (s, 1H, NH); ^{13}C NMR (75 MHz, DMSO-d_6) δ: 56.43 (2×OCH_3), 60.57 (OCH_3), 105.31 (2×CH), 117.91 (CH), 120.41 (2×CH), 123.55 (C), 124.62 (CH), 125.55 (CH), 127.46 (CH), 128.10 (CH), 129.32 (2×CH), 129.53 (CH), 130.69 (CH), 132.23 (C), 135.72 (CH), 138.84 (C), 139.28 (C), 142.93 (C), 148.53 (C), 153.63 (2×C), 156.12 (C), 165.85 (CO).

8.2.20.13 (E)-N-(p-tolyl)-2-(3,4,5-trimethoxystyryl)quinoline-4-carboxamide 35m

Purified by crystallization from EtOH Yield: 72.9%; ^{1}H NMR (300 MHz, DMSO-d_6) δ: 2.32 (s, 3H, CH_3), 3.71 (s, 3H, OCH_3), 3.87 (s, 6H, 2×OCH_3), 7.12–8.12 (m, 13H, C_9H_5N, 2×CH, C_6H_4, C_6H_2), 10.74 (s, 1H, NH); ^{13}C NMR (75 MHz, DMSO-d_6) δ: 21.00 (CH_3), 56.42 (2×OCH_3), 60.57 (OCH_3), 105.30 (2×CH), 117.88 (CH), 120.41 (2×CH), 123.59 (C), 125.57 (CH), 127.41 (CH), 128.11 (CH), 129.53 (CH), 129.67 (2×CH), 130.66 (CH), 132.25 (C), 133.62 (C), 135.68 (CH), 136.79 (C), 138.83 (C), 143.02 (C), 148.53 (C), 153.62 (2×C), 156.11 (C), 165.63 (CO).

8.2.20.14 (E)-N-(4-chlorophenyl)-2-(3,4,5-trimethoxystyryl)quinoline-4-carboxamide 35n

Purified by flash column chromatography EtOAc/Cyclohexane (1:1). Yield: 43.7%; ^{1}H NMR (300 MHz, DMSO-d_6) δ: 3.72 (s, 3H, OCH_3), 3.88 (s, 6H, 2×OCH_3), 7.12–8.12 (m, 13H, C_9H_5N, 2×CH, C_6H_2, C_6H_4), 10.97 (s, 1H, NH); ^{13}C NMR (75 MHz, DMSO-d_6) δ: 56.43 (2×OCH_3), 60.57 (OCH_3), 105.33 (2×CH), 117.98 (CH), 121.99 (2×CH), 123.45 (C), 125.50

(CH), 127.51 (CH), 128.07 (CH), 128.27 (C), 129.25 (2×CH), 129.56 (CH), 130.73 (CH), 132.22 (C), 135.79 (CH), 138.22 (C), 138.88 (C), 142.61 (C), 148.54 (C), 153.64 (2×C), 156.12 (C), 165.94 (CO).

8.2.20.15 (E)-N-(3,4,5-trimethoxyphenyl)-2-(3,4,5-trimethoxystyryl)quinoline-4-carboxamide 35o

Purified by crystallization from EtOH. Yield: 66.8%; ^{1}H NMR (300 MHz, DMSO-d_6) δ: 3.68 (s, 3H, OCH_3), 3.71 (s, 3H, OCH_3), 3.80 (s, 6H, 2×OCH_3), 3.88 (s, 6H, 2×OCH_3), 7.12–8.14 (m, 11H, C_9H_5N, 2×CH, C_6H_2, C_6H_2), 10.74 (s, 1H, NH); ^{13}C NMR (75 MHz, DMSO-d_6) δ: 56.29 (2×OCH_3), 56.44 (2×OCH_3), 60.57 (OCH_3), 60.65 (OCH_3), 98.25 (2×CH), 105.32 (2×CH), 117.91 (CH), 123.52 (C), 125.58 (CH), 127.45 (CH), 128.08 (CH), 129.53 (CH), 130.69 (CH), 132.22 (2×C), 135.42 (2×C), 135.70 (CH), 142.84 (C), 148.53 (C), 153.27 (2×C), 153.63 (2×C), 156.07 (C), 165.65 (CO).

8.2.20.16 (E)-N-(4-(trifluoromethyl)phenyl)-2-(3,4,5-trimethoxystyryl)quinoline-4-carboxamide 35p

Purified by crystallization from EtOH. Yield: 71.6%; ^{1}H NMR (300 MHz, DMSO-d_6) δ: 3.72 (s, 3H, OCH_3), 3.88 (s, 6H, 2×OCH_3), 7.12–8.14 (m, 13H, C_9H_5N, 2×CH, C_6H_2, C_6H_4), 11.20 (s, 1H, NH); ^{13}C NMR (75 MHz, DMSO-d_6) δ: 56.43 (2×OCH_3), 60.57 (OCH_3), 105.31 (2×CH), 118.05 (CH), 120.39 (2×CH), 123.37 (C), 124.44 (C), 124.86 (C), 125.44 (CH), 126.63 (CH), 126.68 (CH), 127.59 (CH), 128.04 (CH), 129.58 (CH), 130.79 (CH), 132.20 (C), 135.85 (CH), 138.87 (C), 142.37 (C), 142.82 (C), 148.54 (C), 153.64 (2×C), 156.13 (C), 166.36 (CO).

8.2.20.17 (E)-N-(4-nitrophenyl)-2-(3,4,5-trimethoxystyryl)quinoline-4-carboxamide 35q

Purified by crystallization from EtOH. Yield: 70.3%; ^{1}H NMR (300 MHz, DMSO-d_6) δ: 3.71 (s, 3H, OCH_3), 3.87 (s, 6H, 2×OCH_3), 7.11–8.36 (m, 13H, C_9H_5N, 2×CH, C_6H_2, C_6H_4), 11.42 (s, 1H, NH); ^{13}C NMR (75 MHz, DMSO-d_6) δ: 56.44 (2×OCH_3), 60.57 (OCH_3), 105.34 (2×CH), 118.14 (CH), 120.27 (2×CH), 123.25 (C), 125.39 (CH), 125.48 (2×CH), 127.68 (CH), 128.01 (CH), 129.61 (CH), 130.85 (CH), 132.17 (C), 135.93 (CH), 138.90 (C), 142.02 (C), 143.42 (C), 145.32 (C), 148.53 (C), 153.64 (2×C), 156.13 (C), 166.56 (CO).

8.2.20.18 (E)-N-(m-tolyl)-2-(3,4,5-trimethoxystyryl)quinoline-4-carboxamide 35r

Purified by flash column chromatography EtOAc/Cyclohexane (1:1). Yield: 97.2%; ^{1}H NMR (300 MHz, DMSO-d_6) δ: 2.35 (s, 3H, CH_3), 3.72 (s, 3H, OCH_3), 3.88 (s, 6H, 2×OCH_3), 6.99–8.12 (m, 13H, C_9H_5N, 2×CH, C_6H_4, C_6H_2), 10.75 (s, 1H, NH); ^{13}C NMR (75 MHz, DMSO-d_6) δ: 21.69 (CH_3), 56.43 (2×OCH_3), 60.57 (OCH_3), 105.32 (2×CH), 117.64 (CH), 117.88 (CH), 120.94 (CH), 123.58 (C), 125.31 (CH), 125.55 (CH), 127.43 (CH), 128.10 (CH), 129.14 (CH), 129.53 (CH), 130.67 (CH), 132.24 (C), 135.69 (CH), 138.54 (C), 138.85 (C), 139.20 (C), 142.99 (C), 148.53 (C), 153.63 (2×C), 156.10 (C), 165.80 (CO).

8.2.20.19 (E)-N-(2,6-dimethylphenyl)-2-(3,4,5-trimethoxystyryl)quinoline-4-carboxamide 35s

Purified by flash column chromatography EtOAc/Cyclohexane (1:1)Yield: 70.8%; ^{1}H NMR (300 MHz, DMSO-d_6) δ: 2.38 (s, 6H, 2×CH_3), 3.72 (s, 3H, OCH_3), 3.89 (s, 6H, 2×OCH_3), 7.14–8.21 (m, 12H, C_9H_5N, 2×CH, C_6H_3, C_6H_2), 10.22 (s, 1H, NH); ^{13}C NMR (75 MHz, DMSO-d_6) δ: 18.85 (2×CH_3), 56.49 (2×OCH_3), 60.58 (OCH_3), 105.40 (2×CH), 118.38 (CH), 123.85 (C), 125.55 (CH), 127.45 (2×CH), 127.96 (CH), 128.40 (2×CH), 129.60 (CH), 130.73 (CH), 132.23 (C), 134.91 (C), 135.40 (CH), 135.83 (2×C), 138.86 (C), 143.27 (C), 148.55 (C), 153.64 (2×C), 155.82 (C), 165.58 (CO).

8.2.20.20 (E)-N-(3-chlorophenyl)-2-(3,4,5-trimethoxystyryl)quinoline-4-carboxamide 35t

Purified by flash column chromatography EtOAc/Cyclohexane (1:1). Yield: 68.7%; ^{1}H NMR (300 MHz, DMSO-d_6) δ: 3.72 (s, 3H, OCH_3), 3.88 (s, 6H, 2×OCH_3), 7.12–8.12 (m, 13H, C_9H_5N, 2×CH, C_6H_2, C_6H_4), 11.03 (s, 1H, NH); ^{13}C NMR (75 MHz, DMSO-d_6) δ: 56.42 (2×OCH_3), 60.57 (OCH_3), 105.31 (CH), 107.24 (CH), 118.01 (CH), 118.84 (CH), 119.93 (CH), 123.41 (C), 124.37 (CH), 125.51 (CH), 127.56 (CH), 128.06 (CH), 129.56 (CH), 130.77 (CH), 131.05 (CH), 132.21 (C), 133.66 (C), 135.82 (CH), 138.88 (C), 140.86 (C), 142.45 (C), 148.55 (C), 153.64 (2×C), 156.12 (C), 166.12 (CO).

8.2.20.21 (E)-2-(4-chlorostyryl)-N-(4-nitro-3-(trifluoromethyl)phenyl)quinoline-4-carboxamide 35u

Purified by flash column chromatography EtOAc/Cyclohexane (1:1). Yield: 66.8%; ^{1}H NMR (300 MHz, DMSO-d_6) δ: 7.39–8.52 (m, 14H, C_9H_5N, 2×CH, C_6H_4, C_6H_3), 11.63 (s, 1H, NH); ^{13}C NMR (75 MHz, DMSO-d_6) δ: 118.39 (CH), 118.68 (CH), 118.76 (CH), 123.23 (C), 123.64 (C), 123.83 (CH), 124.34 (C), 125.45 (CH), 127.85 (3×CH), 128.21 (CH),

128.62 (CH), 129.44 (2×CH), 129.75 (CH), 130.94 (CH), 135.77 (C), 136.50 (C), 141.68 (C), 142.60 (C), 143.81 (C), 148.52 (C), 155.95 (C), 166.77 (CO).

8.2.20.22 (E)-2-(3,4-dichlorostyryl)-N-(4-nitro-3-(trifluoromethyl)phenyl)quinoline-4-carboxamide 35v

Purified by flash column chromatography EtOAc/Cyclohexane (1:1). Yield: 57.3%; ^{1}H NMR (300 MHz, DMSO-d_6) δ: 7.41–8.48 (m, 13H, C_9H_5N, 2×CH, C_6H_3, C_6H_3), 11.82 (s, 1H, NH); ^{13}C NMR (75 MHz, DMSO-d_6) δ: 118.25 (CH), 118.55 (CH), 118.98 (CH), 123.24 (C), 123.51 (C), 123.79 (CH), 124.45 (C), 125.98 (CH), 127.73 (3×CH), 128.25 (CH), 128.69 (CH), 129.37 (2×CH), 129.74 (CH), 130.88 (C), 135.71 (C), 136.62 (C), 141.54 (C), 142.58 (C), 143.99 (C), 148.54 (C), 155.81 (C), 166.81 (CO).

8.2.20.23 (E)-2-(4-methoxystyryl)-N-(4-nitro-3-(trifluoromethyl)phenyl)quinoline-4-carboxamide 35w

Purified by flash column chromatography EtOAc/Cyclohexane (1:1). Yield: 75.3%; ^{1}H NMR (300 MHz, DMSO-d_6) δ: 3.41 (s, 3H, OCH_3), 7.42–8.66 (m, 14H, C_9H_5N, 2×CH, C_6H_4, C_6H_3), 11.77 (s, 1H, NH); ^{13}C NMR (75 MHz, DMSO-d_6) δ: 34.17 (OCH_3), 118.52 (CH), 118.73 (CH), 119.04 (CH), 123.54 (C), 123.79 (C), 123.97 (CH), 124.66 (C), 125.94 (CH), 127.83 (3×CH), 128.52 (CH), 128.91 (CH), 129.53 (2×CH), 129.98 (CH), 131.87 (CH), 135.62 (C), 136.78 (C), 141.63 (C), 142.52 (C), 143.66 (C), 148.58 (C), 155.71 (C), 166.32 (CO).

8.2.20.24 (E)-2-(3-methylstyryl)-N-(4-nitro-3-(trifluoromethyl)phenyl)quinoline-4-carboxamide 35x

Purified by flash column chromatography EtOAc/Cyclohexane (1:1). Yield: 73.5%; ^{1}H NMR (300 MHz, DMSO-d_6) δ: 2.37 (s, 3H, CH_3), 7.62–8.43 (m, 14H, C_9H_5N, 2×CH, C_6H_4, C_6H_3), 11.63 (s, 1H, NH); ^{13}C NMR (75 MHz, DMSO-d_6) δ: 23.05 (CH_3), 117.98 (CH), 118.30 (CH), 118.92 (CH), 123.05 (C), 123.51 (C), 123.88 (CH), 124.73 (C), 125.53 (CH), 127.44 (3×CH), 128.19 (CH), 128.81 (CH), 129.43 (2×CH), 129.89 (CH), 131.42 (CH), 135.42 (C), 136.93 (C), 141.18 (C), 142.42 (C), 143.66 (C), 148.41 (C), 155.40 (C), 166.88 (CO).

8.2.20.25 (E)-2-(4-chlorostyryl)-N-(4-(trifluoromethyl)phenyl)quinoline-4-carboxamide 35y

Purified by flash column chromatography EtOAc/Cyclohexane (1:1). Yield: 52.6%; ^{1}H NMR (300 MHz, DMSO-d$_6$) δ: 7.25–8.41 (m, 15H, C_9H_5N, 2×CH, C_6H_4, C_6H_4), 11.74 (s, 1H, NH); ^{13}C NMR (75 MHz, DMSO-d$_6$) δ: 118.12 (CH), 118.62 (CH), 118.95 (CH), 123.18 (C), 123.54 (C), 123.91 (CH), 124.53 (C), 125.51 (CH), 127.69 (3×CH), 128.18 (CH), 128.69 (CH), 129.34 (2×CH), 129.81 (CH), 130.93 (CH), 135.87 (C), 136.53 (C), 141.62 (C), 142.73 (C), 143.81 (C), 148.63 (C), 155.74 (C), 166.84 (CO).

8.2.20.26 (E)-2-(4-bromostyryl)-N-(4-(trifluoromethyl)phenyl)quinoline-4-carboxamide 35z

Purified by flash column chromatography EtOAc/Cyclohexane (1:1). Yield: 58.4%; ^{1}H NMR (300 MHz, DMSO-d$_6$) δ: 7.63–8.82 (m, 15H, C_9H_5N, 2×CH, C_6H_4, C_6H_4), 11.64 (s, 1H, NH); ^{13}C NMR (75 MHz, DMSO-d$_6$) δ: 118.07 (CH), 118.54 (CH), 118.93 (CH), 123.12 (C), 123.53 (C), 123.86 (CH), 124.51 (C), 125.52 (CH), 127.81 (3×CH), 128.31 (CH), 128.93 (CH), 129.43 (2×CH), 129.89 (CH), 130.91 (CH), 135.85 (C), 136.60 (C), 141.31 (C), 142.44 (C), 143.96 (C), 148.51 (C), 155.67 (C), 166.68 (CO).

8.2.20.27 (E)-2-(3,4-dichlorostyryl)-N-(4-(trifluoromethyl)phenyl)quinoline-4-carboxamide 35aa

Purified by flash column chromatography EtOAc/Cyclohexane (1:1). Yield: 61.2%; ^{1}H NMR (300 MHz, DMSO-d$_6$) δ: 7.42–8.78 (m, 14H, C_9H_5N, 2×CH, C_6H_3, C_6H_4), 11.81 (s, 1H, NH); ^{13}C NMR (75 MHz, DMSO-d$_6$) δ: 118.09 (CH), 118.41 (CH), 118.88 (CH), 123.12 (C), 123.44 (C), 123.91 (CH), 124.42 (C), 125.81 (CH), 127.47 (3×CH), 128.12 (CH), 128.75 (CH), 129.23 (2×CH), 129.66 (CH), 130.54 (C), 135.41 (C), 136.75 (C), 141.42 (C), 142.63 (C), 143.96 (C), 148.77 (C), 155.80 (C), 166.64 (CO).

8.2.20.28 (E)-2-(2-nitrostyryl)-N-(4-(trifluoromethyl)phenyl)quinoline-4-carboxamide 35ab

Purified by flash column chromatography EtOAc/Cyclohexane (1:1). Yield: 48.9; ^{1}H NMR (300 MHz, DMSO-d$_6$) δ: 7.78–8.85 (m, 15H, C_9H_5N, 2×CH, C_6H_4, C_6H_4), 11.85 (s, 1H, NH); ^{13}C NMR (75 MHz, DMSO-d$_6$) δ: 118.11 (CH), 118.53 (CH), 118.89 (CH), 123.18 (C), 123.46 (C), 123.87 (CH), 124.51 (C), 125.78 (CH), 127.71 (3×CH), 128.36 (CH), 128.84

(CH), 129.19 (2×CH), 129.80 (CH), 130.91 (CH), 135.60 (C), 136.74 (C), 141.38 (C), 142.44 (C), 143.82 (C), 148.34 (C), 155.74 (C), 166.41 (CO).

8.2.20.29 (E)-2-(3-nitrostyryl)-N-(4-(trifluoromethyl)phenyl)quinoline-4-carboxamide 35ac

Purified by flash column chromatography EtOAc/Cyclohexane (1:1). Yield: 43.9% ^{1}H NMR (300 MHz, DMSO-d_6) δ: 7.32–8.56 (m, 15H, C_9H_5N, 2×CH, C_6H_4, C_6H_4), 11.72 (s, 1H, NH); ^{13}C NMR (75 MHz, DMSO-d_6) δ: 118.20 (CH), 118.51 (CH), 118.83 (CH), 123.06 (C), 123.37 (C), 123.86 (CH), 124.31 (C), 125.75 (CH), 127.71 (3×CH), 128.26 (CH), 128.83 (CH), 129.22 (2×CH), 129.75 (CH), 130.87 (CH), 135.72 (C), 136.61 (C), 141.41 (C), 142.63 (C), 143.82 (C), 148.61 (C), 155.73 (C), 166.85 (CO).

8.2.20.30 (E)-2-(3-methylstyryl)-N-(4-(trifluoromethyl)phenyl)quinoline-4-carboxamide 35ad

Purified by crystallization from EtOH. Yield: 82.2%; ^{1}H NMR (300 MHz, DMSO-d_6) δ: 2.47 (s, 3H, CH_3), 7.34–8.55 (m, 15H, C_9H_5N, 2×CH, C_6H_4, C_6H_4), 11.78 (s, 1H, NH); ^{13}C NMR (75 MHz, DMSO-d_6) δ: 23.57 (CH_3), 117.42 (CH), 118.21 (CH), 118.73 (CH), 123.02 (C), 123.49 (C), 123.88 (CH), 124.85 (C), 125.69 (CH), 127.58 (3×CH), 128.12 (CH), 128.89 (CH), 129.47 (2×CH), 129.85 (CH), 131.55 (CH), 135.43 (CH), 136.86 (C), 141.27 (C), 142.57 (C), 143.73 (C), 148.69 (C), 155.52 (C), 166.88 (CO).

8.2.20.31 (E)-N-(4-chlorophenyl)-2-(4-chlorostyryl)quinoline-4-carboxamide 35ae

Purified by flash column chromatography EtOAc/Cyclohexane (1:1). Yield: 52.6%; ^{1}H NMR (300 MHz, DMSO-d_6) δ: 7.45–8.63 (m, 15H, C_9H_5N, 2×CH, C_6H_4, C_6H_4), 11.87 (s, 1H, NH); ^{13}C NMR (75 MHz, DMSO-d_6) δ: 118.23 (CH), 118.59 (CH), 118.82 (CH), 123.21 (C), 123.62 (C), 123.89 (CH), 124.66 (C), 125.47 (CH), 127.72 (3×CH), 128.14 (CH), 128.74 (CH), 129.41 (2×CH), 129.80 (CH), 130.92 (CH), 135.88 (C), 136.42 (C), 141.55 (C), 142.68 (C), 143.83 (C), 148.57 (C), 155.89 (C), 166.63 (CO).

8.2.20.32 (E)-N-(4-chlorophenyl)-2-(3,4-dichlorostyryl)quinoline-4-carboxamide 35af

Purified by flash column chromatography EtOAc/Cyclohexane (1:1). Yield: 53.9%; ^{1}H NMR (300 MHz, DMSO-d_6) δ: 7.81–8.67 (m, 14H, C_9H_5N, 2×CH, C_6H_3, C_6H_4), 11.74 (s, 1H, NH); ^{13}C NMR (75 MHz, DMSO-d_6) δ: 118.03 (CH), 118.37 (CH), 118.85 (CH), 123.05 (C), 123.38 (C), 123.82 (CH), 124.46 (C), 125.88 (CH), 127.43 (3×CH), 128.07 (CH),

128.68 (CH), 129.19 (2×CH), 129.57 (CH), 130.87 (C), 135.53 (C), 136.78 (C), 141.40 (C), 142.66 (C), 143.88 (C), 148.73 (C), 155.82 (C), 166.70 (CO).

8.2.20.33 (E)-N-(4-chlorophenyl)-2-(2-nitrostyryl)quinoline-4-carboxamide 35ag

Purified by flash column chromatography EtOAc/Cyclohexane (1:1). Yield: 42.1 %; ^{1}H NMR (300 MHz, DMSO-d_6) δ: 7.81–8.90 (m, 15H, C_9H_5N, 2×CH, C_6H_4, C_6H_4), 11.85 (s, 1H, NH); ^{13}C NMR (75 MHz, DMSO-d_6) δ: 118.03 (CH), 118.49 (CH), 118.98 (CH), 123.22 (C), 123.49 (C), 123.81 (CH), 124.49 (C), 125.87 (CH), 127.63 (3×CH), 128.31 (CH), 128.82 (CH), 129.23 (2×CH), 129.84 (CH), 130.98 (CH), 135.66 (C), 136.71 (C), 141.32 (C), 142.42 (C), 143.87 (C), 148.56 (C), 155.83 (C), 166.52 (CO).

8.2.20.34 (E)-N-(4-chlorophenyl)-2-(4-methoxystyryl)quinoline-4-carboxamide 35ah

Purified by crystallization from EtOH. Yield: 83.4 %; ^{1}H NMR (300 MHz, DMSO-d_6) δ: 3.72 (s, 3H, OCH_3), 7.43–8.69 (m, 15H, C_9H_5N, 2×CH, C_6H_4, C_6H_4), 11.92 (s, 1H, NH); ^{13}C NMR (75 MHz, DMSO-d_6) δ: 35.02 (OCH_3), 117.72 (CH), 118.62 (CH), 119.11 (CH), 123.34 (C), 123.76 (C), 124.05 (CH), 124.98 (C), 125.85 (CH), 127.69 (3×CH), 128.51 (CH), 128.99 (CH), 129.71 (2×CH), 130.12 (CH), 131.82 (CH), 135.57 (CH), 137.17 (C), 141.41 (C), 142.68 (C), 143.84 (C), 148.75 (C), 155.68 (C), 167.15 (CO).

8.3 BIOLOGY

8.3.1 SIRT6 production

Recombinant human SIRT6 protein was produced as described in a previously.[118] Human SIRT6(1-355) in vector pQE80L.1 was expressed in *E.coli* M15[pREP4] by autoinduction in TB medium at 16 °C overnight. The target protein was isolated via affinity chromatography on Talon resin (Clontech) and incubated with Tobacco Etch Virus (TEV) protease overnight at 4 °C to cleave off the affinity tag. TEV protease and affinity tag were removed via Talon affinity chromatography. The protein was further purified by cation exchange chromatography on SP sepharose and size-exclusion chromatography on a Superdex75 column. Purified protein was concentrated using an amicon centrifugal filter (Millipore, USA) to ~25 mg/mL, flash-frozen in liquid nitrogen, and stored at −80 °C.

8.3.2 SIRT6 deacetylation assay

For SIRT6 deacetylase assay, 3 μM SIRT6 was incubated with different test compounds in 50 μL of the assay buffer containing 20 mM HEPES pH 7.5, 100 mM NaCl, 2 mM DTT, 1% DMSO, 100 μM acetylated fluorogenic peptide substrate ("Fluor-de-Lys 1"; Enzo Life Sciences) and 500 μM NAD^+. Reactions were run at 37 °C for 1 h and then stopped and developed by adding 50 μL developer solution containing 2 mM NAM and 10 mg/mL trypsin. After incubation at room temperature for 20 min, fluorescence signals were measured at 360 nm (excitation)/460 nm (emission) using a FluoDia T70 (Photon Technology). Background controls contained all components except for SIRT6 protein. All assays were done in triplicates, and the reported data are representatives of at least two independent repetitions.

8.3.3 Cell lines

All the cell lines were of human origin and purchased from the American Type Culture Collection (ATCC, Manassas,VA, USA). Non-small cell lung carcinoma (A549), T-acute lymphoblastic leukemia (RPMI-8402), Medullobastoma (HD-MB03), Triple-negative breast cancer (MDA-MB-231) cells were grown in DMEM or RPMI medium (Gibco, Milano, Italy). Both media were supplemented with 115 units/mL of penicillin G (Gibco, Milano, Italy), 115 μg/mL of streptomycin (Invitrogen, Milano, Italy) and 10% fetal bovine serum (Invitrogen, Milano, Italy). Lymphoma cell lines (SU-DHL-8, VL51, TOLEDO, SU-DHL-18, SU-DHL-1, KM-H2) were cultured as recommended, using RPMI-1640 medium,

supplemented with 20% (v/v) fetal bovine serum, Penicillin-Streptomycin-Neomycin (~5000 units penicillin, 5 mg streptomycin and 10 mg neomycin/mL, Sigma) and L-glutamine (1%). Cell line identities were validated by CellCheck test (IDEXX, BioResearch) or with the Promega GenePrint 10 System kit, and all experiments were performed within one month after the cells were thawed. Cells were periodically tested to confirm mycoplasma negativity using the MycoAlert Mycoplasma Detection Kit (Lonza). Cells were incubated at 37 °C with 5% CO_2 and were subcultured every three days.

8.3.4 Preparation of compounds for in vitro screening

All compounds were dissolved in DMSO to obtain a stock concentration of 10 mM and were stored frozen at 4 °C. For each experiment, fresh dilutions of compounds were made from the stock solutions to obtain the indicated concentrations. The DMSO concentration did not exceed 0.1% in any experiment.

8.3.5 Cell proliferation analysis

For each screening experiment, cells were seeded in 96-well plates (non-tissue culture treated) at a density ranging from 5000 to 10,000 cells/well, depending on the doubling time of the specific cell line. For distributing cells into wells of the plates either a VIAFLO 96 hand-held electronic channel pipette (Integra Biosciences) or manual 12-channel pipet was used. Cells were initially treated with a single dose of 1 μM compound for 72 h. Selected compounds, which reached proliferation inhibition of about 60%, were further tested in the appropriate tissue culture medium with increasing compound doses ranging from 0 to 10 μM, using 1:2 dilution in series to obtain IC_{50} values. These assays were performed in triplicate. To 100 μL of cells suspended in medium, 100 μL of drug suspension was added, for a total seeding volume of 200 μL/well. After preparation of the microplates, they were incubated at 37 ◦C in a 5% CO_2, 95% air atmosphere with 100% relative humidity for 72 h. Wells containing medium only were included on each plate and used as blanks for absorbance readings. MTT (Sigma, Buchs) was prepared as a 5 mg/mL stock in phosphate-buffered saline and filter-sterilized. At the end of the incubation period, 20 μL of MTT solution was added to each well, and microplates were incubated at 37 °C for 4 h. Cells were then lysed with 50 μL per well of 25% sodium dodecyl sulfate lysis buffer, and absorbance was read at 570 nm using a Beckman Coulter-AD340 plate reader. The % of proliferation by the cells was obtained by quantifying the linear relationship between live cells and the A570 signal produced.

8.3.6 Antiproliferative activity in PBMCs

Additional experiments were carried out with PBMCs from healthy donors as described previously.[119] For cytotoxicity evaluations in proliferating PBMC cultures, non-adherent cells were resuspended at 5 ×105 cells/mL in a growth medium containing 2.5 g/mL PHA (Irvine Scientific). The same cellular density was used also for resting PBMC cultures but without the addition of PHA. Scalar concentrations of the tested compounds were added, and viability was determined after a 72 h incubation by the MTT test.

8.3.7 Apoptosis assay

The quantification of apoptosis induced by the tested compound was carried out by flow cytometric analysis using the Annexin-V Fluos kit (Roche Diagnostics) following the manufacturer's instructions. The cells treated with different concentrations of the test compound after a 48 h incubation were labeled with annexin V/FITC and PI and analyzed with a Coulter Cytomics FC500 instrument (Beckman Coulter) in the FL1 and FL3 channels, respectively.

8.3.8 Cell cycle assay

For these experiments, the VL51 and TOLEDO cell lines were used. They were seeded in 6-well plates at a density of 5 ×104, 2.5 ×105 and 2.0 ×105, respectively, in a final volume of 2 mL culture medium. The cells were then treated with the test compounds for 24 h at the indicated concentrations. After this incubation period, the cells were detached with trypsin-EDTA and harvested by centrifugation. The pellet thus obtained was fixed in 70% ice cold EtOH. Then the cells were processed and analyzed as described previously,[120] except that for the acquisition of data with labeled cells, a Cytomics FC500 flow cytometer (Beckman Coulter) was used.

9. REFERENCES

1. Null, M., Arbor, T. C. & Agarwal, M. *Anatomy, Lymphatic System*. (2025).
2. Leong, S. P. L. & Witte, M. H. Future Perspectives and Unanswered Questions on Cancer Metastasis and the Lymphovascular System. in 293–296 (2007). doi:10.1007/978-0-387-69219-7_21.
3. Petrova, T. V. & Koh, G. Y. Biological functions of lymphatic vessels. *Science (1979)* **369**, (2020).
4. Vojdani, A. *et al.* Natural Killer Cells and Cytotoxic T Cells: Complementary Partners against Microorganisms and Cancer. *Microorganisms* **12**, 230 (2024).
5. Montorsi, L., Siu, J. H. Y. & Spencer, J. B cells in human lymphoid structures. *Clin Exp Immunol* **210**, 240–252 (2022).
6. Granzow, J. W. Lymphedema surgery: the current state of the art. *Clin Exp Metastasis* **35**, 553–558 (2018).
7. Pecora, F. *et al.* Management of Infectious Lymphadenitis in Children. *Children* **8**, 860 (2021).
8. Lourens, G. B. & Ferrell, D. K. Lymphatic Filariasis. *Nursing Clinics of North America* **54**, 181–192 (2019).
9. Siegel, R. L., Giaquinto, A. N. & Jemal, A. Cancer statistics, 2024. *CA Cancer J Clin* **74**, 12–49 (2024).
10. Opinto, G. *et al.* Hodgkin Lymphoma: A Special Microenvironment. *J Clin Med* **10**, 4665 (2021).
11. Hoppe, R. T. *et al.* NCCN Guidelines Insights: Hodgkin Lymphoma, Version 1.2018. *Journal of the National Comprehensive Cancer Network* **16**, 245–254 (2018).
12. Engert, A. *et al.* Two Cycles of Doxorubicin, Bleomycin, Vinblastine, and Dacarbazine Plus Extended-Field Radiotherapy Is Superior to Radiotherapy Alone in Early Favorable Hodgkin's Lymphoma: Final Results of the GHSG HD7 Trial. *Journal of Clinical Oncology* **25**, 3495–3502 (2007).
13. Munir, F. *et al.* Classical Hodgkin Lymphoma: From Past to Future—A Comprehensive Review of Pathophysiology and Therapeutic Advances. *Int J Mol Sci* **24**, 10095 (2023).
14. Kahn, J. M. *et al.* Survival by age in paediatric and adolescent patients with Hodgkin lymphoma: a retrospective pooled analysis of children's oncology group trials. *Lancet Haematol* **9**, e49–e57 (2022).
15. Swerdlow, S. H. *et al.* The 2016 revision of the World Health Organization classification of lymphoid neoplasms. *Blood* **127**, 2375–2390 (2016).
16. Dogan, A. & Roshal, M. Challenges in defining the immune microenvironment in T-cell lymphoma. *Haematologica* (2024) doi:10.3324/haematol.2024.285836.
17. Cheson, B. D. & Leonard, J. P. Monoclonal Antibody Therapy for B-Cell Non-Hodgkin's Lymphoma. *New England Journal of Medicine* **359**, 613–626 (2008).
18. Dave, S. S. *et al.* Prediction of Survival in Follicular Lymphoma Based on Molecular Features of Tumor-Infiltrating Immune Cells. *New England Journal of Medicine* **351**, 2159–2169 (2004).

19. Scott, D. W. *et al.* High-grade B-cell lymphoma with MYC and BCL2 and/or BCL6 rearrangements with diffuse large B-cell lymphoma morphology. *Blood* **131**, 2060–2064 (2018).
20. Ferlay, J. *et al.* Estimating the global cancer incidence and mortality in 2018: GLOBOCAN sources and methods. *Int J Cancer* **144**, 1941–1953 (2019).
21. Chu, D.-T. *et al.* Recent Progress of Stem Cell Therapy in Cancer Treatment: Molecular Mechanisms and Potential Applications. *Cells* **9**, 563 (2020).
22. Neelapu, S. S. *et al.* Comparison of 2-year outcomes with CAR T cells (ZUMA-1) vs salvage chemotherapy in refractory large B-cell lymphoma. *Blood Adv* **5**, 4149–4155 (2021).
23. Falchi, L., Vardhana, S. A. & Salles, G. A. Bispecific antibodies for the treatment of B-cell lymphoma: promises, unknowns, and opportunities. *Blood* **141**, 467–480 (2023).
24. Patton, J. T. & Woyach, J. A. Targeting the B cell receptor signaling pathway in chronic lymphocytic leukemia. *Semin Hematol* **61**, 100–108 (2024).
25. Yang, H., Xun, Y., Ke, C., Tateishi, K. & You, H. Extranodal lymphoma: pathogenesis, diagnosis and treatment. *Molecular Biomedicine* **4**, 29 (2023).
26. Isaacson, P. G. & Du, M.-Q. MALT lymphoma: from morphology to molecules. *Nat Rev Cancer* **4**, 644–653 (2004).
27. Willemze, R. WHO-EORTC classification for cutaneous lymphomas. *Blood* **105**, 3768–3785 (2005).
28. Chiu, B. C.-H. & Hou, N. Epidemiology and Etiology of Non-Hodgkin Lymphoma. in 1–25 (2015). doi:10.1007/978-3-319-13150-4_1.
29. Kelly, R. S. & Vineis, P. Biomarkers of susceptibility to chemical carcinogens: the example of non-Hodgkin lymphomas. *Br Med Bull* **111**, 89–100 (2014).
30. Ysebaert, L. *et al.* Lymphoma Heterogeneity Unraveled by Single-Cell Transcriptomics. *Front Immunol* **12**, (2021).
31. Asmamaw Dejenie, T. *et al.* Current updates on generations, approvals, and clinical trials of CAR T-cell therapy. *Hum Vaccin Immunother* **18**, (2022).
32. Cirillo, M., Craig, A. F. M., Borchmann, S. & Kurtz, D. M. Liquid biopsy in lymphoma: Molecular methods and clinical applications. *Cancer Treat Rev* **91**, 102106 (2020).
33. Lunning, M. A. & Vose, J. M. Management of indolent lymphoma: where are we now and where are we going. *Blood Rev* **26**, 279–88 (2012).
34. Arcaini, L. *et al.* Antiviral treatment in patients with indolent B-cell lymphomas associated with HCV infection: a study of the Fondazione Italiana Linfomi. *Annals of Oncology* **25**, 1404–1410 (2014).
35. Rummel, M. J. *et al.* Bendamustine plus rituximab versus CHOP plus rituximab as first-line treatment for patients with indolent and mantle-cell lymphomas: an open-label, multicentre, randomised, phase 3 non-inferiority trial. *The Lancet* **381**, 1203–1210 (2013).
36. Hallek, M. *et al.* iwCLL guidelines for diagnosis, indications for treatment, response assessment, and supportive management of CLL. *Blood* **131**, 2745–2760 (2018).
37. Montoto, S. & Fitzgibbon, J. Transformation of Indolent B-Cell Lymphomas. *Journal of Clinical Oncology* **29**, 1827–1834 (2011).
38. Padala, S. A. & Kallam, A. *Diffuse Large B-Cell Lymphoma*. (2025).

39. Hutcheson, R. L., Chakravorty, A. & Sugden, B. Burkitt Lymphomas Evolve to Escape Dependencies on Epstein-Barr Virus. *Front Cell Infect Microbiol* **10**, 606412 (2020).
40. Kostakoglu, L. PET-CT Imaging of Lymphoma. in *Clinical PET-CT in Radiology* 265–291 (Springer New York, New York, NY, 2011). doi:10.1007/978-0-387-48902-5_22.
41. Abrisqueta, P. New Insights into First-Line Therapy in Diffuse Large B-Cell Lymphoma: Are We Improving Outcomes? *J Clin Med* **13**, (2024).
42. Manickam Gurusamy, V. *et al.* The role of radiotherapy in newly diagnosed primary CNS lymphoma: A descriptive review and a pragmatic approach to clinical practice. *Clin Transl Radiat Oncol* **39**, 100559 (2023).
43. Crump, M. *et al.* Outcomes in refractory diffuse large B-cell lymphoma: results from the international SCHOLAR-1 study. *Blood* **130**, 1800–1808 (2017).
44. Sethi, A., Tandon, A., Mishra, H. & Singh, I. Diffuse large B-cell lymphoma: An immunohistochemical approach to diagnosis. *Journal of Oral and Maxillofacial Pathology* **23**, 284 (2019).
45. Kuo, S.-H. *et al.* Helicobacter pylori-related diffuse large B-cell lymphoma of the stomach: a distinct entity with lower aggressiveness and higher chemosensitivity. *Blood Cancer J* **4**, e220 (2014).
46. Burns, D. M. & Chaganti, S. Epstein-Barr virus-associated lymphoproliferative disorders in immunosuppressed patients. *Ann Lymphoma* **5**, 24–24 (2021).
47. Mlynarczyk, C., Fontán, L. & Melnick, A. Germinal center-derived lymphomas: The darkest side of humoral immunity. *Immunol Rev* **288**, 214–239 (2019).
48. Vodicka, P., Klener, P. & Trneny, M. Diffuse Large B-Cell Lymphoma (DLBCL): Early Patient Management and Emerging Treatment Options. *Onco Targets Ther* **15**, 1481–1501 (2022).
49. Dunleavy, K. *et al.* Dose-adjusted EPOCH-R (etoposide, prednisone, vincristine, cyclophosphamide, doxorubicin, and rituximab) in untreated aggressive diffuse large B-cell lymphoma with MYC rearrangement: a prospective, multicentre, single-arm phase 2 study. *Lancet Haematol* **5**, e609–e617 (2018).
50. Fabbri, N., Mussetti, A. & Sureda, A. Second-line treatment of diffuse large B-cell lymphoma: Evolution of options. *Semin Hematol* **60**, 305–312 (2023).
51. Kapoor, I. *et al.* Resistance to BTK inhibition by ibrutinib can be overcome by preventing FOXO3a nuclear export and PI3K/AKT activation in B-cell lymphoid malignancies. *Cell Death Dis* **10**, 924 (2019).
52. Xu, J. *et al.* Current Advances and Future Strategies for BCL-2 Inhibitors: Potent Weapons against Cancers. *Cancers (Basel)* **15**, (2023).
53. Yang, J. *et al.* Sirt6 promotes tumorigenesis and drug resistance of diffuse large B-cell lymphoma by mediating PI3K/Akt signaling. *Journal of Experimental & Clinical Cancer Research* **39**, 142 (2020).
54. Yu, W., Yang, Z., Huang, R., Min, Z. & Ye, M. SIRT6 promotes the Warburg effect of papillary thyroid cancer cell BCPAP through reactive oxygen species . *Onco Targets Ther* **Volume 12**, 2861–2868 (2019).
55. Chen, L. *et al.* SYK Inhibition Modulates Distinct PI3K/AKT- Dependent Survival Pathways and Cholesterol Biosynthesis in Diffuse Large B Cell Lymphomas. *Cancer Cell* **23**, 826–838 (2013).

56. Schutkowski, M., Fischer, F., Roessler, C. & Steegborn, C. New assays and approaches for discovery and design of Sirtuin modulators. *Expert Opin Drug Discov* **9**, 183–199 (2014).
57. Minisini, M. *et al.* Transcriptomic and genomic studies classify NKL54 as a histone deacetylase inhibitor with indirect influence on MEF2-dependent transcription. *Nucleic Acids Res* **50**, 2566–2586 (2022).
58. Li, G., Tian, Y. & Zhu, W.-G. The Roles of Histone Deacetylases and Their Inhibitors in Cancer Therapy. *Front Cell Dev Biol* **8**, (2020).
59. Carafa, V. *et al.* Sirtuin functions and modulation: from chemistry to the clinic. *Clin Epigenetics* **8**, 61 (2016).
60. Taurone, S. *et al.* Biochemical Functions and Clinical Characterizations of the Sirtuins in Diabetes-Induced Retinal Pathologies. *Int J Mol Sci* **23**, 4048 (2022).
61. Schutkowski, M., Fischer, F., Roessler, C. & Steegborn, C. New assays and approaches for discovery and design of Sirtuin modulators. *Expert Opin Drug Discov* **9**, 183–199 (2014).
62. Avalos, J. L. *et al.* Structure of a Sir2 Enzyme Bound to an Acetylated p53 Peptide. *Mol Cell* **10**, 523–535 (2002).
63. Fiorentino, F., Mai, A. & Rotili, D. The role of structural biology in the design of sirtuin activators. *Curr Opin Struct Biol* **82**, 102666 (2023).
64. Sauve, A. A. *et al.* Chemistry of Gene Silencing: The Mechanism of NAD^+-Dependent Deacetylation Reactions. *Biochemistry* **40**, 15456–15463 (2001).
65. Rauh, D. *et al.* An acetylome peptide microarray reveals specificities and deacetylation substrates for all human sirtuin isoforms. *Nat Commun* **4**, 2327 (2013).
66. Pannek, M. *et al.* Crystal structures of the mitochondrial deacylase Sirtuin 4 reveal isoform-specific acyl recognition and regulation features. *Nat Commun* **8**, 1513 (2017).
67. Du, J. *et al.* Sirt5 Is a NAD-Dependent Protein Lysine Demalonylase and Desuccinylase. *Science (1979)* **334**, 806–809 (2011).
68. Tan, M. *et al.* Lysine Glutarylation Is a Protein Posttranslational Modification Regulated by SIRT5. *Cell Metab* **19**, 605–617 (2014).
69. Pan, P. W. *et al.* Structure and Biochemical Functions of SIRT6. *Journal of Biological Chemistry* **286**, 14575–14587 (2011).
70. Li, L. *et al.* SIRT7 is a histone desuccinylase that functionally links to chromatin compaction and genome stability. *Nat Commun* **7**, 12235 (2016).
71. Simonet, N. G. *et al.* SirT7 auto-ADP-ribosylation regulates glucose starvation response through mH2A1. *Sci Adv* **6**, (2020).
72. Fiorentino, F., Mai, A. & Rotili, D. Emerging Therapeutic Potential of SIRT6 Modulators. *J Med Chem* **64**, 9732–9758 (2021).
73. Mostoslavsky, R. *et al.* Genomic Instability and Aging-like Phenotype in the Absence of Mammalian SIRT6. *Cell* **124**, 315–329 (2006).
74. Toiber, D. *et al.* SIRT6 Recruits SNF2H to DNA Break Sites, Preventing Genomic Instability through Chromatin Remodeling. *Mol Cell* **51**, 454–468 (2013).
75. Yang, B., Zwaans, B. M. M., Eckersdorff, M. & Lombard, D. B. The sirtuin SIRT6 deacetylates H3 K56Ac in vivo to promote genomic stability. *Cell Cycle* **8**, 2662–2663 (2009).

76. Michishita, E. *et al.* SIRT6 is a histone H3 lysine 9 deacetylase that modulates telomeric chromatin. *Nature* **452**, 492–496 (2008).
77. Kim, H.-S. *et al.* Hepatic-Specific Disruption of SIRT6 in Mice Results in Fatty Liver Formation Due to Enhanced Glycolysis and Triglyceride Synthesis. *Cell Metab* **12**, 224–236 (2010).
78. Kawahara, T. L. A. *et al.* SIRT6 Links Histone H3 Lysine 9 Deacetylation to NF-κB-Dependent Gene Expression and Organismal Life Span. *Cell* **136**, 62–74 (2009).
79. Lombard, D. B., Schwer, B., Alt, F. W. & Mostoslavsky, R. SIRT6 in DNA repair, metabolism and ageing. *J Intern Med* **263**, 128–141 (2008).
80. Ouyang, L. *et al.* SIRT6 overexpression induces apoptosis of nasopharyngeal carcinoma by inhibiting NF-κB signaling. *Onco Targets Ther* **Volume 11**, 7613–7624 (2018).
81. Chen, X. *et al.* The histone deacetylase SIRT6 suppresses the expression of the RNA-binding protein PCBP2 in glioma. *Biochem Biophys Res Commun* **446**, 364–369 (2014).
82. Kugel, S. *et al.* SIRT6 Suppresses Pancreatic Cancer through Control of Lin28b. *Cell* **165**, 1401–1415 (2016).
83. Choe, M. *et al.* The RUNX2 Transcription Factor Negatively Regulates SIRT6 Expression to Alter Glucose Metabolism in Breast Cancer Cells. *J Cell Biochem* **116**, 2210–2226 (2015).
84. Yu, W., Yang, Z., Huang, R., Min, Z. & Ye, M. SIRT6 promotes the Warburg effect of papillary thyroid cancer cell BCPAP through reactive oxygen species . *Onco Targets Ther* **Volume 12**, 2861–2868 (2019).
85. Yang, Z., Yu, W., Huang, R., Ye, M. & Min, Z. SIRT6/HIF-1α axis promotes papillary thyroid cancer progression by inducing epithelial–mesenchymal transition. *Cancer Cell Int* **19**, 17 (2019).
86. Bai, L. *et al.* Upregulation of SIRT6 predicts poor prognosis and promotes metastasis of non-small cell lung cancer via the ERK1/2/MMP9 pathway. *Oncotarget* **7**, 40377–40386 (2016).
87. Krishnamoorthy, V. & Vilwanathan, R. Silencing Sirtuin 6 induces cell cycle arrest and apoptosis in non-small cell lung cancer cell lines. *Genomics* **112**, 3703–3712 (2020).
88. Zhou, H.-Z. *et al.* NQO1 potentiates apoptosis evasion and upregulates XIAP via inhibiting proteasome-mediated degradation SIRT6 in hepatocellular carcinoma. *Cell Communication and Signaling* **17**, 168 (2019).
89. Ran, L.-K. *et al.* SIRT6 Overexpression Potentiates Apoptosis Evasion in Hepatocellular Carcinoma via BCL2-Associated X Protein–Dependent Apoptotic Pathway. *Clinical Cancer Research* **22**, 3372–3382 (2016).
90. Liu, Y. *et al.* Inhibition of SIRT6 in prostate cancer reduces cell viability and increases sensitivity to chemotherapeutics. *Protein Cell* **4**, 702–710 (2013).
91. Geng, C. *et al.* Overexpression of Sirt6 is a novel biomarker of malignant human colon carcinoma. *J Cell Biochem* **119**, 3957–3967 (2018).
92. Fiorentino, F., Fabbrizi, E., Mai, A. & Rotili, D. Activation and inhibition of sirtuins: From bench to bedside. *Med Res Rev* **45**, 484–560 (2025).
93. Wood, M., Rymarchyk, S., Zheng, S. & Cen, Y. Trichostatin A inhibits deacetylation of histone H3 and p53 by SIRT6. *Arch Biochem Biophys* **638**, 8–17 (2018).

94. You, W. & Steegborn, C. Structural Basis of Sirtuin 6 Inhibition by the Hydroxamate Trichostatin A: Implications for Protein Deacylase Drug Development. *J Med Chem* **61**, 10922–10928 (2018).
95. Sociali, G. *et al.* Quinazolinedione SIRT6 inhibitors sensitize cancer cells to chemotherapeutics. *Eur J Med Chem* **102**, 530–539 (2015).
96. Sun, W. *et al.* Discovery of 5-(4-methylpiperazin-1-yl)-2-nitroaniline derivatives as a new class of SIRT6 inhibitors. *Bioorg Med Chem Lett* **30**, 127215 (2020).
97. Song, N. *et al.* Discovery of a pyrrole-pyridinimidazole derivative as novel SIRT6 inhibitor for sensitizing pancreatic cancer to gemcitabine. *Cell Death Dis* **14**, 499 (2023).
98. Song, N. *et al.* A SIRT6 Inhibitor, Marine-Derived Pyrrole-Pyridinimidazole Derivative 8a, Suppresses Angiogenesis. *Mar Drugs* **21**, 517 (2023).
99. Zhang, Q. *et al.* Targeting a cryptic allosteric site of SIRT6 with small-molecule inhibitors that inhibit the migration of pancreatic cancer cells. *Acta Pharm Sin B* **12**, 876–889 (2022).
100. Xu, X. *et al.* Discovery of a potent and highly selective inhibitor of SIRT6 against pancreatic cancer metastasis in vivo. *Acta Pharm Sin B* **14**, 1302–1316 (2024).
101. Liang, C. *et al.* Structure-Guided Discovery of Subtype Selective SIRT6 Inhibitors with a β-Carboline Skeleton for the Treatment of Breast Cancer. *J Med Chem* **67**, 21975–22001 (2024).
102. Parenti, M. D. *et al.* Discovery of Novel and Selective SIRT6 Inhibitors. *J Med Chem* **57**, 4796–4804 (2014).
103. Madhavi Sastry, G., Adzhigirey, M., Day, T., Annabhimoju, R. & Sherman, W. Protein and ligand preparation: parameters, protocols, and influence on virtual screening enrichments. *J Comput Aided Mol Des* **27**, 221–234 (2013).
104. Lu, C. *et al.* OPLS4: Improving Force Field Accuracy on Challenging Regimes of Chemical Space. *J Chem Theory Comput* **17**, 4291–4300 (2021).
105. Bandgar, B. P., Bettigeri, S. V. & Phopase, J. Unsymmetrical Diaryl Sulfones through Palladium-Catalyzed Coupling of Aryl Boronic Acids and Arylsulfonyl Chlorides. *Org Lett* **6**, 2105–2108 (2004).
106. Munawar, S. *et al.* Steglich esterification: A versatile synthetic approach toward the synthesis of natural products, their analogues/derivatives. *Heliyon* **10**, e23416 (2024).
107. Beutner, G. L. *et al.* TCFH–NMI: Direct Access to *N* -Acyl Imidazoliums for Challenging Amide Bond Formations. *Org Lett* **20**, 4218–4222 (2018).
108. Vélez, C. *et al.* Toxicity and Apoptosis Related Effects of Benzimidazo [3,2-α] Quinolinium Salts Upon Human Lymphoma Cells. *Open Med Chem J* **11**, 54–65 (2017).
109. Kalac, M. *et al.* N-quinoline-benzenesulfonamide derivatives exert potent anti-lymphoma effect by targeting NF-κB. *iScience* **23**, 101884 (2020).
110. Muscia, G. C., Asis, S. E. & Buldain, G. Y. Microwave-assisted Synthesis of 2-Styrylquinoline-4-carboxylic Acids as Antitubercular Agents. *Med Chem (Los Angeles)* **13**, (2017).
111. Devi, P. *et al.* Synthesis and structural characterisation of amides from picolinic acid and pyridine-2,6-dicarboxylic acid. *Sci Rep* **5**, 9950 (2015).

112. Chen, L. *et al.* SYK Inhibition Modulates Distinct PI3K/AKT- Dependent Survival Pathways and Cholesterol Biosynthesis in Diffuse Large B Cell Lymphomas. *Cancer Cell* **23**, 826–838 (2013).
113. Lu, C. *et al.* OPLS4: Improving Force Field Accuracy on Challenging Regimes of Chemical Space. *J Chem Theory Comput* **17**, 4291–4300 (2021).
114. Johnston, R. C. *et al.* Epik: p K_a and Protonation State Prediction through Machine Learning. *J Chem Theory Comput* **19**, 2380–2388 (2023).
115. Halgren, T. A. *et al.* Glide: A New Approach for Rapid, Accurate Docking and Scoring. 2. Enrichment Factors in Database Screening. *J Med Chem* **47**, 1750–1759 (2004).
116. Bowers, K. J. *et al.* Molecular dynamics---Scalable algorithms for molecular dynamics simulations on commodity clusters. in *Proceedings of the 2006 ACM/IEEE conference on Supercomputing - SC '06* 84 (ACM Press, New York, New York, USA, 2006). doi:10.1145/1188455.1188544.
117. Clark, A. J. *et al.* Prediction of Protein–Ligand Binding Poses via a Combination of Induced Fit Docking and Metadynamics Simulations. *J Chem Theory Comput* **12**, 2990–2998 (2016).
118. Schlicker, C., Boanca, G., Lakshminarasimhan, M. & Steegborn, C. Structure-based development of novel sirtuin inhibitors. *Aging* **3**, 852–872 (2011).
119. Romagnoli, R. *et al.* Design, Synthesis, in Vitro, and in Vivo Anticancer and Antiangiogenic Activity of Novel 3-Arylaminobenzofuran Derivatives Targeting the Colchicine Site on Tubulin. *J Med Chem* **58**, 3209–3222 (2015).
120. Viola, G. *et al.* Induction of γ-globin mRNA, erythroid differentiation and apoptosis in UVA-irradiated human erythroid cells in the presence of furocumarin derivatives. *Biochem Pharmacol* **75**, 810–825 (2008).